University College of Southeast Norway
Faculty of Technology, Natural Sciences and Maritime Sciences
—
Doctoral dissertation Nr 34
2018

Asmat Nawaz

Perovskite Solar Cells: Improved Active layer Morphology and Pore-filling in TiO2 Nano-Scaffolds

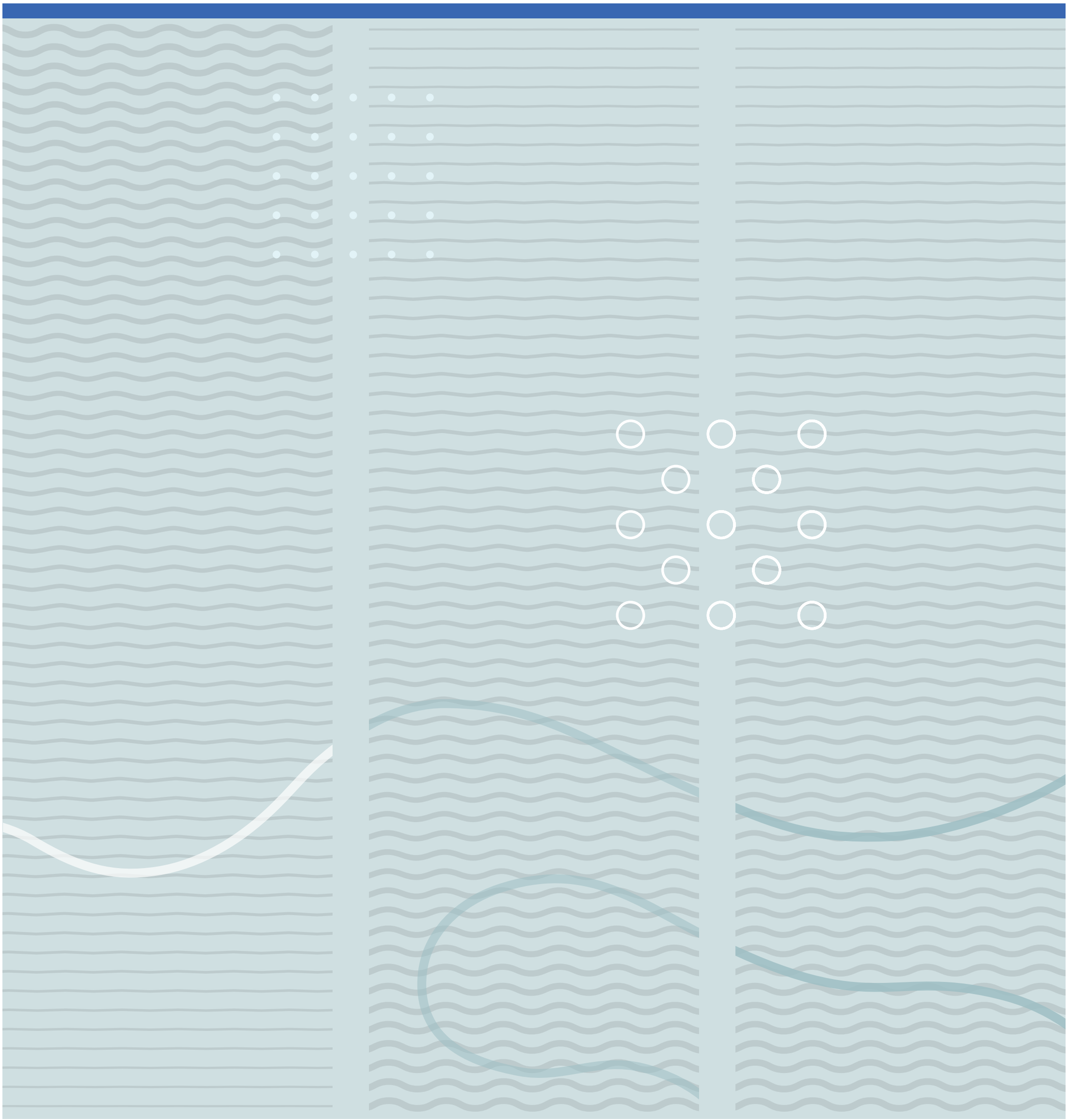

Asmat Nawaz

Perovskite Solar Cells

Improved Active layer Morphology and Pore-filling in TiO2 Nano-Scaffolds

A PhD dissertation in
Applied Micro- and Nanosystems

Faculty of Technology, Natural Sciences and Maritime Sciences
University College of Southeast Norway
Borre, 2018

Doctoral dissertations at the University College of Southeast Norway no. 34
ISSN: 2464-2770 (print)
ISSN: 2464-2483 (electronic)
ISBN: 978-82-7860-318-5 (print)
ISBN: 978-82-7860-317-8 (electronic)

Print: University College of Southeast Norway

Dedication

To my parents who took care of my daughter during my whole PhD period. My lovely daughter who was an infant when I started my PhD and lived without me during these years. My husband, brothers and sisters.

Preface

This thesis is submitted for the degree of Doctor of Philosophy at the University College of South East Norway (USN)-Department of Micro and Nano Systems Technology (IMST)

This doctoral work has been conducted at USN, (Horten, Norway) and in the collaboration with Ege University, Solar Energy Institute, (Izmir Turkey) and Department of Physics, University of Konstanz (Germany) under the supervision of Professor Muhammad Nadeem Akram and Professor Kaiying Wang.

Lånekassen (PhD Quota program) provided financial support. Norwegian PhD Nano-Network and Norfab gave additional support.

Acknowledgement

Foremost, I humbly thankful to almighty GOD for giving me strength and opportunity to complete this PhD thesis successfully.

Though only my name appears on the front cover of this dissertation, but, many great people have contributed to the completion of it. I owe my gratitude to all those people and because of whom my doctoral experience has been one that I will cherish always.

I must offer my sincere appreciation to my principal supervisor Professor M. Nadeem Akram for his constant encouragement and guidance. I could not have imagined a better advisor for my PhD study, who gave me freedom to explore on my own. He has always been there to listen and advice.

I would also like to express my special thanks of gratitude to my co-supervisors, Professor Kaiying Wang and Professor Rehana Sharif for their invaluable support and constructive advice.

I would also like to express my deep gratitude to my external advisors, Professor Lukas Schmidt Mende (Physics dept. Konstanz University, Germany) and Professor Ceylan Zafer (Ege University, Solar Energy Institute, Izmir, Turkey), who gave me opportunity to work in their well-equipped labs with a good support of their research group members.

Beside my advisors, I would like to thank my defense committee members for insightful comments, critical questions and helpful suggestion related to my dissertation work.

I would also like to acknowledge the Faculty of Technology and Maritime Sciences, and especially to the Department of Micro and Nano Systems Technology at University College South East Norway for letting me use the available resources and providing me invaluable administrative guidance during PhD work. I am also thankful to lab engineers Zekija Ramic, M. Tayyib, Ragnar Dahl Johansen, Thomas Martinsen for helping hand in laboratory work and special thanks to Tone Gran, Kristin Skjold Granerød, Knut E. Aasmundtveit, Agne Johannessen and Maija Heinilä for helping in administrative work, encouraging words and emotional support.

I am also thankful to my family and many of my friends that helped me stay sane through these difficult years. I greatly value their friendship. A special thanks to **Azhar Fakharuddin (field supervisor)**, Ka Kan Wong, Pramod K. Singh, Ali Koray Erdinc, Burak Gultekin and Sajad Hussain for helping me a lot during my experimental work.

Abstract

Organometallic halide perovskite solar cells (PSCs) have recently shown tremendous research interest due to their remarkable photovoltaic (PV) performance reaching up to 22% power conversion efficiency in merely five years since their first solid-state high performing device reported in 2012. This high performance stems from judicious selection of charge transport layers and enabling efficient charge extraction at device interfaces, optimization of the perovskite composition such as inclusion of formamidinium (FA) or Caesium (Cs) or both into the commonly employed Methyl Ammonium cation (MA), and a control over perovskite layer morphology. The research work presented in this thesis primarily explores the influence of the perovskite $MAPbI_3$ active layer morphology and crystallinity and the role of selective contacts such as widely employed TiO_2 compact layers and one-dimensional scaffolds on the device performance and stability.

At first, the effect of perovskite morphology was investigated by employing solvent additives and anti-solvent treatment methods on the perovskite films developed via single-step and double-step methods. The solubility of the precursor solution was enhanced by adding a controlled amount of additive (in this case DI-H_2O), resulting in a smooth and uniform $MAPbI_3$ film surface. Similarly, a significant improvement in $MAPbI_3$ morphology was observed upon anti-solvent treatment. The modified films not only showed higher crystallinity, but also a change in the perovskite energy levels. This shift in the energy levels favoured interfacial charge transfer leading to an improvement in open circuit voltage (1.08 V) up from 0.61V for an untreated rival. The effect of anti-solvent treatment on the $MAPbI_3$ films deposited via double-step deposition method was also investigated. Unlike a significant improvement observed for the perovskite films developed via single-step method, we observed no significant difference on the perovskite morphology. We noted that the anti-solvent treatment only works well for initially bad perovskite films with poor surface coverage, and in the case of an already smooth film, it rather decreased the film thickness leading to a drop in light absorption and photocurrent.

We then investigated the role of one-dimensional (1D) TiO_2 electron transport layers (ETLs), namely, TiO_2 nanorods/and nanotubes on the device performance and stability. We particularly focused on improving the commonly observed inferior pore-filling of the perovskite in nanorods/nanotubes scaffolds which is a bottleneck for device performance. We demonstrated a perovskite healing process (recrystallization of $MAPbI_3$ films in the methylamine gas environment) to improve the pore-filling in these 1D nanostructures, which was confirmed via scanning electron microscope imaging. Besides the improved pore-filling fraction upon healing, we also found an improvement in the perovskite crystallinity and formation of large crystal grains. Photoluminescence and electrical characterizations demonstrated an improved charge transfer in the healed films compared to their pristine analogous. We also observed a significant improvement in the power conversion efficiency and stability under continuous light soaking in perovskite solar cells fabricated using the healed perovskite films.

List of papers omitted in this online paper due to publisher's restrictions

Article 1

Morphology Study of Inverted Planar Heterojunction Perovskite Solar Cells in Sequential Deposition, Asmat Nawaz, Ali Koray Erdinc, Burak Gultekin, Ceylan Zafer, Muhammad Tayyib, Kaiying Wang, M. Nadeem Akram, International Journal of Electrical, Computer, Energetic, Electronic and Communication Engineering, Vol:10, No:7, 2016 (Extended form of conference article, ICREET, UK, 2016, oral presentation, best oral presentation award).

My contribution: material synthesis, device fabrication, characterization, analysis, manuscript preparation

Article 2

Insights into optoelectronic properties of anti-solvent treated perovskite films, Asmat Nawaz, Ali Koray Erdinc, Burak Gultekin, Muhammad Tayyib, Ceylan Zafer, Kaiying Wang, M. Nadeem Akram , Ka Kan Wong, Sajad Hussain, Lukas Schmidt-Mende, Azhar Fakharuddin, J Mater Sci: Matser Electron, pp. 1-7, 2017.

My contribution: material synthesis, device fabrication, characterization, analysis, manuscript preparation.

Article 3

Improved pore-filling of TiO_2 nanorods and nanotubes scaffolds for perovskite solar cells, Asmat Nawaz, Ka Kan Wong, Carola Ebenhoch, Eugen Zimmermann, Zhaoke Zheng, Muhammad Nadeem Akram, Julian Kalb, Kaiying Wang, Azhar Fakharuddin, Lukas Schmidt-Mende, submitted to, ACS Applied materials & Interfaces.

My contribution: material synthesis, device fabrication, characterization, analysis, manuscript preparation.

Other articles not included in this thesis

1.**Efficient dye sensitized solar cell and supercapacitor using 1-ethyl 3-methyl imidazolium dicyanamide incorporated PVDF–HFP polymer matrix**, Asmat Nawaz, Rehana Sharif, Hee-Woo Rhee, Pramod K. Singh, Journal of Industrial and Engineering Chemistry 33, 381–384, 2016.

2.**Review: Non-Invasive Continuous Blood Glucose Measurement Techniques**, Asmat Nawaz, Per Øhlckers, Steinar Sælid, Morten Jacobsen , M. Nadeem Akram, Bioinformatics and Diabetes**,** 1, 54-78, 2016.

Abbreviations

PV: Photovoltaic

PSCs: Perovskite solar cells

VBM: Valence band maxima

CBM: Conduction band minima

J_{SC}: Photocurrent density

V_{OC}: Open circuit voltage

FF: Fill factor

PCE: Power conversion efficiency

R_{Sh}: Shunt/parallel resistance

R_S: Series resistance

ETM: Electron transport material

HTM: Hole transport material

ETL: Electron transport layer

HTL: Hole transport layer

MA/CH_3NH_3: Methylamine

MAI/CH_3NH_3I: Methyl Amine Iodide

PbI_2: Lead iodide

DMF: Dimethylformamide

GBL: γ- Butyrolactone

SS: Single-step

DS: Double-step

ss: Steady-state

DI-H_2O: Deionized water

HCl: Hydrochloric acid

IPA: Isopropyl alcohol

TL: Toluene

$MAPbI_3/CH_3NH_3PbI_3$: perovskite

1D: One-dimensional

TNRs: Titania nanorods

TNTs: Titania nanotubes

XRD: X-ray Diffraction

PL: Photoluminescence

TRPL: Time resolved photoluminescence

PESA: photoelectron spectroscopy in air

SEM: Scanning electron microscopy

TEM: Transmission electron microscopy

Table of contents

Chapter 1

Chapter 1 presents an overview of photovoltaics along with a detailed description of the properties of perovskite material, device architectures and working mechanism of the perovskite solar cell (PSC). Morphology engineering of the perovskite film through various deposition routes and role of selective contacts is also reviewed in this chapter.

1 Introduction and literature review

1.1 Motivation and overview of photovoltaics

Currently, the world is facing global warming mainly due to the emission of the greenhouse gases from burning coal and oil [1] [2]. An important challenge for mankind is to find affordable, clean and sustainable energy sources at large scale to meet today's energy requirements. The energy supplied on the earth by the solar radiation is an efficient and feasible source to harvest and convert into electricity. Photovoltaic (PV) solar cells, capable of converting solar energy directly into electrical energy, are an alternative that have potential to meet the entire world's energy demand [3]. The PV devices can be divided into three categories. (1) First generation solar cell, (2) second generation solar cell and (3) third generation solar cell often also termed as future generation solar cells [4]. First generation solar cell is composed of silicon (Si) wafers (monocrystalline and polycrystalline). The monocrystalline Si homo-junction and hetro-junction cells have 25.1% and 25.6% efficiencies respectively, whereas the polycrystalline Si cells have 20.8% efficiency [5]. Under thermodynamic consideration of detailed balance, the maximum efficiency of Si based single junction solar cells (absence of nonradiative recombination) is limited to 33.5% for AM1.5G spectrum at 25 °C and referred to as Shockley Queisser (SQ) limit [6]. At present, silicon solar cells (wafer technology) dominates and taking up ~ 93% [7] of the global PV installation market with PCE of commercial modules of around 20% and lifetime of more than 20 years. The cost of silicon modules dropped down significantly from ~70$/WP in 1970s [8] to ~0.36 $/WP in 2017 [9]. Figure 1.1 shows the global cumulative PV installed capacity until 2018 [10].

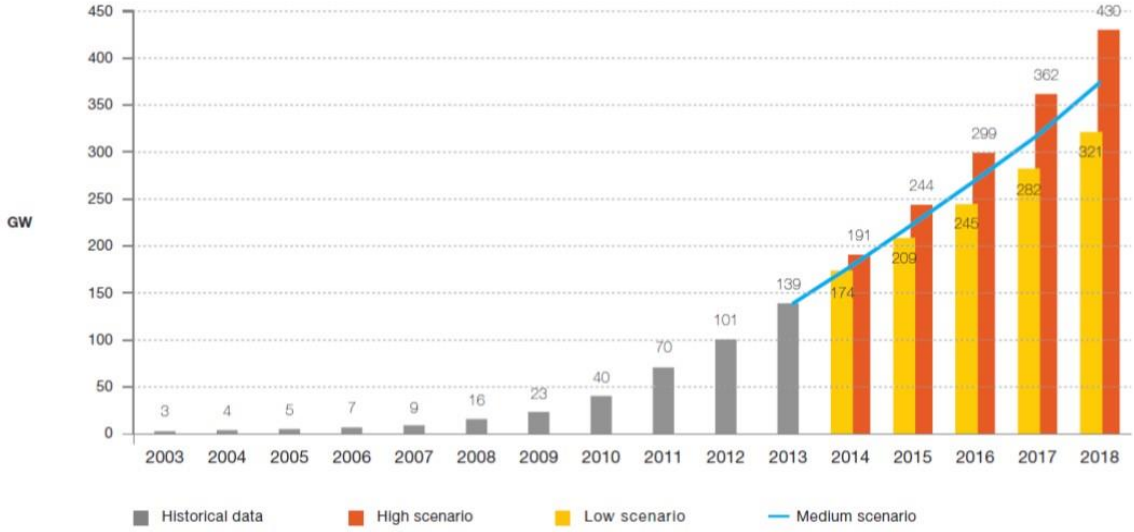

Figure 1.1: Global PV cumulative scenario until 2018 [10].

However, the main disadvantage is that Si technology needs expensive materials with higher processing temperature, which means that the production is still expensive [5] [11]. Second generation solar cells are based on ‘thin film’ technology that consists of semiconductor materials such as copper indium gallium diselenide (CIGS-21.7%), single crystalline gallium arsenide (GaAs-28.8%) and poly-crystalline cadmium telluride (CdTe-21.5%) showing promising efficiencies [5]. Multi-junction solar cells surpass SQ limit due to several absorber layers for harvesting light in different regions of the solar spectrum and have reached highest power conversion efficiency (PCE) of 38.8% under one sun condition with a five junction (GAInAs/GAInP/GaAS/AlGaInAs/AlGaInP) tandem geometry. However, a big challenge for the PV community with these solar cells is the high production cost [5]. **Fig 1.2** is taken form National Renewable Energy Laboratory (NREL) website that shows the best solar cells efficiencies reported so far [12]. Researchers have pushed towards new kinds of solar cells and developed ‘third generation’ solar cells to overcome the limitations of the previous solar cells and tried to reduce high production cost [4]. Though, the efficiencies of third generation solar cells are relatively low as compared to Si/multi-junction solar cells, but they have low production cost due to cheap fabrication processing techniques. This makes third generation solar cells appealing to the PV community.

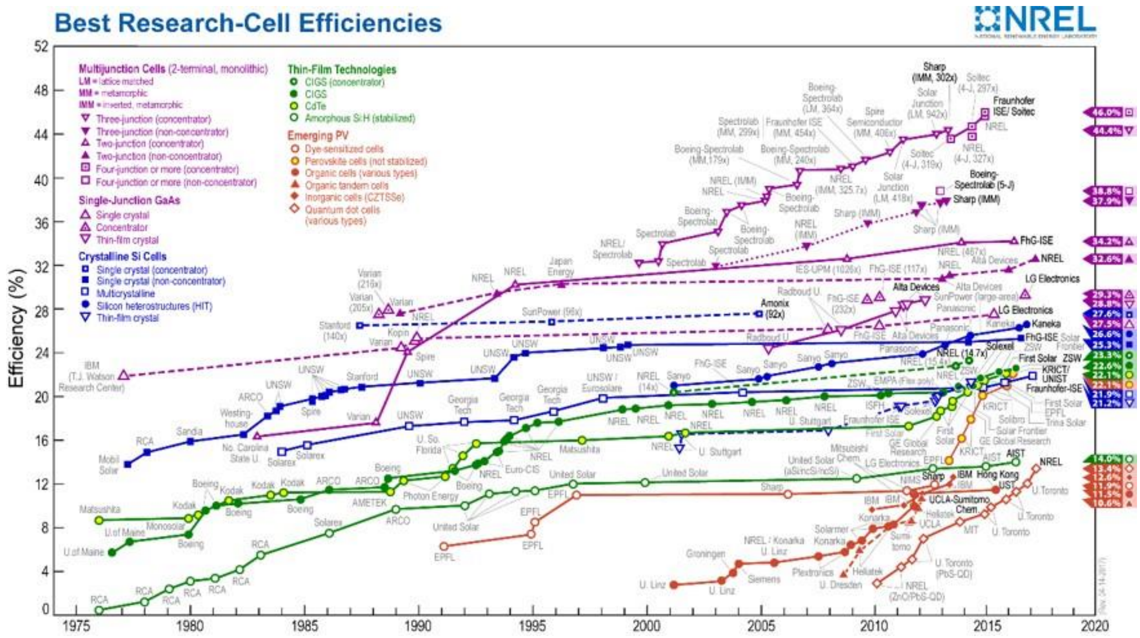

Figure 1.2: Best solar cells efficiencies, Taken form National Renewable Energy Laboratory (NREL) website [12].

In recent years, solution processed photovoltaics have attracted significant interest due to their high power conversion efficiency (PCE), cost effective fabrication, and added functionality such as flexibility, being aesthetic and light weight. In 1991, the first development was based on dye-sensitize solar cells (DSSCs) [13], which now demonstrate 14.3% efficiency [14]. The most recent breakthrough in the field of third generation solar cells is the development of organic-inorganic halide perovskite solar cells that now demonstrate an efficiency about 22% [15]. Progress of perovskite solar cells has been remarkably impressive as these can be fabricated by solution processing at low temperatures and the production requires less energy than Si solar cell. Coupling of

PSCs with c-Si and/or CIGS solar cells in a tandem geometry is considered a novel approach in order to reduce the overall cost of energy generation (cost-efficiency balance) and also to enhance the PCE of single junction solar cells beyond the SQ limit. Tandem solar cells can be fabricated in three different ways: (1) Mechanically stacked solar cells, termed as 4-termial (4T), (2) Monolithic solar cells, termed as 2-terminal (2T) and (3) optical splitting tandem solar cell [16]. Recently, 26.4% PCE has been reported with mechanically stacked configuration [17]. A focus on tandem devices is due to their easy integration and printability on existing PV technology, as PSCs can easily be printed via solution processing techniques. Another potential market advantage of the PSCs is the deployment of flexible PV technology. It is not only interesting due to the quest for low cost manufacturing and high-throughput but also by considering its properties of being lightweight, flexible and thin, that would make it easy to integrate on any surface (e.g. building integrated photovoltaics (BIPV), automotive integrated photovoltaics (AIPV)) or structure (either curved, rigid, or flexible) and even in portable and indoor electronics [8].

Despite the high efficiency reports, the PSCs still suffer from issues such as: long-term operational stability, toxicity (the most efficient device employ lead, Pb), and reproducibility. The reproducibility arises from their rapid crystallization, which largely depends on the processing conditions and also the substrate or the selective contacts underneath [18]. For a high efficient device, the choice of selective contacts is crucial for efficient charge extractions as well as its stability as perovskite deposition on metal oxides such as ZnO and TiO_2 has shown degradation due to a possible interfacial reaction [19] [20].

1.2 Perovskite solar cell

1.2.1 Base technology

The base technology for PSCs is solid-state solar cells (SSCs), which are based on Gratzel dye sensitized solar cells. In 1991, Gratzel and Regan developed a low cost photo-electrochemical solar cell based on dye sensitized nano-crystalline TiO_2 film [13], which now demonstrate 14.3% PCE [14]. However, issues such as liquid electrolyte usage raised concerns with leakage [21]. Therefore, liquid electrolytes are replaced by solid electrolytes without any change in the basic structure and concept of DSSCs [22]. **Fig 1.3(a)** shows device structure of SS- DSSC and **(b)** shows the energy landscape of SS-DSSC along with chemical structure of Spiro-OMeTAD, most commonly employed hole transport material (HTM) [23] . In SS-DSSCs, hole transfer between dye and Spiro-OMeTAD occurs at similar rates as the electron injection from dye to TiO_2, whereas in conventional DSSCs, the transfer of electron is several orders of magnitude is faster than the dye regeneration. [23].

In 1998, Udo et al. first time employed Spiro-OMeTAD as HTM in SS-DSSC [22]. The conductivity and hole diffusion length in HTMs should be considered simultaneously because they limit the mesoporous TiO_2 film thickness. TiO_2 film thickness should be matched to the reciprocal of the absorption coefficient, so for higher absorption coefficient, thinner TiO_2 film are needed and vice versa. When using Spiro- OMeTAD, the thickness of TiO_2 film is limited to around 2µm [24] [25]. Therefore, no substantial improvement is expected in the SS-DSSCs because most of the molecular organic dyes having absorption coefficient ~ $10^3 cm^{-1}$ [26]. This would need ~10µm thick film for sufficiently harvesting the incoming light [25]. For higher PCEs, there is a need of new sensitizer with absorption coefficient over $0.5*10^4 cm^{-1}$. The light harvester organo-lead halide perovskite shows a significant leap because of its high absorption coefficient of $1.5*10^4 cm^{-1}$ [26].

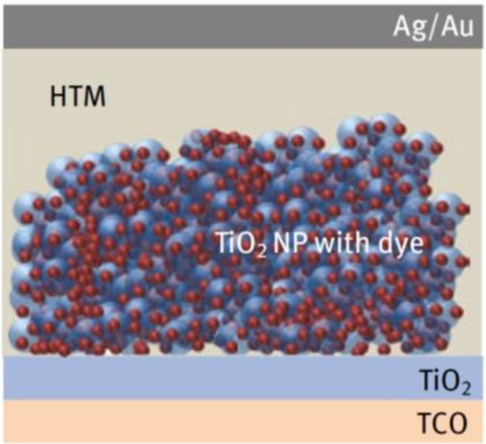

Figure 1.3(a): Schematic illustration of device structure of SS- DSSC (TCO: Transparent conducting oxide, NP: Nano particle [23].

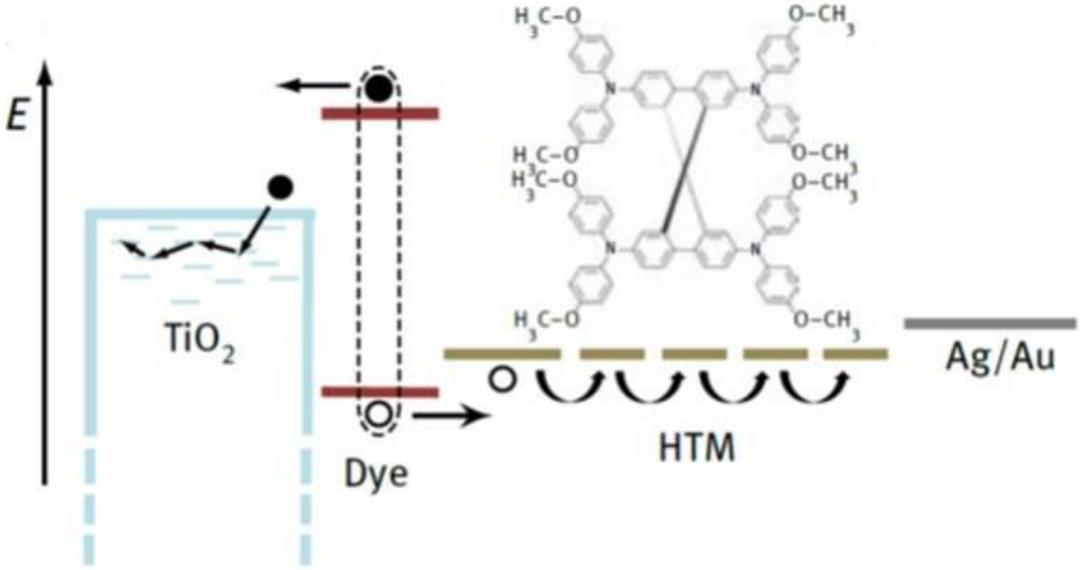

Figure 1.3(b): Working principle of SS-DSSC [23].

1.3 Material properties

1.3.1 Crystal structure and phase transition

The general formula of the perovskite crystal structure is AMX_3, where A represents organic cations, M represents a divalent metal cation [27] such as (Co^{+2}, Cu^{+2}, Fe^{+2}, Cr^{+2}, Cd^{+2}, Pd^{+2}, Mn^{+2}, Sn^{+2}, Ge^{+2}, Pb^{+2}, Yb^{+2} or Eu^{+2}) and X represents halide anions such as (Cl^-, Br^- or I^-). Recently, most investigated halide perovskite consist of $CH_3NH_3^+$ (MA), $HC(NH_2)_2$ (FA) or Cs^+ as A, and Sn^{+2}or Pb^{+2} as M [28]. The perovskite crystal structure is described as a three dimensional arrangement of a corner sharing octahedral MX_6 unit, with cation A, sited in the cubo-octahedral interstices. Ideally, the perovskite structure is cubic as shown in **fig 1.4** [25]. Perovskite structure formation is estimated by using Goldschmidt’s tolerance factor ‘t’ as described in the following equation:

$$t= (rA+ rX) / 2^{1/2} [rM +rX]) \qquad (1.1)$$

where rA, rM and rX are effective ionic radii for A, M and X ions, respectively [29]. A modification in the combination of anions and cations result into different perovskite crystal sizes, band gaps, stability and performance of the devices. This unique perovskite structure exhibits interesting characteristics, that is: low exciton binding energy [30], high absorption coefficient [31], tuneable bandgaps [32], high ambipolar charge carrier mobilities [33] and long electron and hole diffusion lengths [34].

The structure of organic/inorganic perovskite is highly influenced by the size of organic cation. A 3D perovskite crystal structure remains the same with smaller size of the organic cation (commonly used Methyl Ammonium, MA). However, with larger cation, layered structure forms with inorganic layers, alternating with organic layers, connected with van der Waals forces. The 3D perovskite ($CH_3NH_3PbI_3$) crystal structure has four solid phases- three perovskite (α, β and γ) phases and one non-perovskite (δ) phase. α-phase is found with pseudo-cubic structure at high temperatures (T > 327K) and a phase transition from α to β occurs at temperature below 327K. The MA cation is disordered in both α and β phases and for its reorientation, a ferroelectric response is required. An orthorhombic (γ) phase occurs at temperature (T<162K), where MA cations are ordered. The degree of rotation of MA ions has been investigated at different phases, and at high temperatures, rapid rotation and at low temperatures, no rotation is observed. This molecular motion of cation leads to a highly ordered arrangement along C−N axis. This is the reason for phase transition from cubic-tetragonal-orthorhombic phase as temperature is lowered. The fourth non perovskite phase (δ) occurs in solvent environment and the structure behaviour is still unclear in this phase [23].

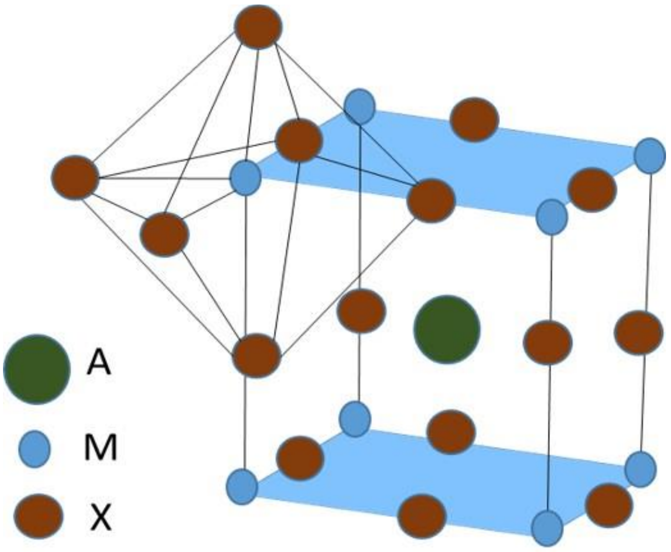

Figure 1.4: Perovskite cubic structure of MX_6 octahedral and larger cation A occupied in cubo-octahedral site.

1.3.2 Optical bandgap engineering

The perovskite ($CH_3NH_3PbI_3$) has estimated band gap value of 1.50-1.6 eV [35] [36]. Due to comparatively short absorption wavelength, limited to 800nm, band gap engineering is required for absorption of longer wavelengths without compromising the absorption coefficient. One approach to tune the band gap (modification M-X-M bond length and angle) without affecting the valence band maxima (VBM), is the replacement of MA organic cation with formamidinium. By using formamidinium, a reduction in the band gap of about 0.07eV is found that gives an extension in the absorption wavelength up to 840nm. Another approach to tune the band gap is a direct modification in M-X bond. Modification in metal cation has a significant effect on the conduction band minima (CBM) and VBM. In $CH_3NH_3PbI_3$, it is estimated that CBM is composed of s-antibonding states of Pb 6p and I5s orbitals, and VMB is composed of mainly s-antibonding of Pb 6s and I5p. The replacement of Pb^{+2} with Sn^{+2} results into a change in the positions of VBM and CBM, and thus the band gap changes from 1.55eV to 1.17eV [36]. Eperon et al. showed that halides have the ability to tune the band gaps. They reported that formamidinium lead iodide ($FAPbI_3$) has narrow band gap value (1.48eV) and by using a mixture of halides such as $FAPbI_X Br_{3-X}$, band gap value can be tuned between 1.48eV to 2.23eV [37]. **Fig 1.5** shows the schematic energy level diagram for the possible combinations of the perovskite materials [36].

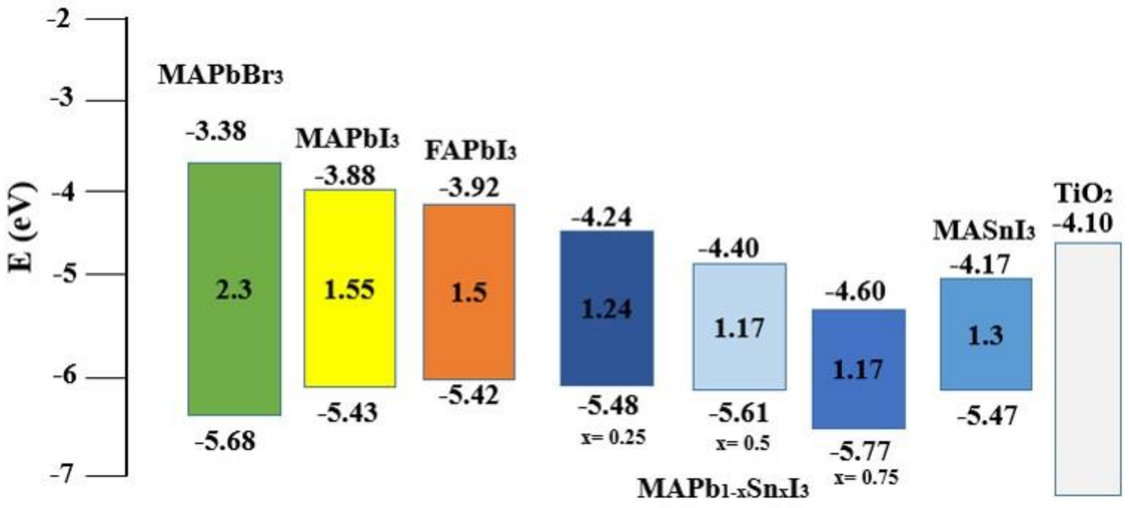

Figure 1.5: Schematic illustration of energy level diagram by using different combinations of perovskite material [36].

1.3.3 Balanced charge-transporting behaviour

To further, understand the performance of the solar cell, hole and electron diffusion lengths of the active material should be examined. By using diffusion coefficient (D) and recombination life time τ, the average diffusion length (L_D) of charges is calculated with the help of following equation:

$$L_D = \sqrt{D\tau} \qquad (1.2)$$

Recently, Xing et al [38] and Stranks et al [34] demonstrated balanced charge transport properties of the perovskite material. By measuring transient absorption and photoluminescence (PL) spectroscopy, it is reported that for triiodide ($CH_3NH_3PbI_3$) the electron- hole diffusion lengths are L_D^e ~130nm and L_D^h ~105nm respectively, and for chloride ($CH_3NH_3PbI_{3-x}Cl_x$) based perovskite, the electron-hole diffusion lengths are L_D^e ~1069nm and L_D^h ~1213nm respectively. To get efficient charge extraction, diffusion lengths of the charge carriers need to exceed the layer thickness, ensuring that most of electron-hole pair can be transported before recombination [34].

1.4 Structure evolution and photovoltaic action of PSCs

Organic-inorganic halide perovskite has been known for applications in field-effect transistors [39] and optical devices [40] [41]. However, its usefulness in photo energy conversion devices is recognised in 2009 by Kojima et al. [42]. They employed halide perovskite as an absorber on the TiO_2 (8-12 µm) layer, a similar device architecture to DSSCs and demonstrated 3.8% PCE. Subsequently, Park et al. [43] reported 6.5% PCE in similar device architecture with lower thickness (~4µm) of TiO_2 film. However, a poor operational stability was shown in these devices, because of liquid electrolyte.

In 2012, first solid state PSC was developed with PCE up to 9.7% [31]. Solid HTM not only solved the stability issue, but also enhanced the PCE. The state-of-the-art PCE of PSCs (20%-22%) is achieved by (i) optimization of electron transport layer (ETL) and hole transport layer (HTL) for better charge extraction (ii) chemically modifying of $CH_3NH_3PbX_3$ by incorporating Caesium and formamidinium together with MA and introducing mixed halides such as PbI, PbBr and PbCl, (iii) morphology controlled optimization of the perovskite film [44] [45] [46] [47] [48].

In a typical PSC device architecture, a perovskite absorber layer is usually employed between the ETL and HTL that creates two interfaces, ETL-perovskite and HTL-perovskite interface. There is a wide variety of PSCs architectures which is determined by charge (p or n-type), morphology (mesoporous or thin film) and electrical properties (insulating or conducting) of ETL/HTL on the conducting substrates making it p-i-n or n-i-p, n-p or p-n, planar or mesoporous PCSs as shown in **fig 1.6** [49]. This makes it difficult to generalize the operating principle for all these devices, and consequently, numerous physical processes such as hysteresis, origin of instability and charge transfer mechanism are still not completely understood [18] [49].

The first solid PSC consists of perovskite absorber layer, which is employed between an ETL on a conducting substrate (FTO) and a HTL (**Fig 1.6a**) with a metal back contact. This architecture holds state-of-the-art performance ~20-22% due to (i) pin-hole free hole blocking layer between FTO and TiO_2, (ii) optimized interfaces (iii) a compact perovskite capping layer over TiO_2 after infiltration of the perovskite within the pores [48] [50]. In other architecture (**Fig 1.6b**), there is a replacement of mesoporous conducting TiO_2 scaffold with an insulating Al_2O_3 layer that showed PCE ~15.9% [51]. This is evidence of an ambipolar charge transport behavior in the perovskite film. The devices having insulating scaffold exhibited higher charge carrier lifetime compared to TiO_2 scaffold counterparts because of TiO_2 that contribute in charge collection having low electron mobility and sub-band gap states, which leads to interfacial recombination [44].

Alternatively, the devices without mesoporous TiO_2 scaffold termed as planar (**Fig 1.6c**) have shown remarkable performance (PCE ~19 –20%), with hysteresis [52] [53], where a dense layer (usually TiO_2 layer) is employed to avoid direct interaction of the perovskite or HTM with FTO. The PSCs without HTL [54] and an ETL [55] (**Fig 1.6d and e**) have also been fabricated and shown significant performance 14-16%. Moreover, inverted solar cells architectures in which holes are collected at FTO/ITO instead of electrons have also been reported (**Fig 1.6f**) having PCE >18% [56].

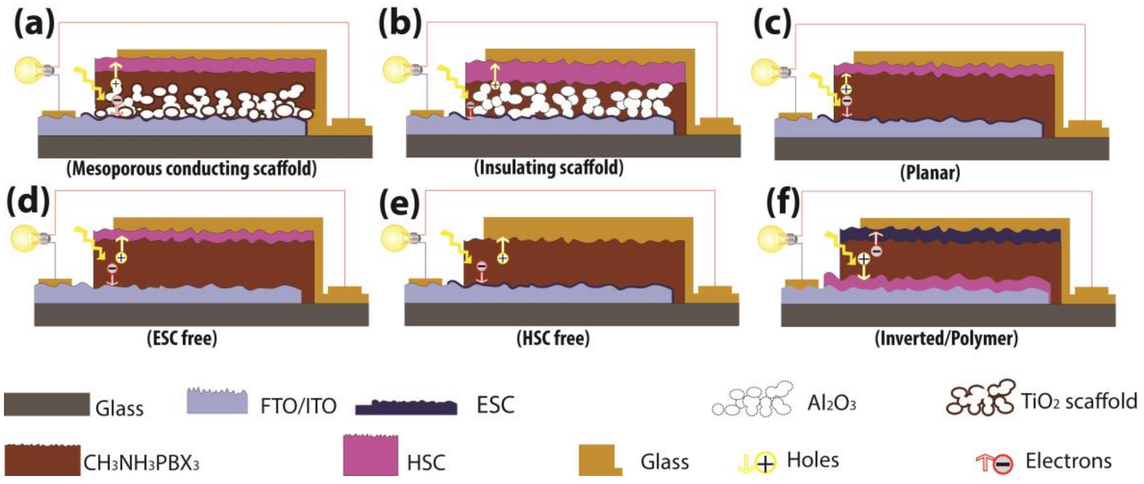

Figure 1.6: Schematic illustration of structure evolution of PSCs: (a) a metal oxide semiconductor (MOS) mostly mesoporous TiO_2 is employed as ETL (b) MOS is replaced by insulating scaffold (Al_2O_3 or ZrO_2) (c) planar architecture in which replacement of MOS/scaffold to compact ETL (d) free from ETL (e) free from HTL (f) inverted architecture in which P-type layer is employed to FTO such that holes can be collected through FTO/ITO [49].

For the PSCs, their performance over time and hysteresis in current–voltage (J-V) characteristics mainly depends on the morphological and electrical properties of the selective contacts. The perovskite morphology and crystal size mostly depends on the nature of ETL/HTL–$CH_3NH_3PbX_3$ interface [57] [58] [59]. Moreover, for practical devices, not only PCE but also operational stability determines the success of the technology in real life application.

1.5 Working principle of PSC

A simplified working principle of PSC involves the absorption of photons by perovskite absorber layer. The perovskite absorber has low exciton binding energy that indicates free charge carrier generation upon the photon absorption and it occurs in few picoseconds. These generated free charge carriers further transport to the respective interface contacts. During the transfer process **(Fig 1.7)**, desirable process (blue arrow) occurs in three steps:

photo-excitation in perovskite absorber (1), transfer of electrons to ETL (2), transfer of holes to HTL (or equivalently transfer of electrons from HTM to perovskite) (3). A numerous undesirable processes (black arrow) may occur that consist of recombination of photo-generated species (4), back charge transfer at the interfaces of HTM and TiO_2 with perovskite (5, 6) and a direct contact between HTM and TiO_2 (7). Eventually, after overcoming the extraction barriers at the interfaces, the remaining charge carriers can transfer through selective contact interfaces and can be extracted by the respective electrodes [60].

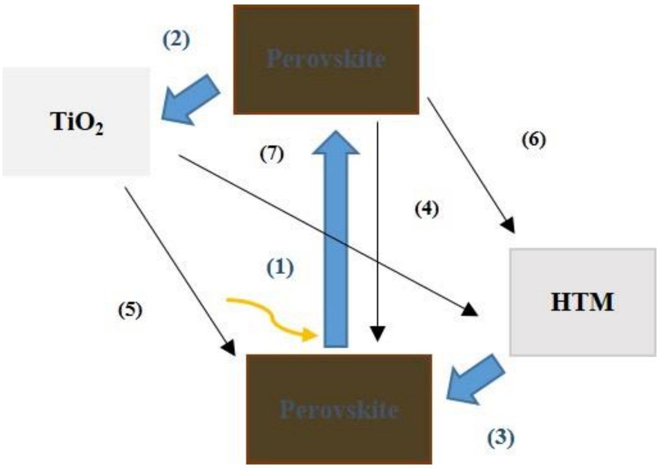

Figure 1.7: Schematic illustration of electron transfer and recombination process in PSC. The thick blue arrows shows desirable process and thin black arrows shows undesirable process.

(a) Charge generation

The significant question regarding charge generation is whether the photo-excited species have excitonic nature or non-excitonic nature. Low exciton binding energies (~2 meV) in perovskite determine that charge generation is non-excitonic. Hence, the efficient generation of free holes and electrons in one-step is one of the major advantages of PSCs [61].

(b) Charge transport and recombination

In semiconductors, transport of charge carriers is related to the electronic band structure and most importantly, the hole and electron effective masses and mobility. In perovskites, these effective masses are quite closer to inorganic semiconductor such as GaAs that largely benefits from the strong spin-orbit coupling effect in the electronic band structure because of the existence of heavy atoms such as Pb. This strong spin-orbit coupling leads to the reduction of band gap and significantly modifies electron-hole effective masses [62] [63] [64].

An important parameter in solar cells is charge carrier life-time that defines time window, to extract the charges efficiently at selective electrodes before recombination. The decay of the free charge carrier density can be expressed in terms of a rate equation:

$$dn/dt = -k_3^{n3} - k_2^{n2} - k_1^{n} \qquad (1.3)$$

where k_1 = rate constant related with trap state recombination, k_2 = rate constant related with radiative or direct or band–to-band recombination and k_3 = rate constant related with augur recombination that strongly depends on the carrier charge density [65]. Numerous studies show that in PSCs, the dominant recombination is non-radiative trap assisted recombination that it mainly decreases the value of V_{OC} [66]. **Fig 1.8** shows the schematic illustration of all three recombination in PSCs.

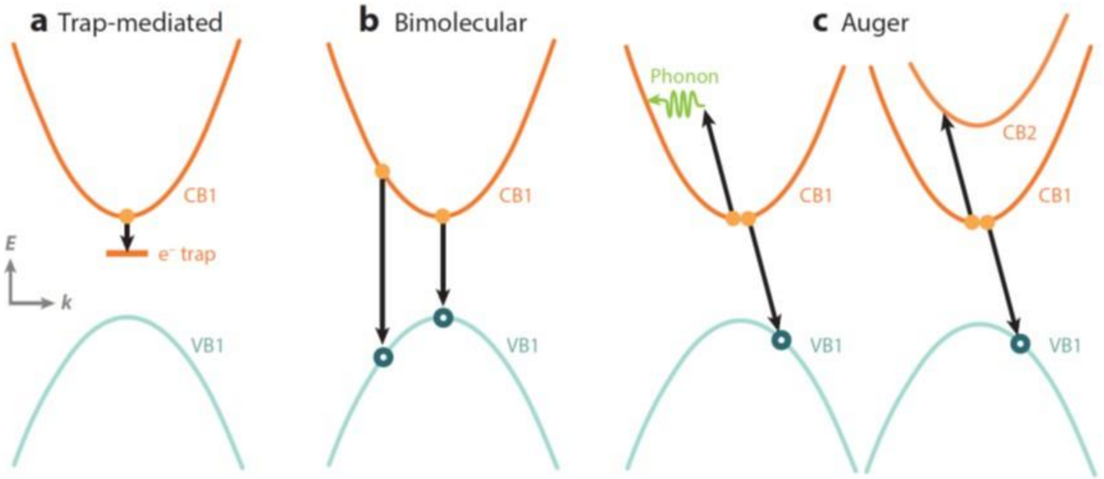

Figure 1.8: Schematic illustration of all three-recombination process in PSC (a) trap assisted recombination involving capture of either electron or hole in the trap state (i-e defects) (b) bimolecular or radiative or band-to-band recombination involving a direct recombination between electron and hole from band-to-band, (c) augur recombination involving transfer of energy of an electron (or hole) to other charge carrier to allow non-radiative recombination either with electron (or hole) [65].

(c) Charge extraction

To extract charges efficiently from PSCs, it is necessary to select the ETL and HTL's with favourable band alignments (both VB and CB) with the perovskite layer. Additionally, balanced charge transfer at interfaces is also important for improvement in the PV performance [67].

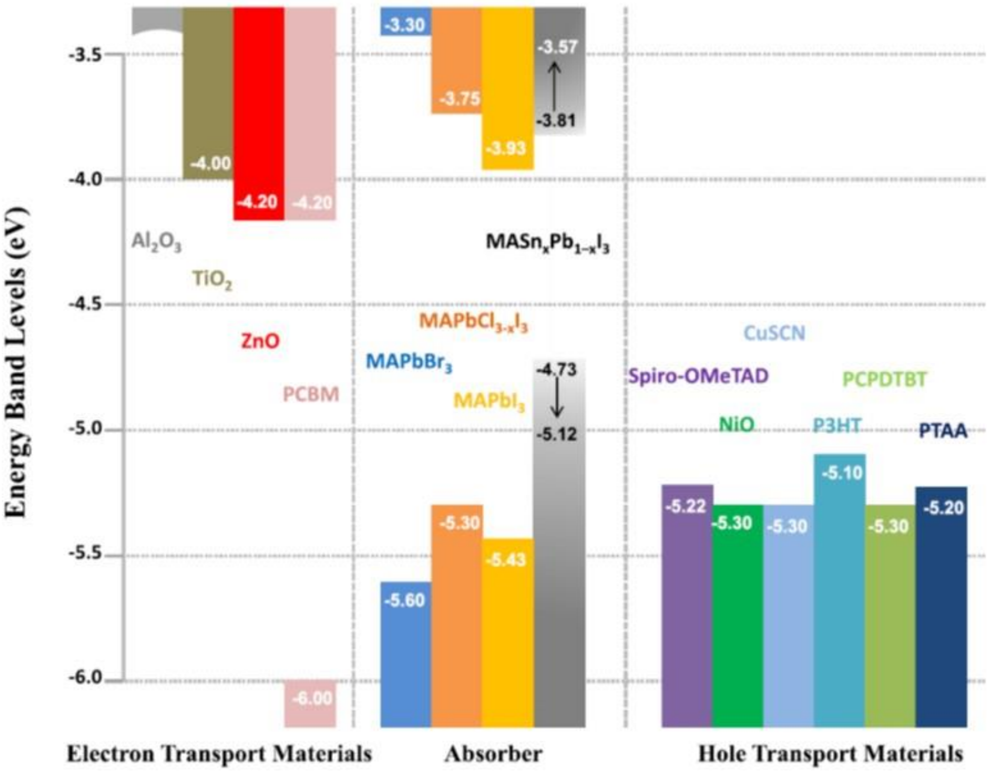

Figure 1.9: Band alignment diagram of ETM's and HTM's used for PSCs [68].

1.6 Challenges with PSCs: Hysteresis and Degradation

In spite of significant achievements in the PCE of PSCs, stability is one of the critical issues prior to its commercial deployment. It depends on numerous factors, both intrinsic, such as perovskite structural and chemical stability and extrinsic, such as moisture, oxygen, light and heat that limit their life-time to few hundred hours only [69] [70]. Perovskite ($CH_3NH_3PbX_3$) materials are stable, both chemically and structurally, but due to hygroscopic nature of the organic cation, moisture induced degradation happens. Substituting or mixing of MA cation with Caesium and/or formamidinium can improve the stability of perovskite towards moisture and heat [47] [48]. A recent study using FTIR spectroscopy shows that evaporation of MAI during film fabrication itself initiate the instability, suggesting that the active layer film fabrication is an essential step for the stability of PSCs [71].

Hysteresis is related with ionic motion in the perovskite and nature of contacts that can affect the PV characteristics (i.e., variation in the J-V curves for different scan rates), and it is detrimental to the device stability [70]. Oxidation and photo-oxidation have been seen for perovskite films but are less severe in full devices, depending on the hydrophobic nature of the top layer [72], and can be avoided by appropriate encapsulation under inert conditions that enables solar cells to be stable for up to 1000 h [44].

1.7 Morphology engineering of perovskite films

To obtain high performance PSCs, controlled morphology of the perovskite film is a critical issue [73] [74]. The fabrication of PSCs involves deposition of the perovskite thin film, ETM and HTM layers via solution process methods. The preparation of perovskite film typically involves stoichiometric reaction of organic halide, mostly CH_3NH_3I, with a metal halide, mostly PbI_2. In the planar heterojunction perovskite solar cells [75], a direct approach applied by different research groups is to increase the thickness of the perovskite layer to maximize the photon harvesting. However, it is not straightforward as it looks due to the quality of perovskite film and consequently shunting pathways and absorption quality are directly related to the crystallization behaviour of the perovskite. The crystallization of $CH_3NH_3PbI_3$ starts at room temperature (R.T.), which is associated with change in colour— a yellow coloured PbI_2 film immediately turns into light brown colour upon reacting with CH_3NH_3I and further annealing it transform into dark brown colour that demonstrates a complete conversion of the perovskite. A good control of the perovskite crystallization is essential to get smooth and highly crystalline films that are thick enough to absorb maximum incident light and thin enough to enable a complete charge collection. It must also be pin-hole free to avoid a direct contact between HTM and ETM, with less grain boundaries [18].

In order to tune the perovskite morphology, there are various perovskite deposition routes such as: single-step (SS), double-step (DS) and Methyl Amine defect healing (MIDH), vacuum assisted vapour deposition (VAVD) and dual source evaporation (DSE). Both SS and DS are solution-processed routes which have shown remarkable PCE beyond 20%.

1.7.1 Single-Step (SS) deposition

A SS deposition of the perovskite film signifies a facile and low-cost route towards high performance PSCs. The perovskite layer is deposited from a solution of both CH_3NH_3X and PbX_2 (X = Cl, Br, I) in a polar solvent, like γ-butyrolactone (GBL) [76], dimethyl formamide (DMF) [77], dimethyl sulfoxide (DMSO) or mixed solvents [45]. Spin coating is a common technique that is employed at lab scale, but other techniques such as blade [78] and slot die coating [79] suitable for large areas have also been demonstrated. Afterwards, annealing is required for the evaporation of the solvent and crystallization of the perovskite film. It is usually carried out on a hot plate at 70-110 ℃ for several minutes to few hours but can be reduced to few seconds by NIR [80] and flash annealing [81] respectively. In a planar geometry, the mixed halide $CH_3NH_3PbI_{3-x}Cl_x$ in a DMF solution, without any additives and thermally annealed with Spiro-OMeTAD as HTM has yielded 15.9% PCE with an alumina scaffold [51].

In spite of its simplicity, a significant issue of SS deposition is the lack of control over the crystallization process that depends on many factors such as precursor compositions, choice of solvents, deposition methods and types of surfaces. As a result, enormous morphological variations occur, leading to rough, inhomogeneous and partly covered layers that reduce incident light absorption and increase the carrier recombination rate, ultimately causing a drop in both reproducibility and device efficiency. Optimizing the perovskite morphology and a complete surface coverage in SS deposition method is crucial and many methodologies have been reported so far, mostly to control the crystallization kinetics [18] [57] [82].

The crystallization rate of the perovskites can also be controlled by including additives in the precursor solution, because the use of additives enhances the solubility of the precursor in the solvent [57]. There are various kind of additives in the literature such as hydroiodic acid (HI) [37], hydrochloric acid (HCl) [83], 1,8-diiodooctane (DIO) [84], 5-ammoniumvaleric iodide (5-AVA) [85], N-cyclohexyl-2 pyrrolidone (CHP) [86], deionized water (DI-H_2O) [87] [88] [89] that are used to get uniform and defect free perovskite morphology, which leads towards higher efficiency.

Seok et al. demonstrated solvent engineering approach (mixture of two solvents GBL & DMSO) for perovskite film by dripping toluene (anti-solvent treatment) during spinning. This report is a breakthrough for controlling the morphology of the perovskite film that leads to improvement in the PV parameters of the solar cell. In this study, $CH_3NH_3 Pb(I_{1-x}Br_x)_3$ is used, and anti-solvent treatment seems to remove all the residues of DMSO during the formation of an intermediate phase MAI-PbI_2-DMSO that results in uniform and smooth perovskite films with low surface roughness [45]. Researchers have used this anti-solvent treatment on different perovskite structures such as mesoscopic TiO_2/perovskite [58], and planar architectures [76] [88] [90].

Priya et al. investigated three different types of anti-solvents such as dichloromethane (DCM), chlorobenzene (CB) and toluene (TL) on bromide based perovskite ($CH_3NH_3PbBr_3$) films. The anti-solvents act like a driving force for crystallization as it reduces the Gibbs energy. TL is non-polar anti-solvent followed by CB and DCM. In this regard, it has larger driving force than other anti-solvents. That is why toluene treated perovskite films are more homogenous, smoother and denser than others [91].

Wang et al. reported a strong dependency of the stoichiometry ratio on $CH_3NH_3PbI_3$ morphology. It was observed that the perovskite morphology is very sensitive with respect to precursor's composition, and a non-stoichiometry ratio leads towards higher efficiency. Under the same deposition conditions with the precursor ratio (CH_3NH_3I : PbI_2 1:1), a rough morphology with microfibers was obtained. However, by decreasing the amount of PbI_2, the formation of uniform film with fewer pinholes was achieved [92].

The solvent-solvent extraction method avoids thermal annealing step for SS deposition The perovskite coated substrate, immediately after spin coating is immersed in a bath of low boiling-point (anti) solvent, such as diethyl ether at room temperature. The efficient extraction of the precursor-solvent induces rapid crystallization of ultra-smooth, uniform perovskite films of controlled thicknesses [93].

The dual source evaporation can be considered as single step deposition: an inorganic component ($PbCl_2$) and the organic source (MAI) are evaporated simultaneously from separate sources at 10^{-5} mbar followed by annealing. The resulting $CH_3NH_3PbI_{3-x}Cl_x$ films are uniform and by incorporating them in planar solar cells, show PCE of over 15%. However, this is not an easily scalable method [94].

1.7.2 Double-Step (DS) deposition

In the DS deposition (or sequential deposition) method, there are three possible routes: (1) Spin coating: lead halide (Cl^-, Br^-, I^-) film is spin coated on the substrate followed by spin coating of MAI [95], (2) Dipping: the lead coated substrate is immersed into MAI solution for complete conversion of the perovskite [46] [96] or (3) Vapour assisted deposition: MAI is vapour deposited onto the lead coated substrates [97]. As compared to SS approach, DS perovskite deposition method has better control over the perovskite morphology and higher reproducibility than standard SS method, as well as better pore-filling, resulted in more conformal capping layer [98] [99]. However, even though DS has already been demonstrated on large area via scalable slot-die coating and roll-to-roll production [100]. But, it presents some limitations such as additional process steps, and comparatively higher processing cost than SS.

Further optimization has led to efficiencies beyond 20%, by introducing a lead halide capping layer onto the mesoporous TiO_2 scaffold that enables complete infiltration of the mixed cation solution, resulting in quick and full conversion of $FA_{1-x}MA_xPb(I_{1-x}Br_x)_3$ films [101]. The immersion in MAI solution can be replaced by vacuum assisted vapour deposition in the presence of solid MAI or by MAI spin coating, followed by annealing in the presence of DMF vapour [102]. An interesting and effective DS approach is the intermolecular exchange process (IEP) in which a mediator, such as DMSO, acts as both reactant and solvent for PbI_2 to avoid rapid and uncontrolled self-assembly crystallization between FAI or MAI and PbI_2. By spin coating FAI solution on the top of DMSO-intercalated-PbI_2 films, a direct molecular exchange of DMSO with FAI molecules occurs, producing large-grained $FAPbI_3$ films without any residue of PbI_2 with PCE greater than 20%. [50].

By using DS approach, the best performing TiO_2 nanostructured (NRs & NTs) based PSCs exhibit PCE 14 – 16% that is lower than a mesoporous nanoparticle or compact flat rival, primarily due to associated pore-filling issues and a poor physical connection between the interface of perovskite and ETL.

1.7.3 Methylamine Gas Induced Defect Healing (MIDH)

In 2015, Zhou et al. explained the influence of Methylamine (MA) gas on $CH_3NH_3PbI_3$ and found that under short exposure of MA gas, the perovskite ($MAPbI_3$) crystals collapse into liquid phase (colourless). The crystallization of perovskite starts again with dark brown colour after removing MA gas. **Fig 1.10** shows the whole MIDH process [103]. It is believed that the interaction between $MAPbI_3$ and MA is likely that Methylamine (CH_3NH_2) molecules react with PbI_6-octahedral frame work and disrupt PbI bonding that results into the collapse of crystal structure and forming a liquid phase (equation 1.4). Upon degassing, Methylamine molecules are released from the liquid (equation 1.5), resulting in recrystallization of $MAPbI_3$ structure [104].

$$CH_3NH_3PbI_2\,(s) + xCH_3NH_2\,(g) \rightarrow CH_3NH_3PbI_2 \,.\, xCH_3NH_2\,(l) \tag{1.4}$$

$$CH_3NH_3PbI_2 \,.\, xCH_3NH_2\,(l) \rightarrow CH_3NH_3PbI_2\,(s) + xCH_3NH_2\,(g) \tag{1.5}$$

Figure 1.10: Evolution of two perovskite crystals under methylamine gas atmosphere [103].

In order to get further insight of gas-perovskite interaction, Zhou et al. [103] studied the effect of different types of amine gas. When ammonium (NH_3) gas interacts with perovskite crystals, a photo-bleaching phenomenon occurs but there is an incomplete solid-to-liquid conversion. This incomplete conversion could be due to less basicity and smaller molecules of NH_3 gas rather than CH_3NH_3 gas. Thus, a minor change in perovskite surface morphology occurs after reversible interaction with NH_3 gas. When large molecules of amine gases such as ethylamine and n-butyl amine interacted with perovskite, a complete conversion of solid-to-liquid phase occurred. However, a complete back conversion into dark brown perovskite did not occur after degassing. For any alkyl group (R) other than Methyl (CH_3), the interaction of gas-perovskite results into an irreversible formation of stable non-perovskite phase. Therefore, above results show the importance of the selection of MA gas for MIDH process.

Fig 1.11 shows a schematic illustration of the basic mechanism involved in MIDH process of perovskite. Exposure to MA gas results in the uptake of MA molecules by pristine perovskite film accompanied by volume expansion. Afterwards, collapse of the perovskite crystals and solid-to-liquid conversion occurs. This process happens in a short time as perovskite have nanoscale crystals in the form of thin film. This liquid spreads all over the surface and forms an ultra-smooth substrate surface. If the substrate has mesoporous layer then this liquid is likely to infiltrate into the pores of mesoscopic structure. Upon degassing, the liquid releases the MA molecules rapidly that results into volume contraction, reconstruction of dense, and an ultra-smooth perovskite crystal structure.

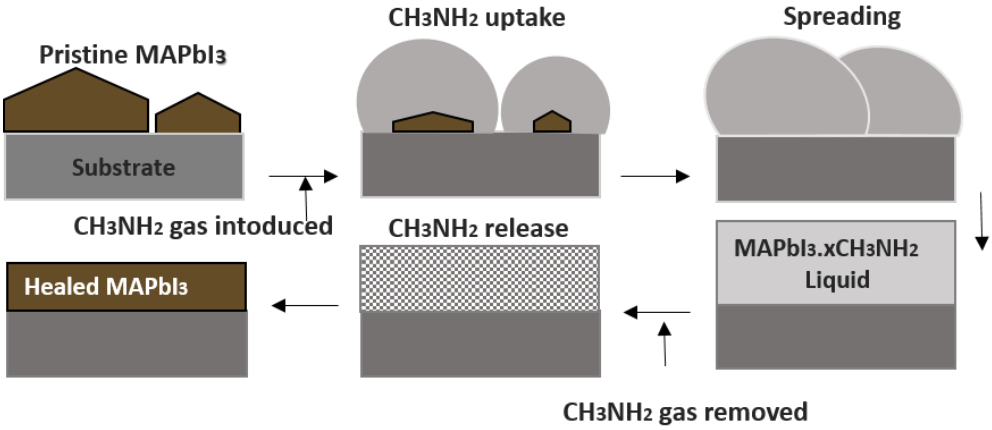

Figure 1.11: Schematic illustration of basic mechanism involved in MIDH process of perovskite.

1.8 Role of selective contacts

Available evidences propose that charge separation and transport in PSCs occur within the perovskite layer, perovskite-ETL and perovskite-HTL interfaces. Therefore, role of selective contacts is crucial for stability, interfacial recombination and hence PCE [105]. There are various selective contacts such as metal oxides (p-type or n-type), organic, inorganic, zero-dimensional, one dimensional and three-dimensional. Their selection determines the photovoltaic parameters (photocurrent and photo-voltage) because of change in band energies and the conductivity/mobility of the selective contacts [49]. The charge carrier diffusion lengths in chloride based perovskites are over ~1 µm [34] with orders of magnitude higher electron mobility than materials used for ETM and HTM that makes the charge recombination significant at the interfaces. This puts rigorous conditions, especially on ETM, to be a material of high charge mobility and free of defects. TiO_2 nanoparticles have inferior electron mobility but this issue could be resolved by using 1D nanostructures such as nanorods (NRs), nanowires (NWs), nanotubes (NTs) having charge mobility two orders of magnitude higher than nanoparticles. Similarly the hole mobility of HTM has a significant impact on the PV parameters [49]. For example, small molecules based organic hole transporting material such as doped Spiro-OMeTAD has higher conductivity and hole mobility as compared to conducting polymer based hole transporting material like P_3HT [106].

Besides PCE, the choice of these selective contacts has also been shown to influence the operational stability. For example, ETL such as TiO_2 nanorod based encapsulated PSCs have shown a stability of >2000 h when compared to nanoparticle rival at similar test conditions, probably due to high crystallinity and thermodynamic stability of the former [107], and for HTMs, in general inorganic HTMs and HTM free devices show superior stability as compared to their organic counterparts [106] .

1.9 Research objectives

It is apparent that the performance and operational stability in the PSCs is significantly influenced by the morphology (grain size, type of grain boundaries, film coverage etc.) and the characteristics of the interfacial layer (organic vs inorganic, conductivity, surface defects and energetics). Our research is mainly focused on engineering and improving the morphology of the perovskite layer developed via most common deposition methods and the properties and optimization of the selective contacts. The key objectives of the study are:

- To improve the perovskite films morphology via incorporation of additives or anti-solvent treatment.
- To improve the perovskite pore-filling in one-dimensional nanostructure scaffolds via Methylamine gas healing.
- To investigate the role of various electron transport layers (compact versus nanostructured) on the photovoltaic performance and stability of the perovskite solar cells.

1.10 Thesis outline

The research work is mainly focused on material synthesis, device fabrication and employing different material and device characterization techniques to evaluate the photovoltaic performance of the perovskite solar cells. The structure of the thesis is based on published and submitted journal articles. The first part (Chapter I) presents an overview of photovoltaics along with a detailed description of the properties of perovskite material, device architectures and working mechanism of the perovskite solar cell. Morphology engineering of the perovskite film via various deposition routes and the role of selective contacts is comprehensively reviewed in this chapter.

The second part (Chapter II & III) summarizes the research work and accomplishments, that is, materials synthesis, device fabrications, extensive characterizations, detailed analysis and structure optimizations.

The last part (Chapter IV) presents the summary and conclusion of the research work. Some future ideas that can be explored to further enhance the performance of the perovskite solar cell are also described. The published and submitted articles are attached at the end of thesis.

Chapter 2

Chapter 2 presents the improvements achieved on perovskite layer morphology by using additives and anti-solvent treatment. The effects of these improvements on the perovskite solar cell performance is thoroughly evaluated.

We note that the performance of the devices was not comparable to the state-of-the-art devices. However, the optimization of the devices to achieve high efficiency was not the main goal. Our results clearly indicate a positive change in the energy levels of anti-solvent treated perovskite film. Moreover, anti-solvent treated method works better with SS rather than DS perovskite deposition method.

The work presented in this chapter has been published in:

1- Asmat Nawaz et al. Morphology Study of Inverted Planar Heterojunction Perovskite Solar Cells in Sequential Deposition, International Journal of Electrical, Computer, Energetic, Electronic and Communication Engineering, Vol:10, No:7, 2016
2- Asmat Nawaz et al. Insights into optoelectronic properties of anti-solvent treated perovskite films, J Mater Sci: Mater Electron, pp. 1-7, 2017.

2 Morphology engineering of perovskite (via additive and anti-solvent treatment) of inverted and regular planar PSCs.

2.1 Summary and context

Organic-inorganic halide perovskites have recently shown tremendous research interest due to their ground breaking photovoltaic performance mainly stemmed from the modification in the perovskite precursor composition and morphology. It has been suggested that low performance in planar device architectures may arise due to pinhole formation and incomplete surface coverage of the perovskite that results in low-resistance shunting paths and lost light absorption in the solar cell [57].

In this research work, both inverted and regular planar devices are fabricated. Two methods, that is: anti-solvent treatment and solvent additives are employed for optimization of the perovskite morphology. It is demonstrated that higher photocurrent values are achieved only with the highest perovskite surface coverage. From photoelectron spectroscopy (PESA) measurement, it is shown that anti-solvent treated perovskite film has deeper VBM with respect to HTM (in this PEDOT:PSS) that favours higher V_{OC}. With this shift in the energy levels, higher V_{OC} ~ 1.08V is obtained as compared to 0.61V for non-treated perovskite film. It is also found that anti-solvent treatment works better with single-step than double-step perovskite deposition method.

2.2 Materials and methods

2.2.1 Synthesis of MAI:

Methylamine (20ml, 40 wt% in ethanol, Aldrich) and Hydroiodic acid (30ml, 57 wt% in water, Aldrich) were mixed in a round bottom flask and stirred at 0℃ for 2 h. The precipitates were recovered by solvent evaporation through rotary evaporator at 60℃ for 30 min. The product was rinsed with diethyl ether (Aldrich) until the color of precipitates changed from pale yellow to colorless and then recrystallized in ethanol. Finally, after filtration, MAI crystals were dried in a vacuum oven at 60℃ for 24 h.

2.2.2 Perovskite ($MAPbI_3$) preparation

For single-step perovskite deposition method, $MAPbI_3$ solution was prepared by mixing of PbI_2 (Aldrich) &MAI (0.6:1) in GBL (Aldrich) and stirred for 30 min at 60℃ to get a homogeneous solution. For double-step perovskite deposition method, 1M PbI_2 solution was prepared in DMF (Aldrich) and kept at 90℃ to get homogeneous solution, and 65mg/ml MAI (Dynemo) solution was prepared in Isopropyl alcohol (IPA-Aldrich) at room temperature.

2.2.3 Interface layer

Phenyl-C61-butyric acid methyl ester (PCBM-Aldrich) and c-TiO_2 NPs (Solaronix) were used as ETL, Poly(3,4-ethylenedioxythiophene)-poly(styrenesulfonate)-(PEDOT:PSS-Heraeus) and Poly(3-hexylthiophene-2,5-diyl)- (P_3HT-Aldrich) were used as HTL. PEDOT:PSS and PCBM were used for inverted device structure and c-TiO_2 NPs and P3HT were used for regular device structure.

2.2.4 Fabrication of PSC

(a) Inverted device architecture

2.5x2.5 cm^2 ITO coated substrates (Solaronix) were patterned by etching with 2 molar HCl solution and ultrasonically washed by acetone (Aldrich), DI-H_2O and IPA respectively. After drying with nitrogen, substrates were treated with oxygen plasma for 10 min. PEDOT:PSS (35µl) was spin coated at 2800rpm for 35s and annealed at 120℃ for 20 min. The perovskite (30µl) was spin coated on PEDOT:PSS coated substrates at 3000rpm for 30s and in second step, 20µl Toluene (TL) was dropped on spinning substrates (5000rpm) 10-15s before completion [76] and annealed at 80 ℃ /110℃ for 20 min. PCBM (30µl) solution was spin coated at 2500rpm for 40s and annealed at 80℃ for 15min. Finally, 100nm of Al was thermally evaporated as a back contact. An embedded thermal evaporator (MBraun) inside the glove box was used for Al evaporation. (Almost 1 hour to achieve pressure $< 8x10^{-6}$mbar and approximately 45 minutes for Al evaporation). The same inverted device architecture was fabricated via sequential deposition method. PEDOT:PSS was spin coated at 2800rpm for 30s on the etched, clean and oxygen plasma treated ITO substrates and annealed at 120℃ for 20 min. 0.8M PbI_2/DMF solutions with additive DI-H_2O (0wt%, 1wt%, 2wt%, 3wt%) were prepared and stirred at 80℃ for 30min . Firstly, PbI_2/DMF (1 wt% DI-H_2O) was spin coated on PEDOT:PSS coated substrates at different rotation speeds (3000-6000 rpm) for 25s and immediately immersed into MAI/IPA solution for 2-3 min to form perovskite. The perovskite films were rinsed with IPA to extract extra iodide and annealed at 110℃ for 1-2 min. PCBM solution was spin coated at 1500rpm for 35s and annealed at 80℃ for 15 min. Finally, 100nm of Al was evaporated as the back contact.

(b) Regular device architecture

The regular devices via DS perovskite deposition method were fabricated on ITO substrates (1.4x1.4cm^2) [108]. In brief, a preheated 50µl PbI_2 solution was spin coated on c- TiO_2 at 5000rpm for 15s inside the glove box and annealed at 70℃ for 1 h. Once cooled down to room temperature, the substrates were drop casted with MAI/IPA (100µl) for 40s (loading time), spun at 4000rpm for 20s and annealed at 110℃ for 15min. P3HT-20mg/ml (45µl), prepared in CB was spin coated on the perovskite layer at 2000rpm for 60s in the glove box. Devices were kept in high vacuum chamber (~ 10^{-6}mbar) for thermal evaporation of WO_3-Ag back contact (3-100nm thickness) [109]. The active area of all fabricated devices was 0.13cm^2.

2.3 Results and discussion

2.3.1 Additives

Additives play an important role to enhance the solubility of the solution, resulting into uniform, smooth and dense surface morphology [110]. In this research work, perovskite sequential deposition method is used to fabricate inverted device architecture. The perovskite morphology is manipulated through DI-H_2O. 0.8M PbI_2 solution in DMF has less solubility even after heating at 80℃ for 30 min. However, a controlled amount of DI-H_2O (1 wt%) makes solution homogenous as shown in **figure 2.1**.

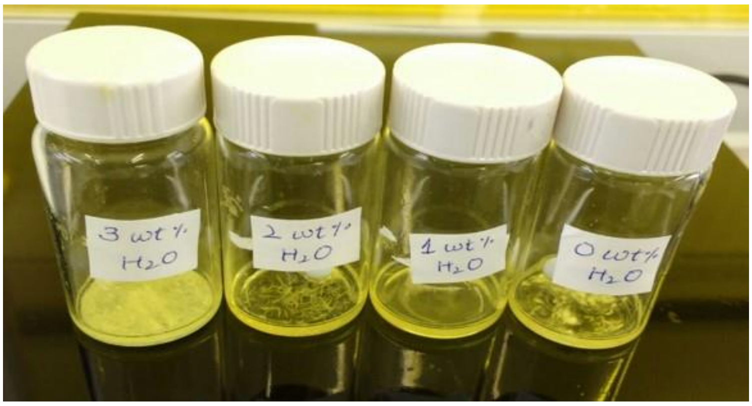

Figure 2.1: Photograph of PbI_2/DMF solution having different amount of water

H_2O is miscible with DMF. The solubility, dielectric constant and polarity parameters are altered after adding water. PbI_2 is dissolved sparingly in water and the solubility parameter of H_2O/DMF solution may be close to PbI_2, therefore, PbI_2 is completely dissolved in the solution [87]. **Figure 2.2 (a-d)** shows the optical images of PbI_2/DMF films with different wt% of water deposited on PEDOT:PSS coated substrates by spin coating. There is a large impact of the water content on the PbI_2 morphology. A continuous and smooth morphology is observed with 1 wt% H_2O and a worse morphology is observed with higher or lesser water content. The increased surface coverage of PbI_2 film suggests that water can induce homogeneous nucleation by modifying PEDOT:PSS/PbI_2 interfacial energy. Furthermore, PEDOT:PSS is hydrophilic and a controlled amount of water in PbI_2/DMF has good adhesion with that. This leads to an improvement in the surface coverage after spin coating. **Figure 2.2 (e-h)** shows the optical images of the perovskite films. The morphology transition from needle like structure to hexagonal plate and again needle like structure is observed by continuous adding of water. As expected, perovskite morphology is highly dependent on PbI_2 films. Therefore, perovskite film with 1 wt % H_2O has better surface coverage.

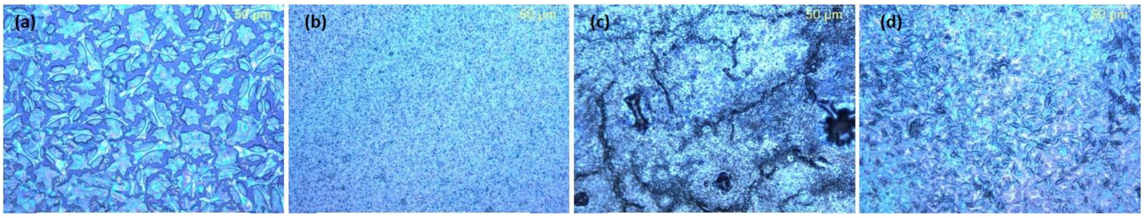

PbI_2 (wo DI-H_2O) PbI_2 (1wt% H_2O) PbI_2 (2wt% H_2O) PbI_2 (3wt% H_2O)

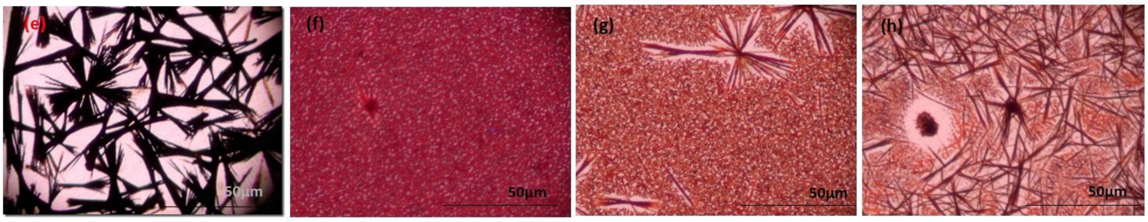

Perovskite (wo H_2O) Perovskite (1wt% H_2O) Perovskite (2wt% H_2O) Perovskite (3wt% H_2O)

Figure 2.2: Optical images of PbI_2 films (a-d) and perovskite films (e-h) prepared from various amount of H_2O in PbI_2/DMF solution.

Perovskite film (1wt % H_2O) thickness dependent photovoltaic measurements are carried out and summarized in table 1. Profilometer (DEKTAK 150) is used to measure perovskite film thickness, as it is a key variable in the device performance particularly in planar heterojunction solar cells. The charge carrier diffusion length for triiodide ($MAPbI_3$) perovskite has been reported ~100nm. Liu et al. has shown planar devices composed of both thinnest $\leq$ 100nm and thickest $\geq$ 400nm $MAPbI_3$ films having PCE of 1-3% [111]. It is shown in the **table 2.1** that with the increase of the perovskite film thickness, there is a decrease in the PCE due to a significant increase in the recombination of the charge carriers at the center of film before reaching to the respective electrodes.

Table 2.1: Summary of PV parameters of PSCs w.r.t perovskite film thickness at 1 sun.

Devices	Perovskite thickness (nm)	V_{OC} (V)	J_{SC}(mAcm^{-2})	FF	PCE%
1	450	0.74	9.43	0.382	2.66
2	550	0.72	6.09	0.334	1.46
3	600	0.68	5.60	0.318	1.21
4	650	0.48	5.44	0.279	0.73

2.3.2 Anti-solvent treatment

Recent studies [58] [76] [82] [112] have shown that anti-solvent treatment is one of the most effective way to induce crystallization and improved perovskite morphology. It can be accomplished by using a non-dissolving solvent such as dichloromethane (DCM), chloroform [76] , chlorobenzene [113] and toluene [58]. These solvents have high miscibility with host solvent and poor solubility with the perovskite precursors. This simple method consist of spin coating of the perovskite precursor followed by subsequent spin coating of organic solvent on to the wet perovskite film to induce crystallization. At the initial stage of spinning, film is composed of MAI and PbI_2 in GBL/DMF, while during the intermediate phase, film is concentrated due to some evaporation of DMF/GBL. Then droplets of TL lead to quick-freezing (drying) of the constituents on spinning through rapid removal of the excess amount of DMF/GBL and an intermediate state PbI_2-MAI-GBL/DMF is formed, which consist of uniform and light brown colour.

After annealing, intermediate phase of the perovskite film is completely converted into crystalline perovskite with dark brown colour. [45] [76].

A detailed comparison on the optoelectronic properties of pristine and TL washed $MAPbI_3$ films via SS (inverted device architecture) and DS (regular device architecture) perovskite deposition method is provided. **Figure 2.3 (a-f)** illustrates top and cross views of pristine and TL treated perovskite films. The pristine perovskite film shows inhomogeneous and island like morphology with thickness 250±20nm, while TL treated perovskite film shows uniform and smooth morphology with thickness 90±30nm. To evaluate the crystallographic properties of both perovskite films (with and without TL) as a function of temperature, XRD measurement is carried out as shown in **figure 2.3 (g and h)**. XRD pattern of both perovskite films annealed at 80℃ for 20 min without TL (blue) and with TL (red) is shown in **figure 2g**. We observed all characteristics peaks of the perovskite at $2\theta=14.2^{\circ}$(110), 28.45˚ (220) and 45.15 ˚ (330) [114]. However, both films still demonstrate peaks at $2\theta=12.5^{\circ}$ and 25.58˚, which corresponding to PbI_2, indicates an incomplete transformation of the perovskite [46]. When both perovskite films are annealed at 110℃ for 20 min, representative PbI_2 peaks disappeared **(fig 2.3h)**. Higher annealing temperature also indicate higher peak intensity, even higher after TL treatment, indicating a systematic trend for enhancement in the crystallinity. The higher crystallinity of TL treated film attributes larger grains that can be seen from cross view of both films as shown in **fig 2.3 (c and f).**

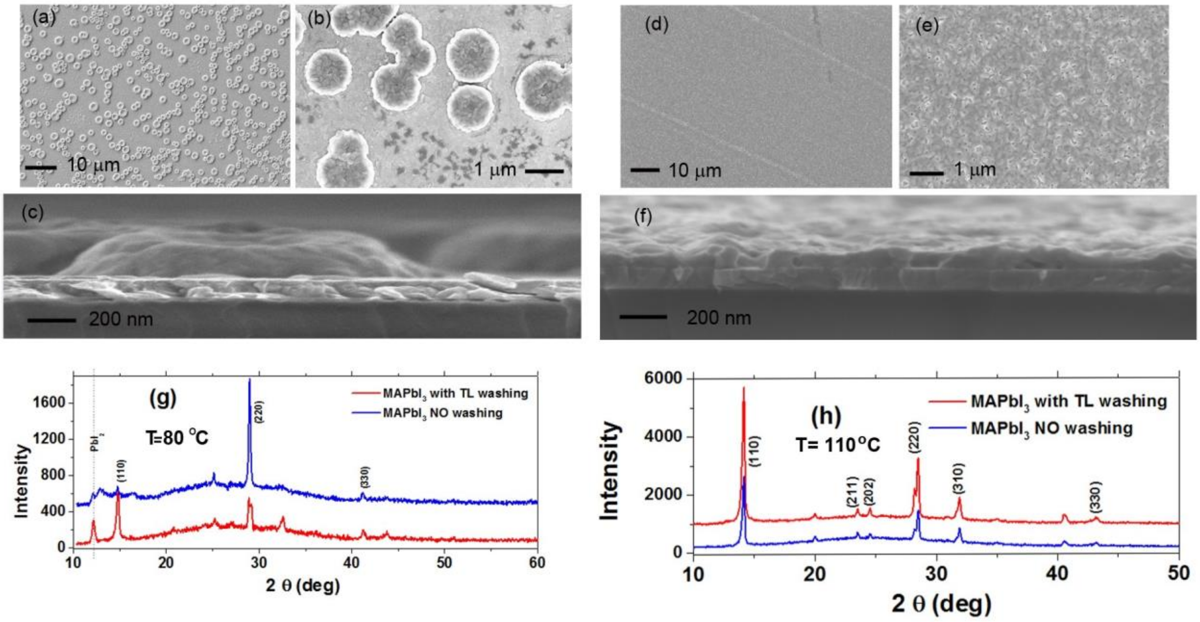

Figure 2.3: SEM images of top and cross view of pristine (a,b,c) and TL treated (d,e,f) perovskite film. XRD pattern of both films as a function of temperature (g and h).

To determine the effect of both perovskite films on the optoelectronic properties, absorbance and photoluminescence (PL) measurements are carried out. **Figure 2.4a** shows the absorbance spectra of both films. The TL drenching enhanced the absorption spectra from 370nm to 660nm because of dramatic change in the perovskite surface coverage that reaches close to 100% [115]. The most significant observation is change in the absorption onset, 762nm for pristine film and 782nm for TL treated film, corresponding to the bandgap of 1.62 and 1.58 eV respectively. The inset of **fig 2.4a** depicts a dark brown colour for TL treated film, indicating a change in the bandgap. A similar trend is observed for PL spectra of both films **(fig 2.4b).** The pristine perovskite film shows the PL emission peak at 1.70 eV that reduced to 1.62 eV for TL treated perovskite film. The higher absorption edge shift of 38 nm for pristine perovskite than TL treated films (17 nm) suggest the presence of more morphological defects in the former. A similar trend can be seen from PL quantum yield **(figure 2.4c).** Upon TL drenching, there is a remarkable increase in the PL intensity. We expect the PL is influenced by defects in the perovskite film. A better film quality (TL treated) has lesser defects, which eliminates sub-band trap states (non-radiative recombination centres), while in the pristine perovskite film, it is dominated by non-radiative recombination centres arising from more morphological defects [116].

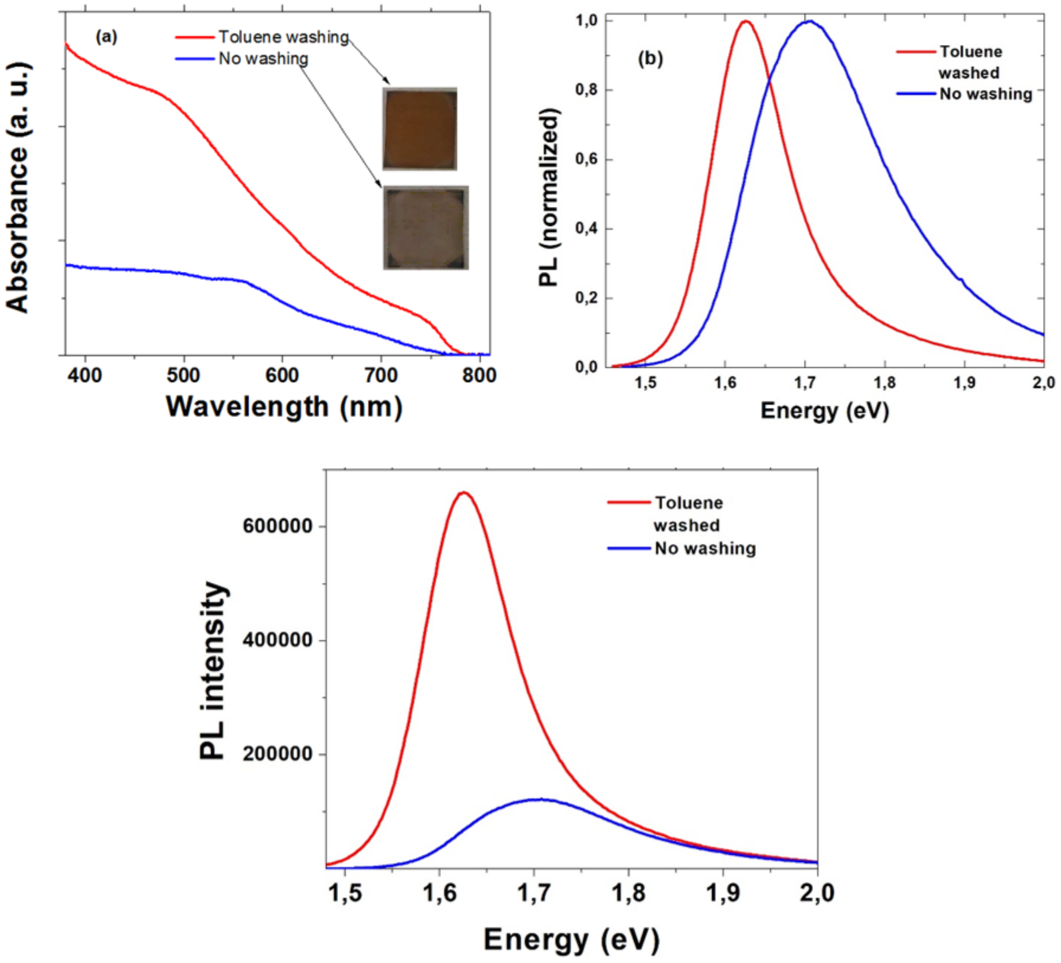

Figure 2.4: (a) Absorbance, (b) Normalized steady state PL spectra of pristine (blue) and TL treated (red) perovskite films and (c) PL quantum yield of pristine (blue) and TL treated (red) perovskite films.

Photoelectron spectroscopy in air (PESA), is carried out to estimate the values of valance band maxima [117] of the perovskite films. The calculated VBM is at -5.22eV and

-5.31eV without and with TL washing respectively as shown in **figure 2.5 (a and b).** We believe that this shift could be a reason for the change in the surface potential of both films due to different surface roughness [118] [119] or because the perovskite films are slightly chemically different. By combining VBM values with the calculated bandgap (E_g) (from the absorbance spectra), we deduced the values of the conduction band minimum (CBM) using the relation CBM = VBM + E_g. The calculated energy levels of both perovskite films are shown in **fig 2.5c**. The band-edge positions of PEDOT:PSS [120] , HOMO/LUMO level of PCBM [121] and work functions of ITO and Al [120] are taken from the literature. The TL treated perovskite film shows a deeper VBM as compared to PEDOT:PSS and a closer CBM to PCBM than pristine perovskite counterpart. A deeper VBM favors higher V_{OC} as shown in the literature [49] and therefore, a high value of V_{OC} upon TL treatment is expected. Contrarily, pristine $MAPbI_3$ film shows less deeper VBM and higher CBM that leads to potential loss at both (ETL-$MAPbI_3$ and HTL-$MAPbI_3$) interfaces.

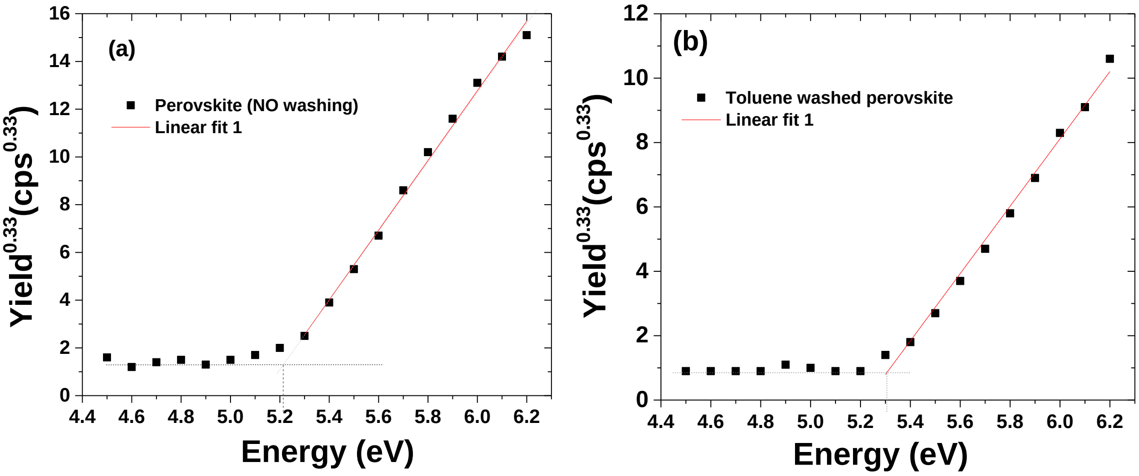

Figure 2.5: (a) PESA measurement of (a) pristine and (b) TL treated perovskite film

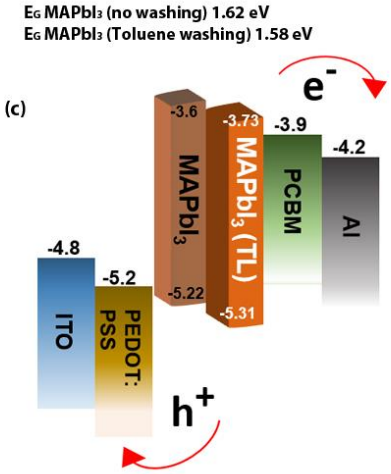

Figure 2.5: (c) Schematic illustration of energy levels of various device layer components.

To validate an improvement in the charge transfer, J-V measurements are carried out for both devices at 1 sun condition. The TL treated device demonstrates J_{SC} = ~ 12mA/cm^2, V_{OC} = 1.08 V, FF 0.63 and PCE 8.12% significant higher than non-treated device. **Table 2.2** shows the PV measured parameters of both devices. Higher J_{SC} shows an improvement in the charge collection and higher V_{OC} suggests a reduced interfacial recombination.

Table 2.2: Summary of measured photovoltaic parameters of PSCs at 1sun.

Device	J_{SC} (mA/cm^2)	V_{OC} (V)	FF	PCE (%)
Wo TL	6.77	0.61	0.31	1.28
With TL	11.97	1.08	0.63	8.12

The effect of TL on the perovskite films prepared via DS deposition is also investigated. Four different types of perovskite films are prepared, that is: no washing, PbI_2 wash, MAI wash and both (PbI_2 and MAI) wash, as shown in **figure 2.6.** However, no significant difference in the perovskite films is found because it has already a good film morphology. Therefore, it is found that anti-solvent treatment seems to work better with SS, where the perovskite film has significant morphological defects without anti-solvent treatment.

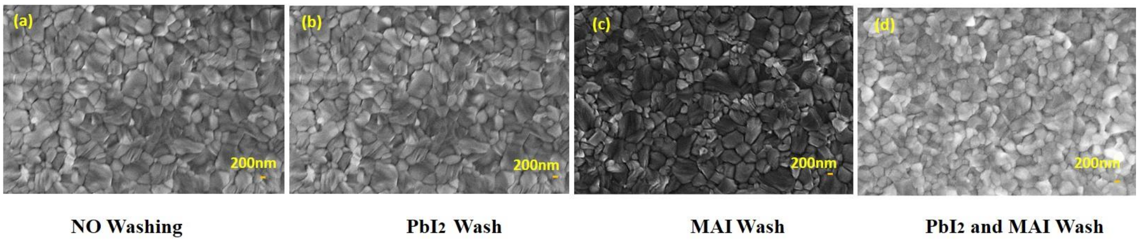

Figure 2.6: SEM images of the top view of perovskite morphology on FTO at various stages as illustrated in figure legend.

The J-V measurements are also carried out for all types of perovskite films as shown in **fig 2.6**. There is no significant difference in the device performance. A lower J_{SC} is noteworthy in dually washed film, because of each washing cycle reduces the film thickness as it is already shown in **figure 2.3** for SS perovskite deposition.

Table 2.3: Summary of PV parameters of PSCs at light intensity of 85mA/cm^2.

Device	**J_{SC} (mA/cm^2)**	**V_{OC} (V)**	**FF (%)**	**PCE (%)**	**Scan Direction**
Wo TL	5.35 5.77	0.66 0.67	32.06 37.19	1.33 1.69	F R
PbI_2 wash	4.82 5.72	0.68 0.75	28.28 37.56	1.09 1.89	F R
MAI wash	6.24 8.45	0.65 0.77	25.36 39.44	1.21 3.02	F R
PbI_2&MAI wash	4.01 4.45	0.69 0.72	28.54 36.69	0.93 1.38	F R

Chapter 3

Chapter 3 presents the improvements in the pore filling of nanostructures via Methylamine gas. We also investigated the role of electron transport layers on the photovoltaic performance and operational stability of the devices.

We note lower performance in our devices compared to the state-of-the-art for TiO_2 scaffolds. However, optimization of the devices to achieve high efficiency was not the main goal of this study. Our experiments clearly show the advantages of improving the pore-filling in order to improve the performance and stability of the cell.

The work presented in this chapter has been submitted in:

Asmat Nawaz et al. Improved pore-filling of TiO_2 nanorods and nanotubes scaffolds for perovskite solar cells, submitted to ACS Applied materials & Interfaces.

3 Development of PSCs with improved pore-filling of TiO_2 nanorods and TiO_2 nanotubes

3.1 Summary and context

Available evidences propose that charge separation and transport in PSCs occur within the perovskite layer, perovskite-ETL and perovskite-HTL interfaces. The charge diffusion lengths in chloride based perovskites are over ~1 µm [34] with orders of magnitude higher electron mobility than materials used for the ETM and the HTM, that makes the charge recombination significant at the interfaces. This puts rigorous conditions, especially on the ETM, to be a material of higher charge mobility and free of defects. TiO_2 nano-particles have inferior electron mobility but this issue could be resolved by using 1D nanostructures. Similarly the hole mobility of HTM has a significant impact on the PV parameters [49].

1D nanostructures of TiO_2 have shown superior charge extraction efficiency and a higher operational stability as well [107]. However, the performance of TiO_2 nanorods (NRs) and nanotubes (NTs) based PSCs is rather low, mainly, due to associated pore-filling issues and a poor physical interconnection between perovskite/ETL. We investigated this aspect and introduced a method to improve the pore-filling of peorvskite in 1D nanostructures. The already crystallized perovskite layer upon TiO_2 NRs and NTs is exposed to a Methylamine (MA) gas rich chamber (so-called healing process) [103] [104] leading to large $CH_3NH_3PbI_3$ grains and achieved an improved pore-filling. The healed perovskite films demonstrate an improved electron extraction, a longer carrier lifetime for perovskite, and an improved PV performance and stability. Furthermore, doped Spiro-

OMeTAD has higher hole mobility as compared to conducting polymer based HTM like P_3HT. Therefore, nanostructured (NRs/NTs) based devices are also fabricated by using P_3HT as well to validate the effect of low mobility on the PV parameters.

3.2 Materials and methods

3.2.1 Perovskite ($MAPbI_3$) preparation

1M PbI_2 (Aldrich) solution was prepared in DMF and kept at 90℃ to get homogeneous solution, and 65mg/ml MAI (Dynemo) solution was prepared in Isopropyl alcohol (IPA) at room temperature.

3.2.2 Interface layer

TiO_2 NPs (solaronix) and TiO_2 NRs/NTs were used as ETL, Poly(3-hexylthiophene-2,5-diyl)- (P_3HT) and doped Spiro-OMeTAD (Merck) with Li-salt (Aldrich) and tert-butyl pyridine (Aldrich) were used as HTL. TiO_2-NRs (TNRs) and TiO_2-NTs (TNTs) were directly synthesized on FTO by hydrothermal process. A detailed description of hydrothermal process is given below.

(a) Hydrothermal growth of TNRs

Rutile TNRs were synthesized via hydrothermal process [107]. In a typical synthesis, 8ml HCl (37%) and 12ml DI-H_2O were mixed and stirred for 10 min. Then titanium (IV) butoxide (TB) was added into the solution followed by another stirring for 10 minutes to get a transparent solution. The resultant solution was poured into Teflon lined autoclave. FTOs (1.4x1.4cm^2-Solaronix) were immersed vertically in the solution and kept in the oven at 180℃ for various hours to achieve the desired NRs length. The autoclave was cooled down immediately under cold tap water and samples were rinsed with DI-H_2O. Finally, samples were annealed at 450℃ for 30 min under ambient condition.

(b) Hydrothermal etching of TNRs to TNTs

To transform TNRs into TNTs, an etching solution was prepared [122]. In brief, 10ml DI-H_2O was mixed with 14ml HCl (37%) and poured into Teflon lined autoclave. As prepared TNRs were immersed into the solution and kept in the oven at 150℃ for few hours according to the length of NRs . The autoclave was cooled down immediately under cold tap water and samples were rinsed with DI-H_2O. The annealed TNRs and TNTs were modified with $TiCl_4$ (Aldrich) aqueous solution (120mM at 70℃ for 30 min) to improve the surface roughness [123] and to form pinhole free hole- blocking layer. Finally, samples were rinsed with DI-H_2O and annealed at 450℃ for 30 min.

3.2.3 Fabrication of PSCs

A double step perovskite deposition method was employed for the fabrication of the PSCs [108]. In brief, a preheated 50µl PbI_2 solution was spin coated at 5000rpm for 15s on ETL inside the glove box and annealed at 70℃ for 1 h. Once cooled to room temperature, the substrates were drop casted with MAI/IPA (100µl) for 40s (loading time), spun at 4000rpm for 20s and annealed at 110 ℃ for 15min. 45µl Spiro-OMeTAD (HTM) 80mg/ml, prepared in CB followed by an addition of 28.8µl tert-butyl pyridine and 17.5µl Li-salt solution (520mg/ml $LiN(CF_3SO_2)_2N$ solution in acetonitrile) was spin coated at 2000 rpm for 60 s on the perovskite layer in the glove box. The samples were stored in a desiccator in dark overnight to improve the complete oxygen doping of Spiro-OMeTAD. Another HTM-P_3HT-20mg/ml prepared in CB was spin coated at 2000rpm for 60s on the perovskite layer in the glove box. Devices were kept in high vacuum chamber (~ 10^{-6}mbar) for thermal evaporation of WO_3-Ag back contact (3-100nm thickness) [109].

3.2.4 Methylamine Gas Induced Defect Healing (MIDH)

In 2015, Zhou et al. [103] explained the influence of Methylamine (MA) gas on the perovskite ($CH_3NH_3PbI_3$) film. Figure 3.1 shows the schematic setup for MIDH process of the perovskite films. After perovskite deposition, samples were placed below the glass chamber (top of silicon wafer) that was connected to MA gas source, vacuum pump and N_2/Air inlet. A rubber-band was mounted between wafer and glass chamber. In order to avoid corrosion of vacuum pump with MA gas, a filter filled with H_2SO_4 was placed between the vacuum pump and the glass chamber. Before starting the MIDH process, the whole set- up was cleaned with IPA and glass chamber was evacuated followed by MA gas flow for 10 s. Before keeping the samples inside the chamber, a cleaning process (three times) was done by evacuation and N_2 flow to remove MA gas from the connection. After keeping the sample inside the chamber, cleaning process was done again for three times. After that, MA gas valve was opened for ~10 s until dark brown perovskite film became transparent. Afterwards, vacuum pump was opened for 10 s to remove all MA gas from the chamber. Then the whole set-up was placed on the hotplate having temperature 40℃ and the chamber was flushed with N_2 and wait until transparent film recrystallize again into perovskite (dark brown). The rest of the procedure for the fabrication of PSC was done by following the same process as discussed in the fabrication section.

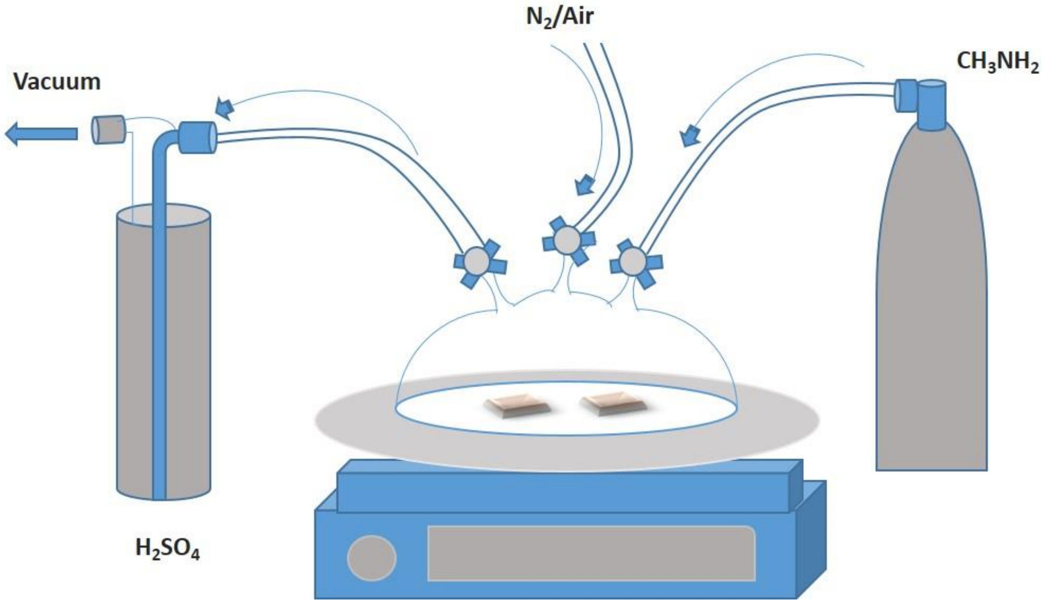

Figure 3.1: Schematic set-up of methylamine gas induced defect healing (MIDH)

3.2.5 Characterizations:

The morphology of the nanostructures and the perovskite films was studied by scanning electron microscope (Zeiss CrossBeam 1540XB FESEM) equipped with an in-lens detector and transmission electron microscope (JEOL). X-Ray diffraction (Bruker D8 Discover with Lynxeye XE detector, Cu Kα 0.15418 nm) was performed to evaluate the crystallographic properties of the nanostructures and the perovskite films. The optoelectronic properties of different perovskites were studied using UV-VIS absorbance (CARY 5000 UV-Vis spectrometer, Agilent) and photoluminescence (PL) spectrophotometer (FluoTime 300, PicoQuant). The time-resolved PL spectra were recorded in vacuum ($5x10^{-5}$ mbar) using time correlated single photon counting (TCSPC) at a repetition rate of 2 MHz. The samples were excited with a 405 nm laser at a repetition rate of 40 MHz. Current-Voltage (J-V) measurements of the PSCs were carried out using a class-A sun simulator in an N_2 environment inert at 81 mW/cm^2, calibrated with a reference Silicon cell and using a Keithley 2420 source meter.

3.3 Results and discussion

The uniform arrays of densely packed and vertically aligned rutile TNRs grown via hydrothermal growth on the conducting substrate (FTO) are shown in **fig 3.2 (a and b)**. A magnified view of NRs **(fig 3.3a)** confirms a tetragonal geometry which is in accordance with past reports [124] [125]. A time dependent (temperature and precursor concentration kept constant) growth of NRs (growth time of 100 to 115 min) yielded the length in the range of 250 to 700 nm. A subsequent etching of the NRs resulted in the NTs **(fig 3.2 c and d)** with approximately same length and diameter. Details on the NRs growth and subsequent etching are shown in **figure 3.4 (i and ii).**

High resolution TEM images of the NRs show a well crystalline lattice with extended crystallinity towards (001) plane **(fig 3.2e)** while the FFT view of a single NR shows the crystalline nature of NR **(inset of fig 3.2f).** The NRs grow along (001) direction with (110) axis, perpendicular to the NRs sidewalls. To improve the surface roughness of the NRs, a post-treatment of the NRs with $TiCl_4$ solution is employed that result in a thin amorphous conformal coating around the NR **(fig 3.2 g and h).** The $TiCl_4$ treatment offers additional benefits to form a pin hole free hole-blocking layer on the FTO/ETL interface. The NTs TEM images **(fig 3.2i)** depict that the surface is defect-enriched, probably because of etching process carried out in the strong acidic medium. The core of the NTs still exhibit high crystallinity **(fig 3.2j)**, however, a TEM investigation at the edge part shows amorphous regions and higher grain boundary density **(fig 3.5)**.

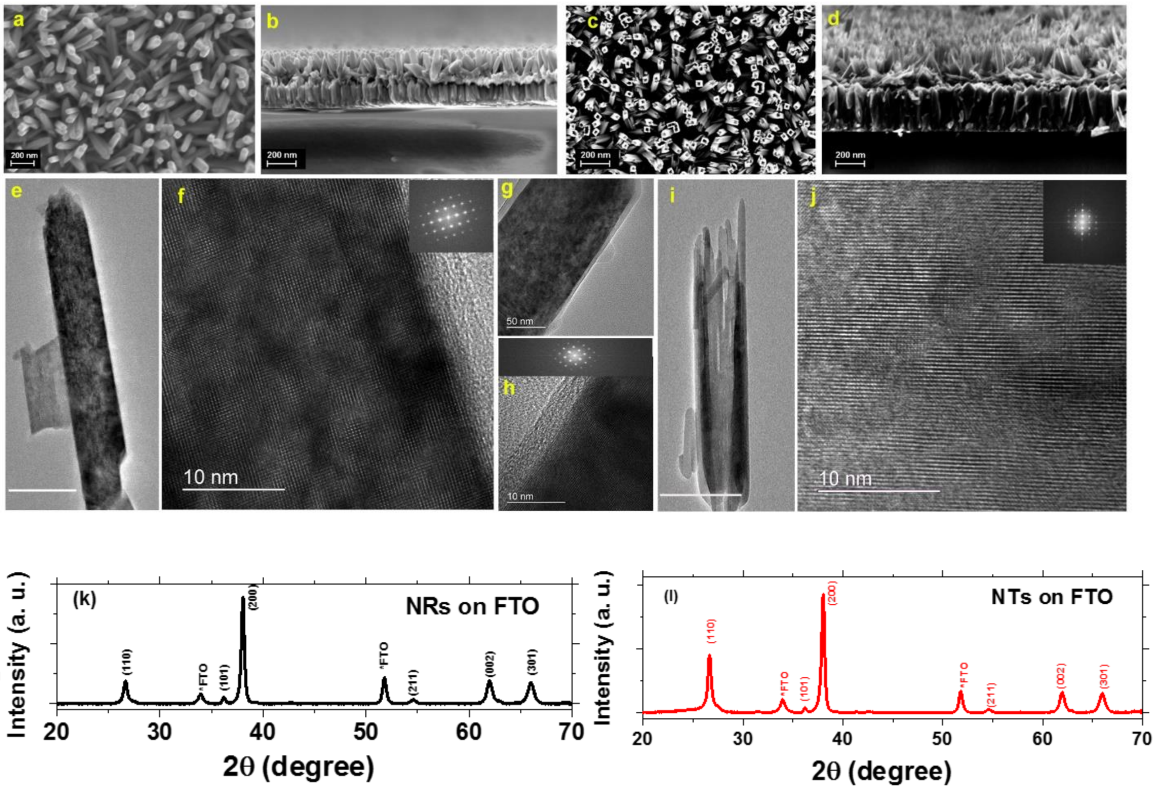

Figure 3.2: Top and cross-view of NRs (a and b) and NTs film (c and d); (e and f) TEM of a single NR, the inset of (f) shows well crystalline electron diffraction pattern, which is mapped locally at the NR surface in (e); (g and h) are TEM images of a NR surface treated with $TiCl_4$ that form a thin amorphous layer around it; (i and j) are TEM images of a typical NT showing a hollow structure and a crystalline morphology. The FFT view in the inset of (j) shows local crystallinity of NT measured at its middle, X-Ray diffraction pattern (k and l) of NRs and NTs respectively.

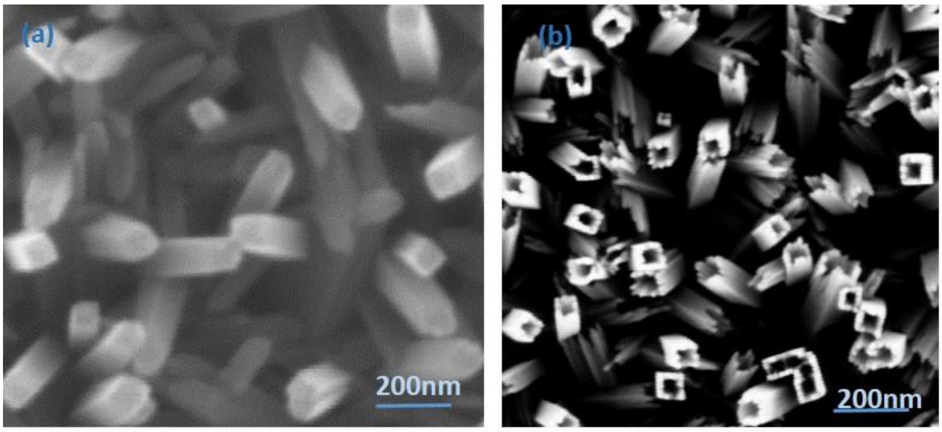

Figure 3.3: SEM images of tetragonal geometry of TiO_2 NRs (a) and TiO_2 NTs (b).

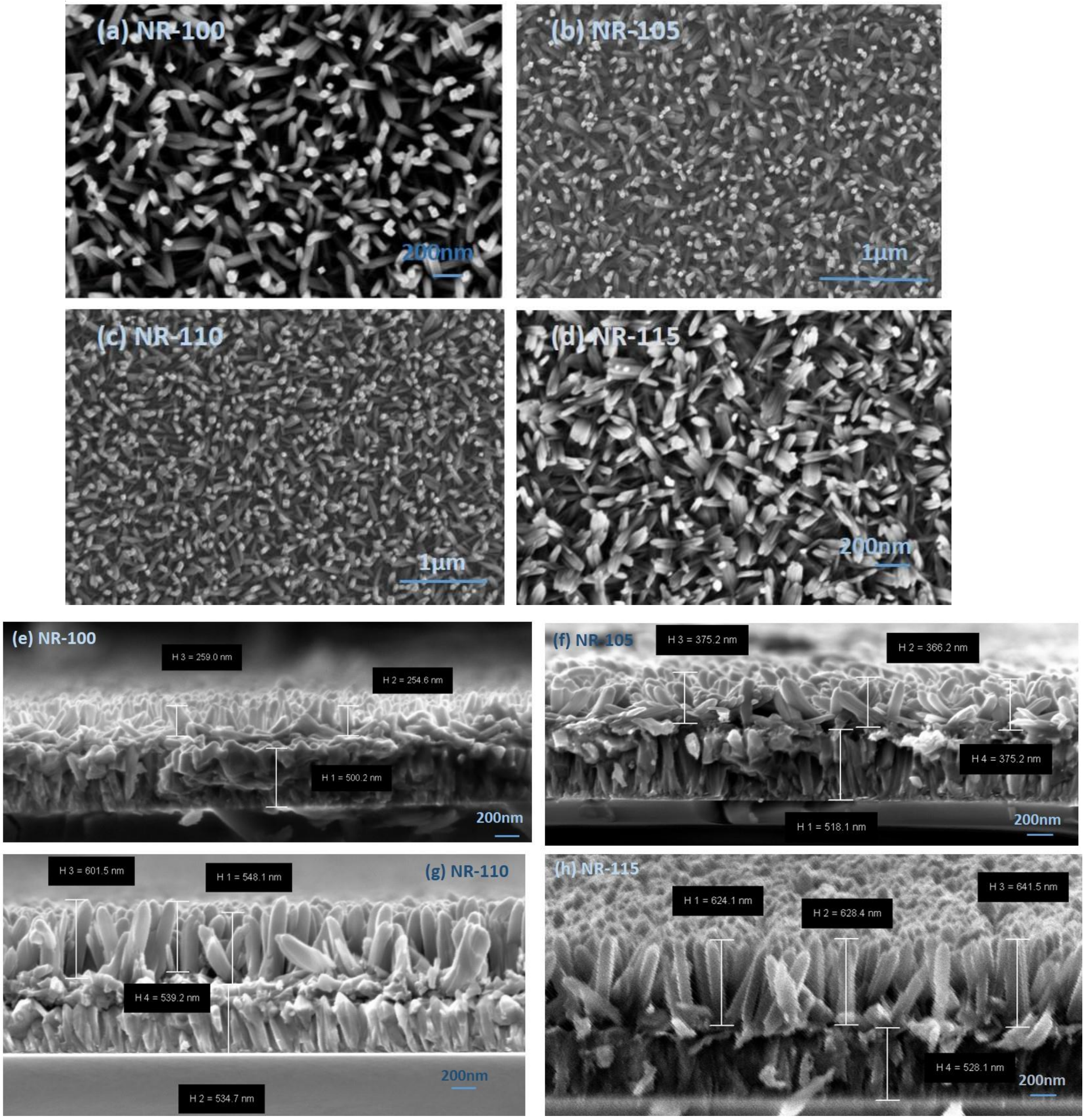

Figure 3.4 (i) : SEM images of hydrothermal growth of TiO_2 NRs; top view (a-d) with different growth timings (100min, 105min, 110min and 115min) along with cross-views (e-h).

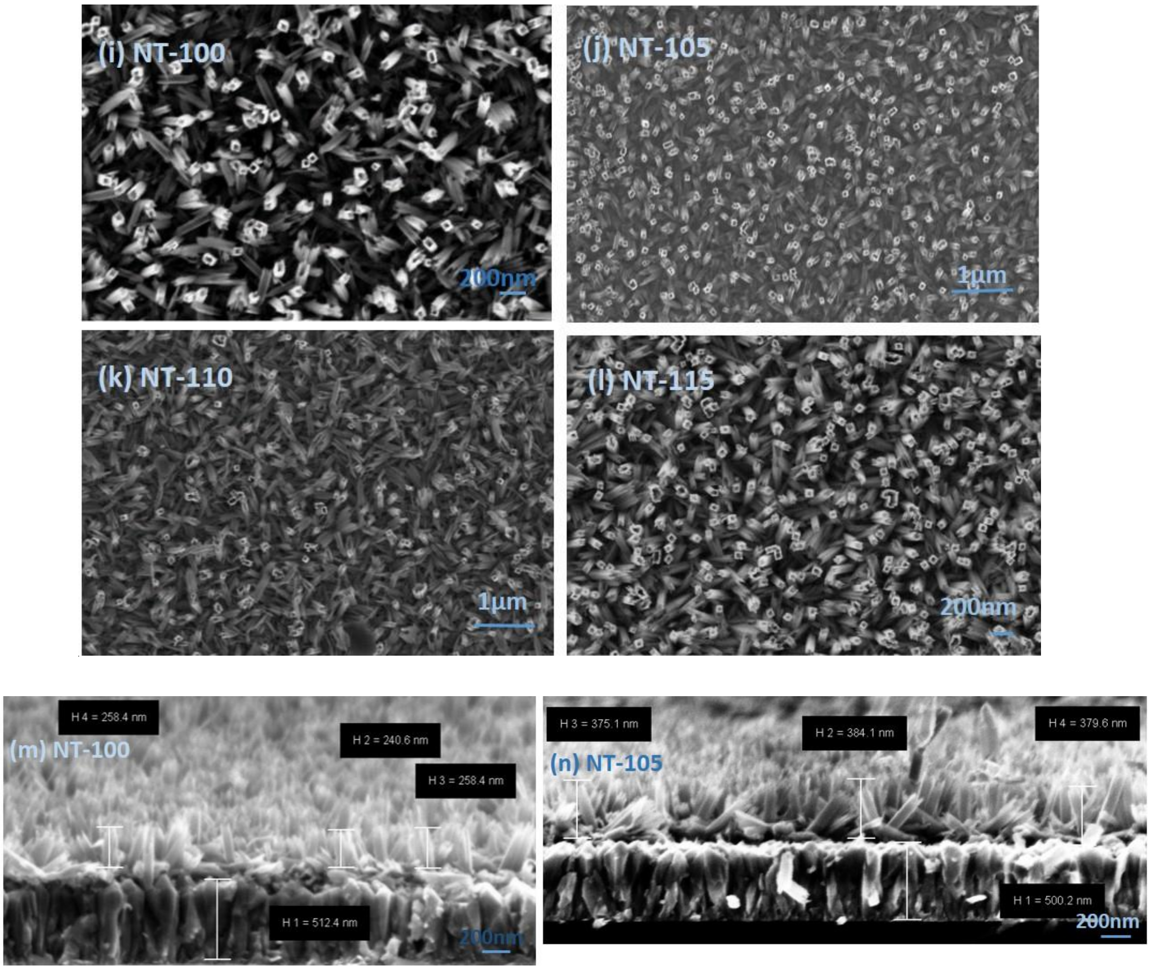

Figure 3.4 (ii) : SEM images of hydrothermal etching of TiO_2 NRs to NTs; top view (i-l) along with cross-view (m and n).

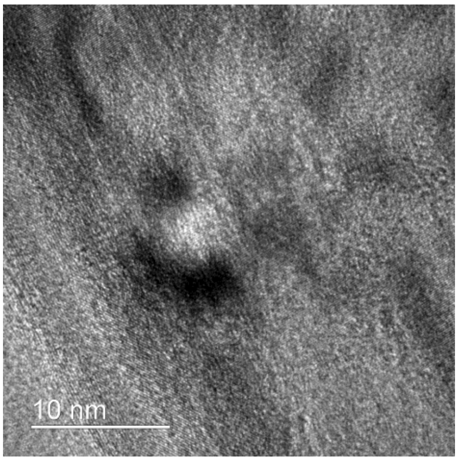

Figure 3.5: TEM image of the edge part of TiO_2 NT

The growth of the NRs and a conversion into NTs can be attributed to the reversible reactions:

$$TiO_2 \underset{\text{dehydration}}{\overset{\text{etching}}{\rightleftarrows}} Ti\ (IV)\ \text{complex} \qquad 3.1$$

Above equation shows reversible reactions with two competing reactions in the system. On one hand, TiO_2 dissolved and produced Ti(IV) complex and on the other hand Ti(IV) complex hydrolysed into TiO_2. During etching (14ml HCl and 10ml DI-H_2O), the solution will push the reaction towards dissolved direction [122]. During the hydrothermal growth of NRs, chloride (Cl^-) ions are known to promote the growth along (001) face, while restricting the growth along (110) direction. As a result, growth rate of NRs along (001) direction is much faster than (110) direction [122] [126]. The surface energy or growth rate of the NRs follows the sequence (110) < (100) < (101) < (001). Usually, the facets of higher surface energies diminish faster to minimize the total surface energy [127]. Therefore, (001) core of NRs etched faster than the (110) face. As a result, solid NRs convert into hollow NTs by keeping the same size and tetragonal shape of NRs **(fig 3.3b)**. Hydrothermal etching time is a critical parameter for a complete conversion of NRs into NTs. If the etching time is below or above a certain time, then no conversion, over-etched and a complete destruction of nanostructure is observed **(fig 3.6)**. Therefore, a precise optimization for the etching time is necessary to get a complete transformation of NRs into NTs.

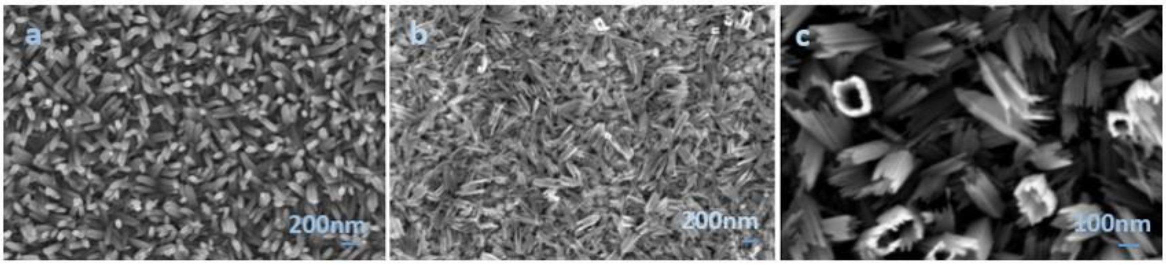

Figure 3.6: SEM images of etching mechanism w.r.t time; (a) No-etching, (b) completely destroyed nanostructure, (c) over-etched NTs

XRD pattern of the NRs and NTs **(fig 3.2 k and l)** shows diffraction peak intensities at (101), (211) and (002) for rutile TiO_2. A stronger intensity at (002) diffraction peak compared to (101) indicates that rutile TNRs are oriented along (001) direction with grown axis perpendicular to the FTO [128]. Both NRs and NTs shows identical peak positions with a minor difference in the peak intensity signifying that etching in the acidic medium does not damage rutile phase of the TiO_2 films [122].

The PSCs fabricated with different NRs and NTs show a systematic dependency on the length. With increasing NR and NT length, the photocurrent (J_{SC}) slightly increases, primarily because of improved light harvesting **(fig 3.7 a and b)**, however, a drop in the V_{OC} – primarily due to a higher recombination led to a lower PCE **(Table 3.1)**. The device fabricated by using pristine TiO_2 NPs showed a lower PCE and comparatively larger hysteresis than a NR and a NT rival, suggesting that an improved charge collection is favored in 1D NR/NTs. A lower PCE is observed for NTs than NRs based PSCs. This can be understood from the fact that the etching process of the NRs generated additional defects in the NT structures (evident from TEM monographs).

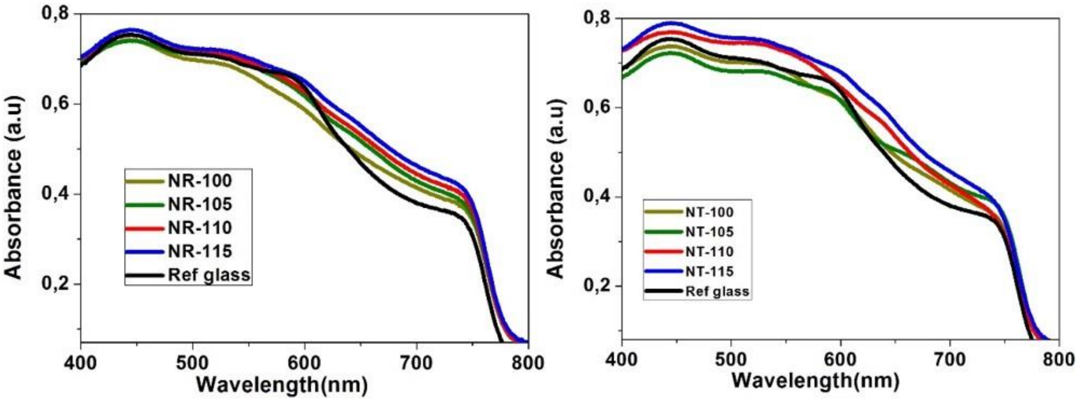

Figure 3.7: Absorbance spectra of the perovskite coated TiO_2 NRs and NTs w.r.t length.

Table 3.1: J-V analysis of PSCs fabricated using different lengths of NRs and NTs and reference device at a light intensity of 81mW/cm^2 (doped Spiro-OMeTAD is used as HTM).

Device	Length of NS (nm)	J_{SC} (mA/cm^2)	V_{OC} (V)	FF	PCE (%)	Scan Direction
NR-100	**250±50**	14.62	0.77	52.62	7.32	F
		14.77	0.88	57.94	9.33	R
NR-105	**350±50**	14.98	0.75	56.29	7.83	F
		14.72	0.82	58.94	8.82	R
NR-110	**550±50**	15.06	0.62	49.09	5.68	F
		15.14	0.74	59.49	8.29	R
NR-115	**650±50**	15.49	0.63	50.67	6.12	F
		15.59	0.75	56.84	8.23	R
NT-100	**250±50**	14.53	0.72	48.38	6.27	F
		14.61	0.85	57.81	8.92	R
NT-105	**350±50**	14.84	0.65	49.33	5.91	F
		14.37	0.79	59.16	8.34	R
NT-110	**550±50**	13.35	0.64	46.79	4.96	F
		13.19	0.78	59.26	7.53	R
NT-115	**650±50**	13.47	0.58	44.62	4.33	F
		13.91	0.73	55.81	7.04	R
Ref. PSC	**100**	7.83	0.65	33.31	2.09	F
		12.32	0.76	58.42	6.68	R

Perovskite morphology of the NRs **(fig 3.8 a and c)** and NTs **(fig 3.8 e and g)** shows a full surface coverage (top-view) with grain size of 100 nm to ~ 1 µm. However, the films also consist of uneven spots that arise due to an uneven 1D nanostructure underneath layer. A cross-view of both films demonstrate a discontinuous film formation with larger cracks suggests a low coverage of perovskite at the bottom of both films **(fig 3.8 c and g)** that leads to higher charge recombination. Furthermore, the cross-views also reveal that the perovskite infiltration is rather poor and the perovskite crystals are mostly formed on the upper part of the NRs/NTs. This is also evident from the full device cross-views **(fig 3.11 a and b)**.

To improve the film morphology and physical interconnectivity, perovskite healing process is carried out in MA gas environment [103] [129]. Under MA gas rich environment, the perovskite film turns completely transparent showing a complete dissolution into the liquid phase and then recrystallize to form large crystals **(fig 3.9** photographs taken during the healing process**)**. The MA healing resulted in large crystals (up to few hundred microns, **(fig 3.8 b and f)** and an improved pore-filling through 1D scaffolds. The cross-views **(fig 3.8 d and h)** evidence the continued large crystal formation and a superior pore-filling in 1D scaffolds.

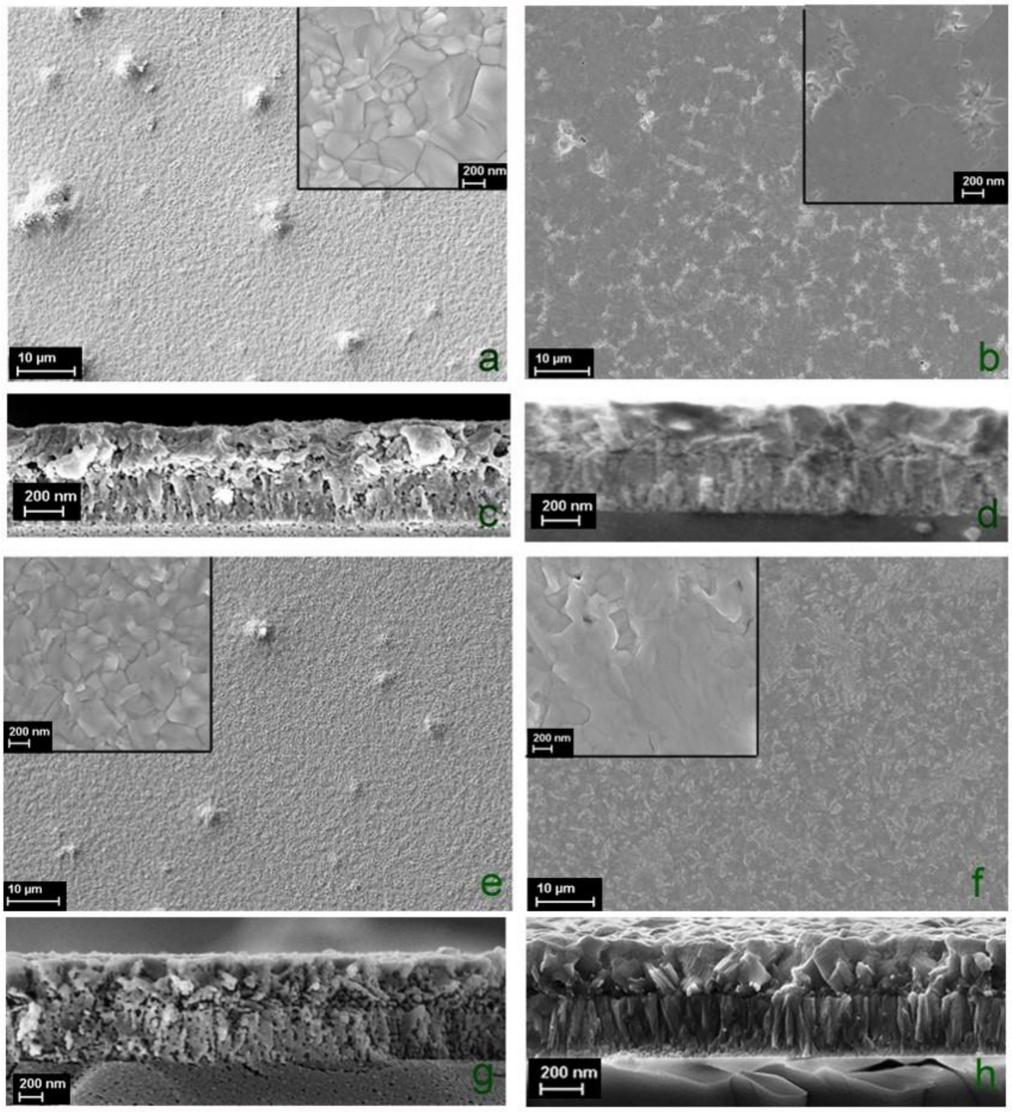

Figure 3.8: Top and cross views of $CH_3NH_3PbI_3$ layer grown on top of NRs (a and c) and NTs (e and g), the similar after being healed via MA gas, i.e., NRs (b and d) and NTs (f and h), respectively.

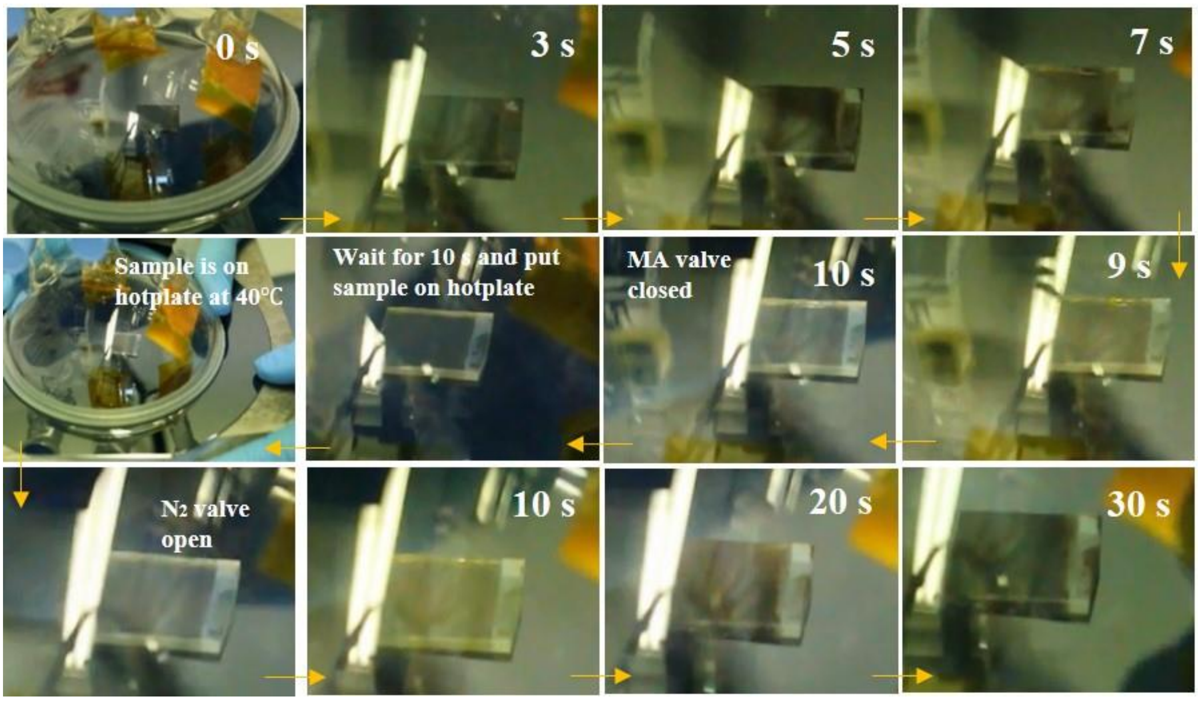

Figure 3.9: Photographs taken during MIDH process.

To compare charge extraction, transfer and recombination of healed and non-healed perovskite films (both NRs and NTs), steady state (ss) and time-resolved photoluminescence (TRPL) of the perovskite films are studied **(fig 3.10 a-h).** A comparison of PL intensity of the perovskite film on NRs and NTs with reference (perovskite on glass) shows a length dependant drop, because of the so-called charge quenching effect. In general, NRs demonstrate a better charge quenching than NTs; however, for healed perovskite films, this trend is reversed. The healed-NTs show the highest drop in the PL intensity, i.e., highest charge quenching, which is attributed to an improved physical contact of the perovskite crystals with NTs scaffold.

Similarly, TRPL spectra of the samples also show an improved charge extraction in the healed NRs/NTs samples compared to their pristine counterparts. TRPL evidences a significant improvement in the charge extraction, as noted in the faster decay region, which is related to the interfacial charge quenching [130]. No such feature is observed for the reference perovskite (on glass) due to the absence of a selective contact. In the case of higher length of NRs/NTs (110 and 115), the charge extraction is rather lower, especially for non-healed films. TRPL spectra for these films is similar to the reference perovskite signifying that the charge might not be transferred towards the scaffold – a process that takes place on a faster time scale - and are recombined bi-molecularly (a slower time-scale process) [131]. It indicates a weak physical interconnection between the scaffold and the perovskite due to poor infiltration. However, upon healing, TRPL spectra shows a dominant charge transfer with slow decay tail (associated with bulk recombination within the $CH_3NH_3PbI_3$ film) asserting an improved physical contact and the charge transfer towards the scaffolds.

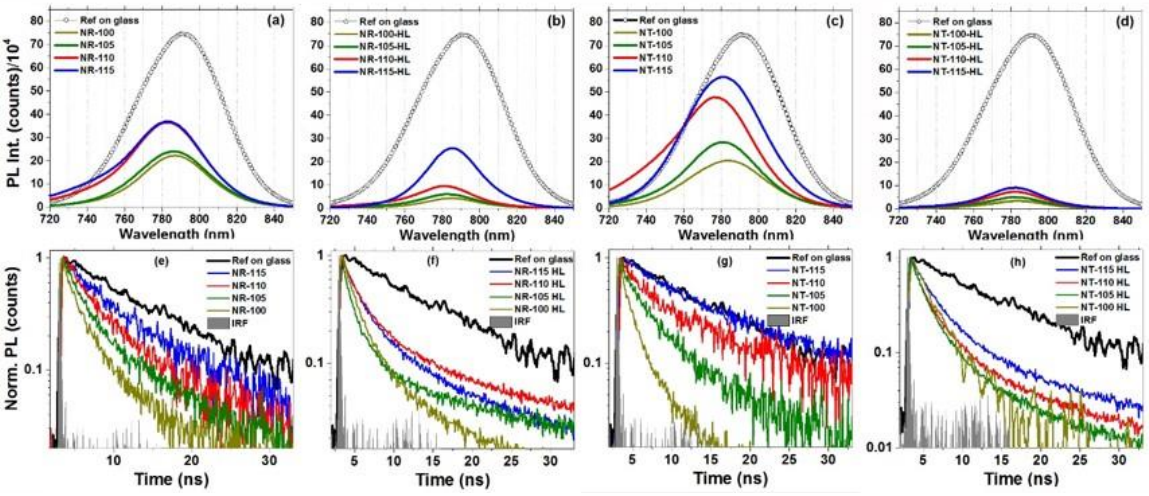

Figure 3.10: Steady-state PL spectra of $CH_3NH_3PbI_3$ layer (a) without and (b) with healing of NRs; (c) without and (d) with healing of NTs. The reference is a $CH_3NH_3PbI_3$ layer deposited on a glass. Time-resolved PL decays of the same, respectively. The PL spectra were recorded in vacuum and the samples were excited using a 405 nm laser.

The improvement in the morphology, pore-filling of the perovskite and the crystallinity after healing are further examined through full device SEM analysis. The cross-views **(fig**

3.11 a –d) clearly show that not only the healing results in the formation of larger $CH_3NH_3PbI_3$ crystals, but also more importantly, an improved pore-filling in 1D scaffolds. In **fig 3.11**, the larger voids at the bottom of nanostructures before healing **(a and b)** are not evident anymore after healing **(c and d).**

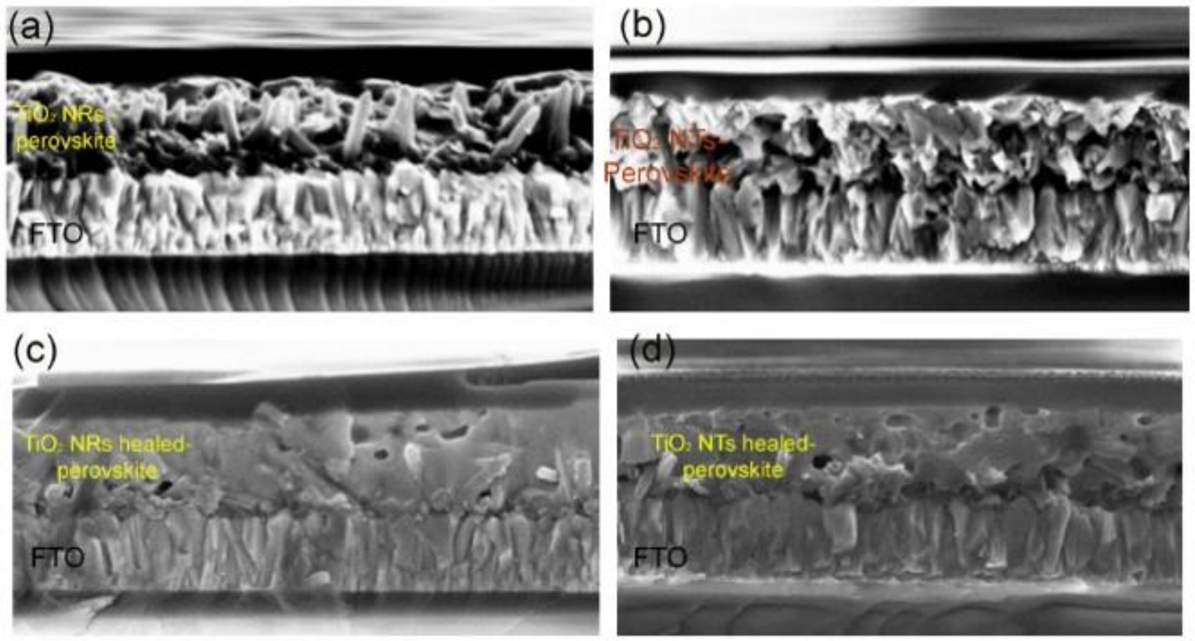

Figure 3.11: Cross-view of a PSC fabricated using (a) TiO_2 NRs and (b) NTs with a pristine $CH_3NH_3PbI_3$ layer, whereas (c) and (d) are their healed $CH_3NH_3PbI_3$ counterparts via MA gas.

The J-V curves of the NRs/NTs based PSCs with and without healing are shown in **fig 3.12** and summarized in **table 3.2.** The NR-PSCs without healing resulted in higher PCE (~9.3%) than NTs (~8.3%), even though a higher photocurrent in the latter is obtained. Higher V_{OC} and FF in the NRs than NTs suggest a lower interfacial recombination. The charge extraction in the NTs is not as efficient as in the NRs (a trend also evident in ss-PL and TRPL of NRs/NTs-perovskite films**, fig 3.10).** However, upon healing, the NTs-PSCs yielded a higher PCE than healed-NRs rivals **(fig 3.12 a and b)**, probably due an improved perovskite morphology, where interconnection is improved due to larger grains and improved pore filling. The MA gas healing not only improved J_{SC}, but also V_{OC} and FF evidencing the enhanced charge collection because of an improved perovskite morphology. For the reliable assessment, a statistical analysis of at least 10 PSCs of each type (fabricated in various batches) is shown in **fig 3.12 (c –f).** It is clear that the healed films not only improves the PV parameters but also results in more reproducible devices.

Table 3.2: J-V analysis of healed and non-healed PSCs.

Device	**J_{SC} (mA/cm^2)**	**V_{OC} (V)**	**FF**	**PCE (%)**	**R_S (Ω/cm^2)**	**R_{SH} (Ω/cm^2)**
NR-100	F 14.62 R 14.77	F 0.77 R0.88	F 52.62 R 57.94	F 7.32 R 9.33	F 14.74 R 12.83	F 0.0039 R 0.0049
NR-100 HL	F 16.66 R 17.06	F 0.89 R 0.93	F 42.77 R 52.62	F 7.80 R 10.33	F 8.14 R 40.16	F 0.0129 R 0.0107
NT-100	F 15.06 R 15.14	F 0.62 R 0.74	F 49.09 R 59.49	F 5.68 R 8.29	F 16.95 R 14.44	F 0.0031 R 0.0032
NT-100 HL	F 16.68 R 17.05	F 0.82 R 0.89	F 51.82 R 62.38	F 8.61 R 11.45	F 12.54 R 31.03	F 0.0062 R 0.0057

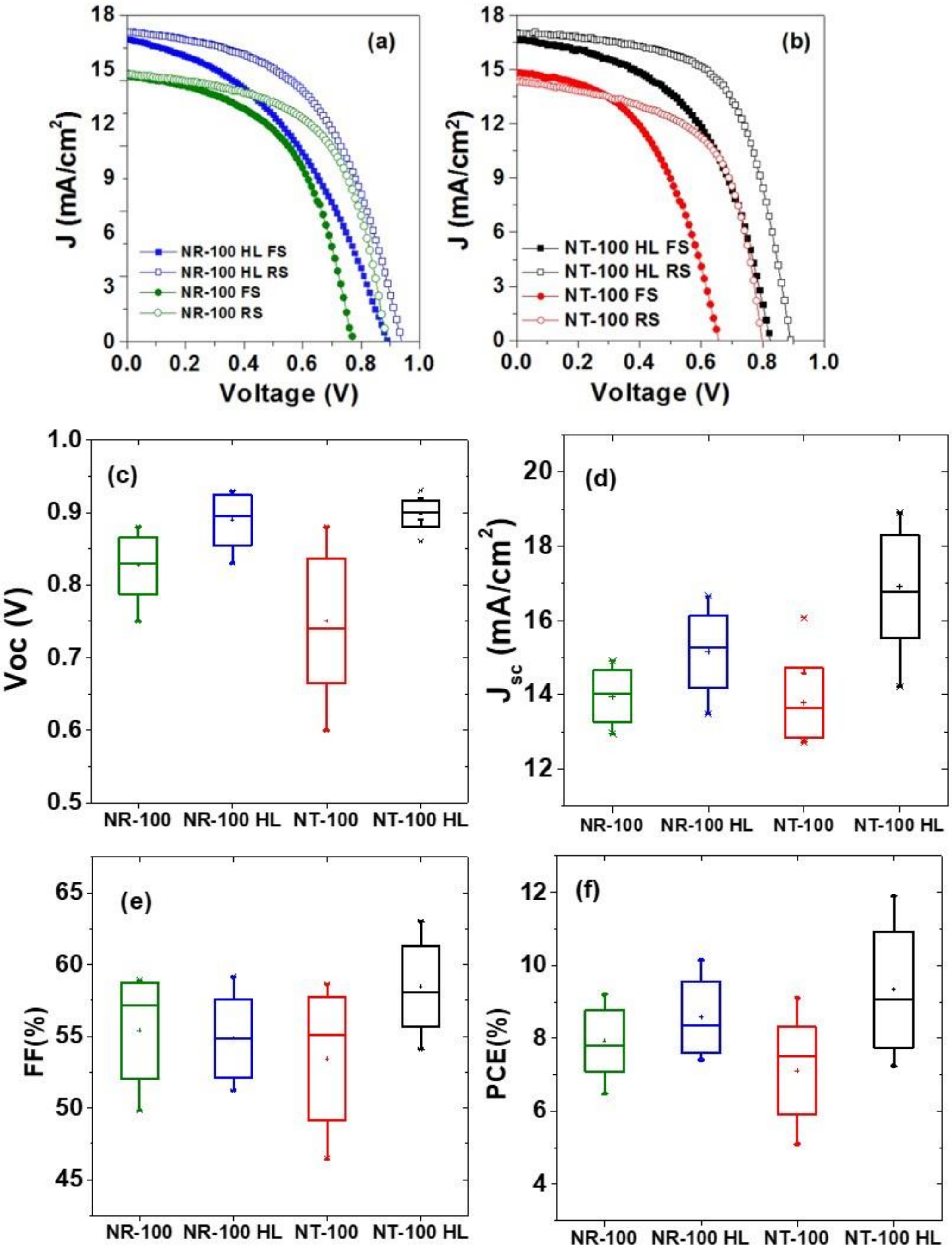

Figure 3.12:J-V analysis of PSCs (FTO/TiO_2-NR-(NT)/$CH_3NH_3PbI_3$/Spiro-OMeTAD/WO_3-Ag) fabricated using TiO_2 NRs and NTs with a pristine $CH_3NH_3PbI_3$ layer and their healed $CH_3NH_3PbI_3$ counterparts (a & b) via MA gas, respectively, whereas fig. c – f show statistical analysis of at least 10 different devices fabrictaed in various batches for reliability.

As PSCs show hysteresis, scan dependent J-V performance , measuring and reporting their stabilized performance and tracking of their maximum power point (MPP) is crucial

[132]. **Figure 3.13 (a –c)** represents stabilized J_{SC}, V_{OC}, and MPP tracking (stabilized PCE) of the devices for 300s under continuous light soaking. The NRs-PSCs (without or with healing) show a consistent J_{SC}, whereas a slight increase in J_{SC} is noted for NT-HL-PSCs.

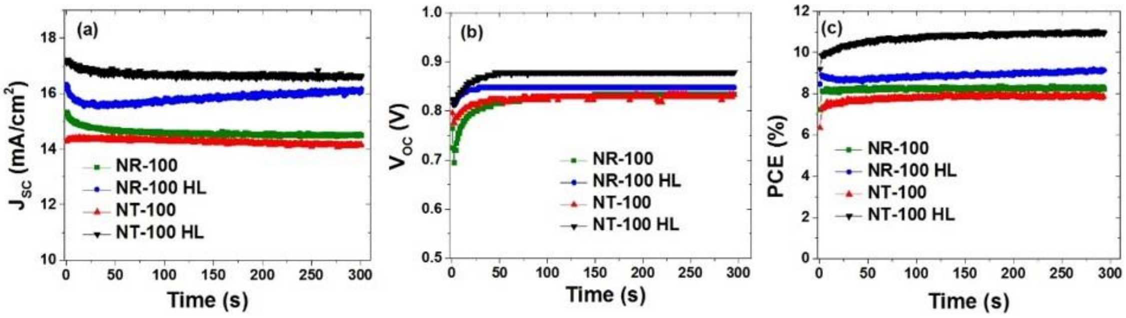

Figure 3.13: Maximum power point tracking (steady state J_{sc}, V_{oc} and PCE) of PSCs fabricated using TiO_2 NRs and NTs with and without healing at device operating conditions.

To determine the operational stability **(fig 3.14)**, the PV performance of all the PSCs is measured under continuous light soaking. The PSCs without healing show a device breakdown after 400min, while the healed counterparts do not show any breakage. Interestingly, the NRs-HL-PSCs show the highest stability after 900 min and a slight increase in PCE is observed. This is similar to our past findings that TiO_2 NRs offer a thermodynamically stable scaffolds due to higher crystallinity [107]. The NTs-HL-PSCs show ~20% drop in PCE after 900 min. The initial rise in the PCE noticed for all samples could be attributed to photo doping of Spiro-OMeTAD. The stability tests are carried out in an inert atmosphere. Therefore, any effect from the moisture or oxygen can be ruled out.

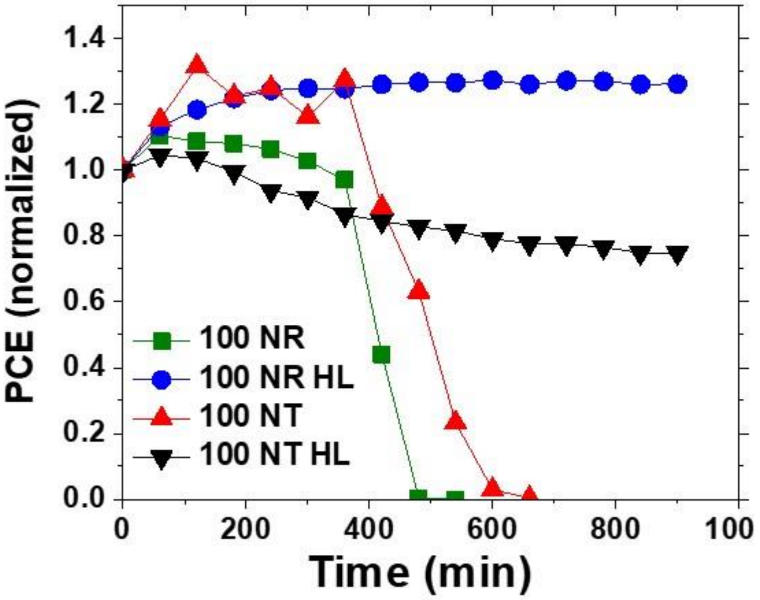

Figure 3.14: Stability testing of the various PSCs under continuous light soaking in inert

Additional work: Cell Fabrication by using P_3HT.

Following research work is not the part of the article. Nanostructured (NRs/NTs) based devices are also fabricated by using P_3HT as HTM.

The PSCs fabricated using different lengths of NRs/NTs show a systematic dependency on the length. With increasing NR and NT length, the photocurrent (J_{SC}) slightly increases, due to an improved light harvesting. However, a drop in the V_{OC} – primarily due to a higher recombination – led to a lower PCE **(Table 3.3).** A lower PCE is observed for NTs based PSCs. This could be understood from the fact that the etching process of the NRs generates additional defects in the NTs structures. For a reliable assessment, a statistical analysis of at least 10 PSCs of each type (fabricated in several batches) is shown in **fig 3.15 (a –h).**

Table 3.3: J-V analysis of PSCs fabricated using P_3HT HTL and different lengths of NRs and NTs at a light intensity of $99mW/cm^2$

Device	**Length of NS. (nm)**	**J_{SC} (mA/cm^2)**	**V_{OC} (V)**	**FF**	**PCE (%)**	**Scan Direction**
NR-100	**250±50**	10.63	0.80	46.98	4.03	F
		11.90	0.82	44.54	4.39	R
NR-105	**350±50**	11.53	0.63	32.80	2.43	F
		12.73	0.69	40.73	3.65	R
NR-110	**550±50**	12.10	0.57	34.05	2.41	F
		12.38	0.61	39.13	3.02	R
NR-115	**650±50**	10.08	0.59	33.03	1.99	F
		12.65	0.55	39.84	2.83	R
NT-100	**250±50**	10.17	0.76	37.36	2.85	F
		9.83	0.74	50.63	3.74	R
NT-105	**350±50**	8.48	0.63	38.09	2.07	F
		8.13	0.64	42.35	2.25	R
NT-110	**550±50**	8.33	0.69	33.26	1.94	F
		8.67	0.64	37.53	2.11	R
NT-115	**650±50**	6.66	0.66	34.21	1.51	F
		7.00	0.64	42.79	1.94	R

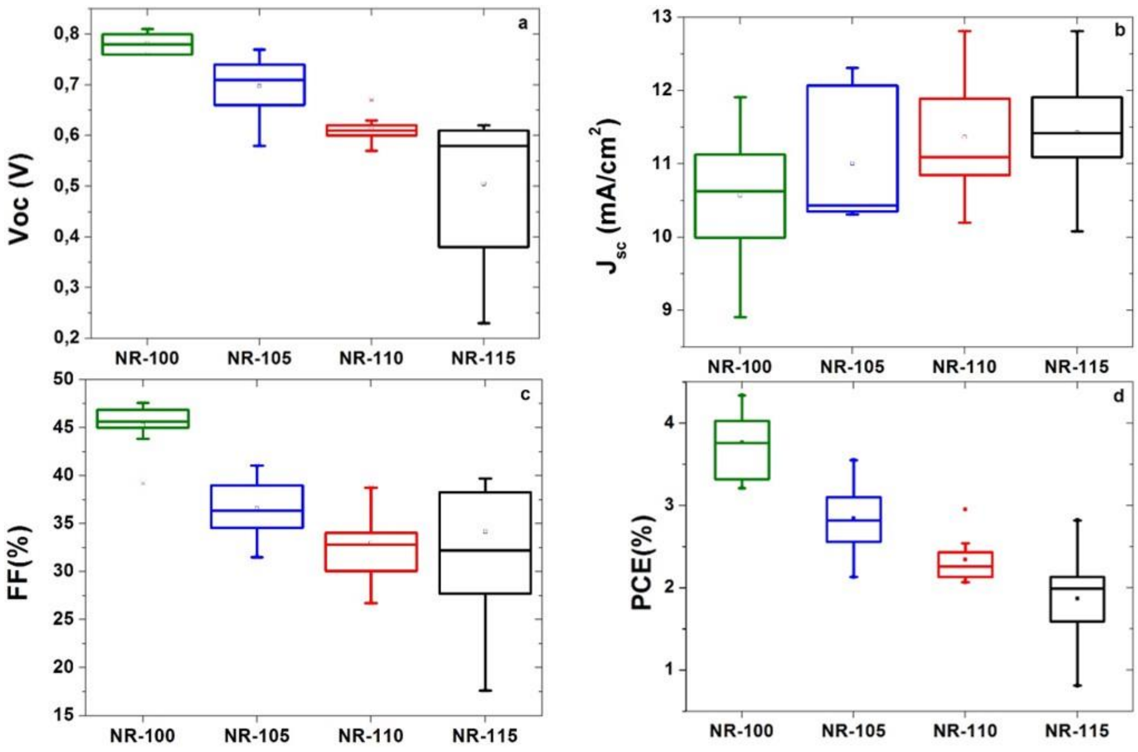

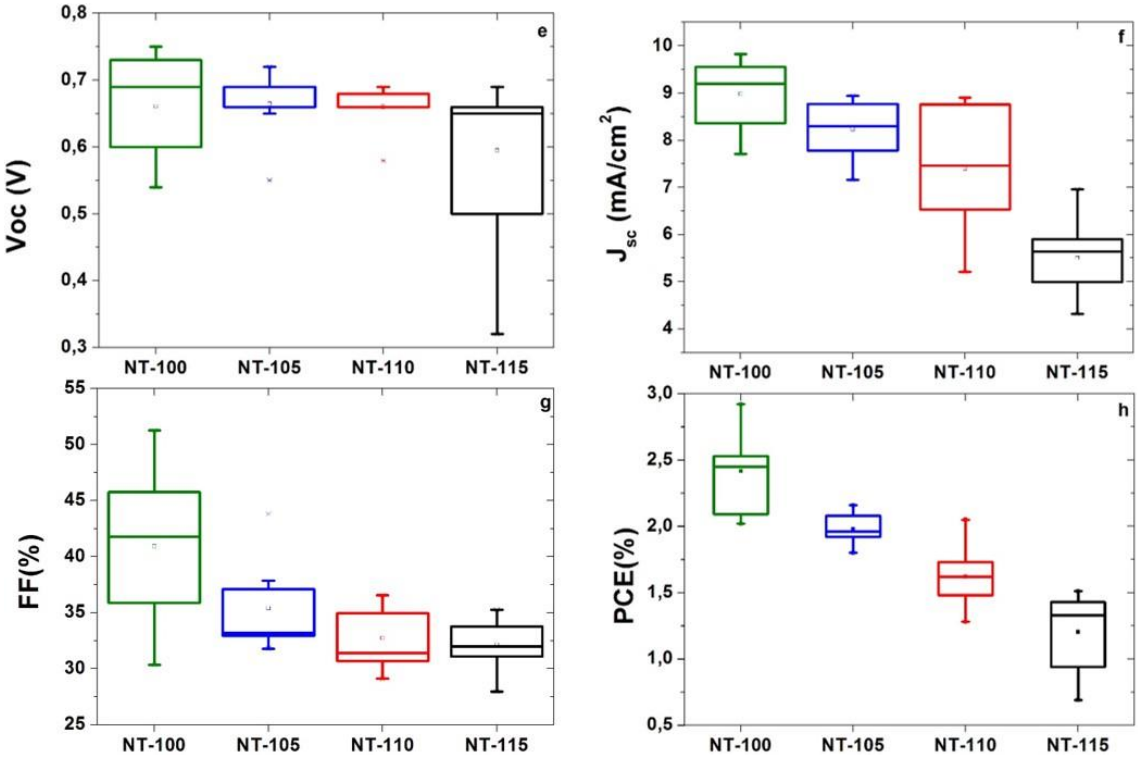

Fig 3.15: a – d (NRs-PSCs-P_3HT) and e-h (NTs-PSCs-P_3HT); statistical analysis of at least 10 different devices fabricated in various batches for reliability and measured at 99mW/cm^2

With P_3HT HTL, a similar trend is observed in the PV parameters as in the case of doped Spiro-OMeTAD, however, with lower PV parameters. The photovoltaic process in the PSCs, similar to other PV technologies, occurs in two steps: absorption of light by an absorber material (perovskite in PSCs) followed by the charge collection at the respective electrodes. Towards latter, the HTM is one of the important material in the PSCs. For an efficient device operation, HTM should provide (i) high hole mobility to minimize losses during the hole transport towards respective contact, (ii) compatible ionization potential with the perovskite (highest occupied molecular orbital (HOMO) or valance band maximum (VBM) almost matching with the perovskite to reduce injection losses), (iii) high resistance and thermal stability towards external degradation factors such as oxygen and moisture for a long term PV operation, and (iv) low-cost. Moreover, a low electron affinity will also bestow HTM with beneficial electron-blocking properties [106].

The HTM-perovskite interface is one of the probable recombination centers within the device as the electrons photo-generated nearby HTM layer, if did not extracted efficiently, may recombine with the holes in the HTM. Moreover, if the HTM layer is not dense, the electrons might reach to the metal contact thereby generating short-circuit in the device, resulting in low FF [106] [133]. The mobility of the HTM has an important bearing on the solar cell's efficiency. Low mobility leads to significant Ohmic losses across the HTM, lowering the FF and J_{SC}. [134].

We fabricated nanostructured-PSCs by using P_3HT and doped Spiro-OMeTAD as the HTM. A comparison of the PV parameters is shown in **Table 3.1 and 3.3**. The PV performance of P_3HT based PSCs is lower as compared to doped Spiro-OMeTAD, primarily (i) due to the low hole mobility of the former ($3*10^{-4}$ cm^2/Vs) [135] [136] than the latter ($1.30*10^{-3}$– $2*10^{-4}$ cm^2/Vs) [137] [138], (ii) a flat molecular structure of P_3HT inducing substantial charge recombination compared to Spiro-based devices [139], (iii) HOMO of Spiro-OMeTAD (5.22 eV) is deeper than P_3HT (5.0 eV), which makes former with smaller energy offset with the VB edge of the perovskite (5.4 eV for $CH_3NH_3PbI_3$) and obtained higher V_{OC}, and (iv) P_3HT overlaps the absorbance of perovskite thus induced a light filtering effect that could also limit the PV parameters [106].

Chapter 4

4 Summary, conclusion and future work

The research work presented in this thesis addresses the impact of morphology engineering of the active layer (halide perovskite) and the role of selective contacts on the photovoltaic performance of the perovskite solar cells (PSCs). The main contributions are:

- The perovskite's morphology is improved by solvent additive and anti-solvent treatment in planar device architectures. The solvent additive (DI-H_2O in this case) is used to enhance the solubility of the precursor solution, resulting in smooth and continuous perovskite film. The modified (toluene treated) perovskite films not only exhibited significantly lower defect density and higher crystallinity than as-prepared $MAPbI_3$ counterpart, but most importantly, favourable change in the energy levels. It is also found that anti-solvent treatment works better with single step perovskite deposition method, where perovskite film is characterized by a higher density of morphological defects.
- A perovskite healing process is demonstrated to improve the morphology of the perovskite crystals grown on one-dimensional (1D) nanostructures. A post treatment of the perovskite films in the methylamine (MA) gas environment demonstrated not only improved pore-filling and adhesion with TiO_2 but also formation of large crystals, which favoured efficient charge extraction. The healed

perovskite films showed a significant improvement in the PCE and enhanced stability under continuous light soaking.

- We investigated the effect of low hole mobility on the PV parameters, 1D nanostructured (NRs/NTs) based devices with low hole mobility HTM (P_3HT) were fabricated. We observed a significant lower PV performance of the devices fabricated with P_3HT. The mobility of the HTM has an important bearing on the solar cell's efficiency. Low mobility leads to significant Ohmic losses across the HTM, lowering the Fill Factor (FF) and short circuit current density (J_{SC}).

Future work:

In this research work, the most studied perovskite (methyl ammonium lead iodide ($MAPbI_3$)) material has been used. The challenge here is that $MAPbI_3$ perovskite has estimated bandgap value of 1.50-1.6 eV [35] [36], while the optimal band gap for solar energy conversion is in between 1.1−1.4 eV. With replacing the components of the lattice, a new perovskite material, formamidinium lead halide ($FAPbX_3$) has been developed, with a bandgap that can be tuned between 1.48− 2.23 eV. Therefore, minimum bandgap is shifted closer to the solar cell optimal [37] [140]. We have shown a significant improvement in PCE by healing of the $MAPbI_3$ films than their pristine counterparts. We expect that by replacing $MAPbI_3$ with $FAPbX_3$ and with the introduction of healing process, it could further improve the performance of the perovskite solar cells.

Device operational stability poses a challenge in the perovskite solar cells commercial deployment. The most commonly used HTM in the development of PSC is doped Spiro-

OMeTAD that demonstrated a significant PCE > 20%. However, it is characterized by rather low mobility and low conductivity in its pristine form. Therefore, dopants such as Co (III) and Li-salt, TBP are used to increase the mobility and conductivity. However, they make Spiro-OMeTAD more sensitive to humidity. For example, Li-TFSI has extremely hygroscopic nature, which acts as humidity centre in the HTM. Hence, PSCs fabricated with doped Spiro-OMeTAD degrade drastically when exposed to humidity. Furthermore, Spiro-OMeTAD is one of the most expensive material in the PSC field. This puts rigorous condition on the choice of HTM, particularly when the commercial deployment of the devices is considered that requires several years of the device operation. This brings us to pay attention to the inorganic p-type materials, which have already shown promising results in the quantum dot solar cells and DSSCs due to higher conductivity and wider band gap. Employing such inorganic materials in the PSCs may not only lead towards higher PCE, but, most importantly, will result in a cost-effective and long term stable PSCs. Amongst such materials, NiO, CuI, Cu_xO, CuSCN, GO (graphene oxide), lead sulphide quantum dots (PbS QDs) and MoO_3 offer promising possibilities to be employed as HTM in the PSCs [106]. We expect that by using inorganic HTM and with the introduction of the healing process, it could further improve the performance and long term operational stability of the perovskite solar cells.

Summary of papers

1. Morphology Study of Inverted Planar Heterojunction Perovskite Solar Cells in Sequential Deposition

In this article, a double-step perovskite deposition method is employed for the fabrication of inverted planar PSCs. The perovskite morphology is improved by the addition of small amount of additive (in this case DI-H_2O) in PbI_2/DMF solution to enhance the solubility of the solution, which results in a transition of the perovskite morphology from needle like structure to hexagonal plate structure (uniform surface coverage). A controlled amount of DI-H_2O (1 wt%) in the PbI_2/DMF solution has shown a good impact on the homogeneity of the precursor solution and on the morphology of PbI_2/perovskite films.

Author contribution:

Literature review, material synthesis, device fabrication, characterization, analysis of experimental results and manuscript preparation.

2. Insights into optoelectronic properties of anti-solvent treated perovskite films

In this article, single-step and double-step perovskite ($MAPbI_3$) deposition methods are employed for the fabrication of inverted and regular device architectures. A significant improvement in $MAPbI_3$ morphology is observed upon anti-solvent treatment. It is demonstrated that higher photocurrent values are achieved only with the highest perovskite surface coverage. The modified (toluene treated) $MAPbI_3$ films not only exhibited significantly lower defect density and higher crystallinity than as-prepared $MAPbI_3$ counterpart, but most importantly, change in $MAPbI_3$ energy levels. A slight downward shift in the valance and conduction band of $MAPbI_3$ is noticed that favoured interfacial charge transfer as evidenced in 0.47 V higher V_{OC} than non-treated $MAPbI_3$ film. It is found that anti-solvent treatment seems work better with single step, where perovskite film has higher morphological defects.

Author contribution:

Literature review, material synthesis, device fabrication, characterization, analysis of experimental results and manuscript preparation.

3. Improved pore-filling of TiO_2 nanorods and nanotubes scaffolds for perovskite solar cells

In this article, the role of one-dimensional electron transport layers (ETLs), namely, TiO_2 nanostructures (nanorods/nanotubes) on the device performance and stability is investigated. We particularly focus on improving the inferior pore-filling of perovskite in these TiO_2 scaffolds. Therefore, perovskite healing method is introduced to improve the pore-filling. The already crystallized perovskite ($CH_3NH_3PbI_3$) layer on the TiO_2 NRs/NTs is exposed to the methylamine gas (healing process). The scanning electron microscopy images revealed an improved pore-filling and the formation of large perovskite grains on healing. Photoluminescence and electrical characterizations demonstrated improved charge transfer in the healed films than their pristine analogous. A remarkable improvement in the power conversion efficiency and stability under continuous light soaking of healed perovskite films are also reported.

Author contribution:

Literature review, material synthesis, device fabrication, characterization, analysis of experimental results and manuscript preparation.

Appendix: Challenges and pitfalls during the research work

Device architectures

1. ITO/PEDOT:PSS/$CH_3NH_3PbI_3$/PCBM/Al (inverted planar)
2. ITO/c-TiO_2/$CH_3NH_3PbI_3$/P_3HT/WO_3-Ag (regular planar)
3. FTO/c-TiO_2/$CH_3NH_3PbI_3$/ Spiro-OMeTAD /WO_3-Ag (regular planar)
4. FTO/ NRs-NTs /$CH_3NH_3PbI_3$/Spiro-OMeTAD /MoO_3 (nanostructured scaffold)
5. FTO/ NRs-NTs /$CH_3NH_3PbI_3$/ Spiro-OMeTAD /Ag (nanostructured scaffold)
6. FTO/NRs-NTs/$CH_3NH_3PbI_3$/P_3HT/WO_3-Ag (nanostructured scaffold)
7. FTO/NRs-NTs/$CH_3NH_3PbI_3$/Spiro-OMeTAD/WO_3-Ag(nanostructured scaffold)

Almost 1800 devices were fabricated by using all of the above mentioned device architectures to achieve a uniform perovskite layer morphology and improved PV parameters.

Architecture (1): Many of the devices failed because of without-oxygen plasma treated ITO were used for the fabrication of solar cells. ITO substrates should be treated with oxygen plasma cleaning before spin coating of PEDOT:PSS that makes ITO surface more hydrophilic by changing the surface properties, resulting in a homogeneous PEDOT:PSS layer. Moreover, it also changes the ITO surface work function by removing carbon contaminates that makes it a better hole injector [141].

Architecture (1 and 2): Many of the devices failed due to inhomogeneous perovskite morphology. Therefore, anti-solvent treatment method was employed to achieve a smooth and uniform perovskite layer. Mole ratio of PbI_2 was carefully optimized in order to achieve a homogeneous solution at room temperature. Other factors such as spinning speed and rotation, annealing time and temperature of the perovskite films were carefully optimized to obtain a full conversion of perovskite from PbI_2.

Architecture (4, 5): A very low FF with S-shape J-V curves were observed in both architectures and no efficient devices were obtained.

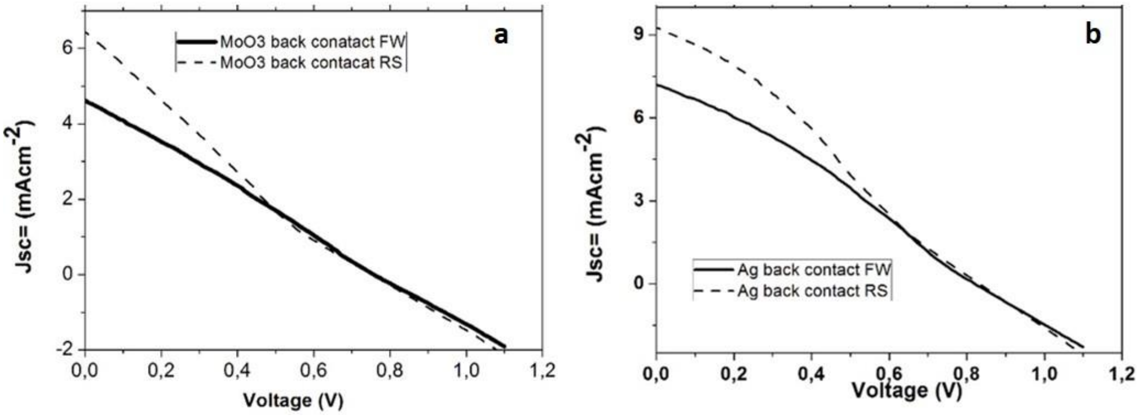

Figure 1: J-V characteristics curves for different back contacts (a) Molybdenum trioxide (MoO_3) and (b) silver (Ag).

Table1: Summary of PV parameters of PSCs at light intensity ~82mA/cm^2

Device	**J_{SC} (mA/cm^2)**	**V_{OC} (V)**	**FF**	**PCE (%)**	**Scan Direction**
NR-100 (MoO3)	4.6	0.75	27.21	1.15	F
	6.4	0.75	23.22	1.37	R
NR-100 (Ag)	7.18	0.82	30.62	2.21	F
	9.25	0.83	29.22	2.75	R

Architecture (6, 7): Nanostructure based PSCs were fabricated. A precise optimization, that is: growth and etching time, annealing temperature and time is required for nanostructured scaffolds. Other factors such as spinning speed and rotation, annealing time and temperature of the perovskite films, hot precursor solution and thickness of back contact were carefully optimized.

During the hydrothermal growth of TiO_2 NRs, a significant effect of the sheet resistance of FTO substrates on TiO_2 NRs growth was observed. It was noticed from SEM images that FTO substrates with low sheet resistance (Fig 2a) have more densely packed TiO_2 NRs rather than high sheet resistance FTO substrates (Fig 2b). To avoid short circuiting (direct contact of perovskite and FTO) and to fabricate high efficiency device, growth of NRs should be densely packed. Therefore, high sheet resistance has a negative impact on devices.

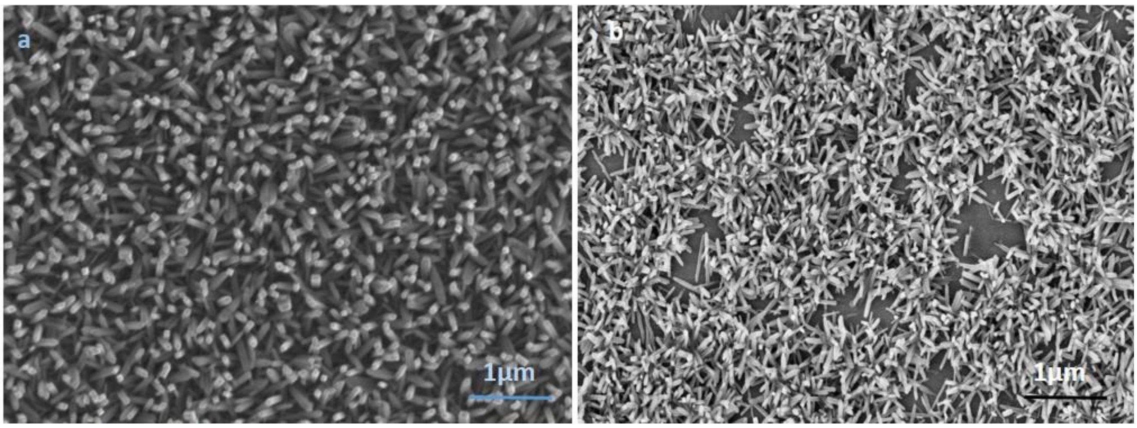

Figure 2: SEM micrographs of TiO2 NRs, (a) FTO with surface resistivity (~12 ohm/sq) and (b) surface resistivity (~25 ohm/sq)

References

[1] R. S. Lindzen, "Taking Greenhouse Warming Seriously," *Energy & Environment,* vol. 18 (7), pp. 937-950, 2007.

[2] M. Lallanilla. *Greenhouse Gas Emissions: Causes & Sources, https://www.livescience.com/37821-greenhouse-gases.html 2015.*

[3] N. S. Lewis and D. G. Nocera, "Powering the planet: Chemical challenges in solar energy utilization," *Proceedings of the National Academy of Sciences,* vol. 103 (43), pp. 15729-15735, 2006.

[4] G. Conibeer, "Third-generation photovoltaics," *Materials Today,* vol. 10 (11), pp. 42-50, 2007.

[5] A. Polman, M. Knight, E. C. Garnett, B. Ehrler, and W. C. Sinke, "Photovoltaic materials: Present efficiencies and future challenges," *Science,* vol. 352 (6283), pp. 307-317, 2016.

[6] M. H. Futscher and B. Ehrler, "Efficiency Limit of Perovskite/Si Tandem Solar Cells," *ACS Energy Letters,* vol. 1 (4), pp. 863-868, 2016.

[7] *P. REPORT, ed. I. Fraunhofer, ISE Fraunhofer, Germany, 2017.*

[8] F. Di Giacomo, A. Fakharuddin, R. Jose, and T. M. Brown, "Progress, challenges and perspectives in flexible perovskite solar cells," *Energy & Environmental Science,* vol. 9 (10), pp. 3007-3035, 2016.

[9] N. Rinaldi. *Solar PV Module Costs to Fall to 36 Cents per Watt by 2017 https://www.greentechmedia.com/articles/read/solar-pv-module-costs-to-fall-to-36-cents-per-watt#gs.yDIolPc 2017.*

[10] *Solar Industry Reports, Global Market Outlook for Photovoltaics 2014-2018.*

[11] M. A. Green, *Third Generation Photovoltaics: Advanced Solar Energy Conversion*: Springer-Verlag Berlin Heidelberg NewYork, 2003.

[12] NREL. *http://www.nrel.gov*.

[13] B. O'Regan and M. Gratzel, "A low-cost, high-efficiency solar cell based on dye-sensitized colloidal TiO2 films," *Nature,* vol. 353 (6346), pp. 737-740, 1991.

[14] K. Kakiage, Y. Aoyama, T. Yano, K. Oya, J.-i. Fujisawa, and M. Hanaya, "Highly-efficient dye-sensitized solar cells with collaborative sensitization by silyl-anchor and carboxy-anchor dyes," *Chemical Communications,* vol. 51 (88), pp. 15894-15897, 2015.

[15] W. S. Yang, B.-W. Park, E. H. Jung, N. J. Jeon, Y. C. Kim, D. U. Lee, *et al.*, "Iodide management in formamidinium-lead-halide–based perovskite layers for efficient solar cells," *Science,* vol. 356 (6345), pp. 1376-1379, 2017.

[16] Q. Wali, N. K. Elumalai, Y. Iqbal, A. Uddin, and R. Jose, "Tandem perovskite solar cells," *Renewable and Sustainable Energy Reviews,* vol. 84 (March), pp. 89-110, 2018.

[17] T. Duong, Y. Wu, H. Shen, J. Peng, X. Fu, D. Jacobs, *et al.*, "Rubidium Multication Perovskite with Optimized Bandgap for Perovskite-Silicon Tandem with over 26% Efficiency," *Advanced Energy Materials,* vol. 7 (14), pp. 1700228-n/a, 2017.

[18] A. Fakharuddin, F. De Rossi, T. M. Watson, L. Schmidt-Mende, and R. Jose, "Research Update: Behind the high efficiency of hybrid perovskite solar cells," *APL Materials,* vol. 4 (9), p. 091505, 2016.

[19] A. Djurišić, F. Liu, and H. W. Tam, "Improving the performance of ZnO-based perovskite solar cells," *Solar & Alternative Energy, SPIE,* pp. 1-3, 2017.

[20] T. Leijtens, G. E. Eperon, S. Pathak, A. Abate, M. M. Lee, and H. J. Snaith, "Overcoming ultraviolet light instability of sensitized TiO2 with meso-superstructured organometal tri-halide perovskite solar cells," vol. 4 (2885), pp. 1-7, 2013.

[21] S. Mathew, A. Yella, P. Gao, R. Humphry-Baker, F. E. CurchodBasile, N. Ashari-Astani, *et al.*, "Dye-sensitized solar cells with 13% efficiency achieved through the molecular engineering of porphyrin sensitizers," *Nat Chem,* vol. 6 (3), pp. 242-247, 2014.

[22] U. Bach, D. Lupo, P. Comte, J. E. Moser, F. Weissortel, J. Salbeck, *et al.*, "Solid-state dye-sensitized mesoporous TiO2 solar cells with high photon-to-electron conversion efficiencies," *Nature,* vol. 395 (6702), pp. 583-585, 1998.

[23] L. Schmidt-Mende and J. Weickert, *Organic and Hybrid Solar Cells*: Walter de Gruyter GmbH, Berlin/Boston, 2016.

[24] H.-S. Kim, C.-R. Lee, I.-H. Jang, W. Kang, and N.-G. Park, "Effect of Overlayer Thickness of Hole Transport Material on Photovoltaic Performance in Solid-Sate Dye-Sensitized Solar Cell," *Bull. Korean Chem. Soc,* vol. 33 (2), pp. 671-673, 2012.

[25] N.-G. Park, "Perovskite solar cells: an emerging photovoltaic technology," *Materials Today,* vol. 18 (2), pp. 65-72, 2015.

[26] H.-S. Kim, S. H. Im, and N.-G. Park, "Organolead Halide Perovskite: New Horizons in Solar Cell Research," *The Journal of Physical Chemistry C,* vol. 118 (11), pp. 5615-5625, 2014.

[27] M. Habibi, F. Zabihi, M. R. Ahmadian-Yazdi, and M. Eslamian, "Progress in emerging solution-processed thin film solar cells – Part II: Perovskite solar cells," *Renewable and Sustainable Energy Reviews,* vol. 62 (September), pp. 1012-1031, 2016.

[28] S. Luo and W. A. Daoud, "Recent progress in organic-inorganic halide perovskite solar cells: mechanisms and material design," *Journal of Materials Chemistry A,* vol. 3 (17), pp. 8992-9010, 2015.

[29] G. Niu, X. Guo, and L. Wang, "Review of recent progress in chemical stability of perovskite solar cells," *Journal of Materials Chemistry A,* vol. 3 (17), pp. 8970-8980, 2015.

[30] K. Zheng, Q. Zhu, M. Abdellah, M. E. Messing, W. Zhang, A. Generalov, *et al.*, "Exciton Binding Energy and the Nature of Emissive States in Organometal Halide Perovskites," *The Journal of Physical Chemistry Letters,* vol. 6 (15), pp. 2969-2975, 2015.

[31] H.-S. Kim, C.-R. Lee, J.-H. Im, K.-B. Lee, T. Moehl, A. Marchioro, *et al.*, "Lead Iodide Perovskite Sensitized All-Solid-State Submicron Thin Film Mesoscopic Solar Cell with Efficiency Exceeding 9%," *Scientific Reports,* vol. 2 (591), pp. 1-7, 2012.

[32] J. H. Noh, S. H. Im, J. H. Heo, T. N. Mandal, and S. I. Seok, "Chemical management for colorful, efficient, and stable inorganic-organic hybrid nanostructured solar cells," *Nano Lett,* vol. 13 (4), pp. 1764-9, 2013.

[33] T. Leijtens, S. D. Stranks, G. E. Eperon, R. Lindblad, E. M. Johansson, I. J. McPherson, *et al.*, "Electronic properties of meso-superstructured and planar

organometal halide perovskite films: charge trapping, photodoping, and carrier mobility," *ACS Nano,* vol. 8 (7), pp. 7147-55, 2014.

[34] S. D. Stranks, G. E. Eperon, G. Grancini, C. Menelaou, M. J. Alcocer, T. Leijtens, *et al.*, "Electron-hole diffusion lengths exceeding 1 micrometer in an organometal trihalide perovskite absorber," *Science,* vol. 342 (6156), pp. 341-4, 2013.

[35] P. Kanhere, S. Chakraborty, C. J. Rupp, R. Ahuja, and Z. Chen, "Substitution induced band structure shape tuning in hybrid perovskites (CH3NH3Pb1-xSnxI3) for efficient solar cell applications," *RSC Advances,* vol. 5 (130), pp. 107497-107502, 2015.

[36] H. S. Jung and N.-G. Park, "Perovskite Solar Cells: From Materials to Devices," *Small,* vol. 11 (1), pp. 10-25, 2015.

[37] G. E. Eperon, S. D. Stranks, C. Menelaou, M. B. Johnston, L. M. Herz, and H. J. Snaith, "Formamidinium lead trihalide: a broadly tunable perovskite for efficient planar heterojunction solar cells," *Energy & Environmental Science,* vol. 7 (3), pp. 982-988, 2014.

[38] G. Xing, N. Mathews, S. Sun, S. S. Lim, Y. M. Lam, M. Grätzel, *et al.*, "Long-Range Balanced Electron- and Hole-Transport Lengths in Organic-Inorganic CH3NH3PbI3," *Science,* vol. 342 (6156), pp. 344-347, 2013.

[39] S. Mathews, R. Ramesh, T. Venkatesan, and J. Benedetto, "Ferroelectric Field Effect Transistor Based on Epitaxial Perovskite Heterostructures," *Science,* vol. 276 (5310), pp. 238-40, 1997.

[40] M. Era, S. Morimoto, T. Tsutsui, and S. Saito, "Organic-inorganic heterostructure electroluminescent device using a layered perovskite semiconductor (C6H5C2H4NH3) 2PbI4," *Applied physics letters,* vol. 65 (6), pp. 676-678, 1994.

[41] H. Oshima, K. Miyano, Y. Konishi, M. Kawasaki, and Y. Tokura, "Switching behavior of epitaxial perovskite manganite thin films," *Applied physics letters,* vol. 75 (10), pp. 1473-1475, 1999.

[42] A. Kojima, K. Teshima, Y. Shirai, and T. Miyasaka, "Organometal halide perovskites as visible-light sensitizers for photovoltaic cells," *J Am Chem Soc,* vol. 131 (17), pp. 6050-1, 2009.

[43] J.-H. Im, C.-R. Lee, J.-W. Lee, S.-W. Park, and N.-G. Park, "6.5% efficient perovskite quantum-dot-sensitized solar cell," *Nanoscale,* vol. 3 (10), pp. 4088-4093, 2011.

[44] M. M. Lee, J. Teuscher, T. Miyasaka, T. N. Murakami, and H. J. Snaith, "Efficient Hybrid Solar Cells Based on Meso-Superstructured Organometal Halide Perovskites," *Science,* vol. 338 (6107), pp. 643-647, 2012.

[45] N. J. Jeon, J. H. Noh, Y. C. Kim, W. S. Yang, S. Ryu, and S. I. Seok, "Solvent engineering for high-performance inorganic–organic hybrid perovskite solar cells," *Nat Mater,* vol. 13 (9), pp. 897-903, 2014.

[46] J. Burschka, N. Pellet, S.-J. Moon, R. Humphry-Baker, P. Gao, M. K. Nazeeruddin, *et al.*, "Sequential deposition as a route to high-performance perovskite-sensitized solar cells," *Nature,* vol. 499 (7458), pp. 316-319, 2013.

[47] J.-W. Lee, D.-H. Kim, H.-S. Kim, S.-W. Seo, S. M. Cho, and N.-G. Park, "Formamidinium and Cesium Hybridization for Photo- and Moisture-Stable Perovskite Solar Cell," *Advanced Energy Materials,* vol. 5 (20), pp. 1501310-n/a, 2015.

[48] M. Saliba, T. Matsui, J. Y. Seo, K. Domanski, J. P. Correa-Baena, M. K. Nazeeruddin, *et al.*, "Cesium-containing triple cation perovskite solar cells: improved stability, reproducibility and high efficiency," *Energy Environ Sci,* vol. 9 (6), pp. 1989-1997, 2016.

[49] A. Fakharuddin, L. Schmidt-Mende, G. Garcia-Belmonte, R. Jose, and I. Mora-Sero, "Interfaces in Perovskite Solar Cells," *Advanced Energy Materials,* vol. 7 (22), pp. 1700623-n/a, 2017.

[50] W. S. Yang, J. H. Noh, N. J. Jeon, Y. C. Kim, S. Ryu, J. Seo, *et al.*, "SOLAR CELLS. High-performance photovoltaic perovskite layers fabricated through intramolecular exchange," *Science,* vol. 348 (6240), pp. 1234-7, 2015.

[51] K. Wojciechowski, M. Saliba, T. Leijtens, A. Abate, and H. J. Snaith, "Sub-150 [degree]C processed meso-superstructured perovskite solar cells with enhanced efficiency," *Energy & Environmental Science,* vol. 7 (3), pp. 1142-1147, 2014.

[52] C. Momblona, L. Gil-Escrig, E. Bandiello, E. M. Hutter, M. Sessolo, K. Lederer, *et al.*, "Efficient vacuum deposited p-i-n and n-i-p perovskite solar cells employing doped charge transport layers," *Energy & Environmental Science,* vol. 9 (11), pp. 3456-3463, 2016.

[53] H. Zhou, Q. Chen, G. Li, S. Luo, T. B. Song, H. S. Duan, *et al.*, "Photovoltaics. Interface engineering of highly efficient perovskite solar cells," *Science,* vol. 345 (6196), pp. 542-6, 2014.

[54] E. Edri, S. Kirmayer, A. Henning, S. Mukhopadhyay, K. Gartsman, Y. Rosenwaks, *et al.*, "Why lead methylammonium tri-iodide perovskite-based solar cells require a mesoporous electron transporting scaffold (but not necessarily a hole conductor)," *Nano Lett,* vol. 14 (2), pp. 1000-4, 2014.

[55] D. Liu, J. Yang, and T. L. Kelly, "Compact Layer Free Perovskite Solar Cells with 13.5% Efficiency," *Journal of the American Chemical Society,* vol. 136 (49), pp. 17116-17122, 2014.

[56] J. H. Heo, H. J. Han, D. Kim, T. K. Ahn, and S. H. Im, "Hysteresis-less inverted CH3NH3PbI3 planar perovskite hybrid solar cells with 18.1% power conversion efficiency," *Energy & Environmental Science,* vol. 8 (5), pp. 1602-1608, 2015.

[57] T. Salim, S. Sun, Y. Abe, A. Krishna, A. C. Grimsdale, and Y. M. Lam, "Perovskite-based solar cells: impact of morphology and device architecture on device performance," *Journal of Materials Chemistry A,* vol. 3 (17), pp. 8943-8969, 2015.

[58] Y. Wu, W. Chen, Y. Yue, J. Liu, E. Bi, X. Yang, *et al.*, "Consecutive Morphology Controlling Operations for Highly Reproducible Mesostructured Perovskite Solar Cells," *ACS Appl Mater Interfaces,* vol. 7 (37), pp. 20707-13, 2015.

[59] A. Fakharuddin, F. Di Giacomo, I. Ahmed, Q. Wali, T. M. Brown, and R. Jose, "Role of morphology and crystallinity of nanorod and planar electron transport layers on the performance and long term durability of perovskite solar cells," *Journal of Power Sources,* vol. 283 (June), pp. 61-67, 2015.

[60] M. A. Green, A. Ho-Baillie, and H. J. Snaith, "The emergence of perovskite solar cells," *Nat Photon,* vol. 8 (7), pp. 506-514, 2014.

[61] Q. Lin, A. Armin, R. C. R. Nagiri, P. L. Burn, and P. Meredith, "Electro-optics of perovskite solar cells," *Nature Photonics,* vol. 9 (2), pp. 106-112, 2015.

[62] D. A. Egger, A. M. Rappe, and L. Kronik, "Hybrid Organic–Inorganic Perovskites on the Move," *Accounts of Chemical Research,* vol. 49 (3), pp. 573-581, 2016.

[63] Y. Hou, "Rational Interfaces Design of Efficient Organic–inorganic Hybrid Perovskite Solar Cells," Phd thesis, Friedrich-Alexander-Universität Erlangen-Nürnberg, 2017.

[64] F. Zheng, L. Z. Tan, S. Liu, and A. M. Rappe, "Rashba Spin–Orbit Coupling Enhanced Carrier Lifetime in CH3NH3PbI3," *Nano Letters,* vol. 15 (12), pp. 7794-7800, 2015.

[65] L. M. Herz, "Charge-Carrier Dynamics in Organic-Inorganic Metal Halide Perovskites," *Annual Review of Physical Chemistry,* vol. 67 (1), pp. 65-89, 2016.

[66] N. Marinova, S. Valero, and J. L. Delgado, "Organic and perovskite solar cells: Working principles, materials and interfaces," *Journal of Colloid and Interface Science,* vol. 488 (February), pp. 373-389, 2017.

[67] R. Ihly, A.-M. Dowgiallo, M. Yang, P. Schulz, N. J. Stanton, O. G. Reid*, et al.*, "Efficient charge extraction and slow recombination in organic-inorganic perovskites capped with semiconducting single-walled carbon nanotubes," *Energy & Environmental Science,* vol. 9 (4), pp. 1439-1449, 2016.

[68] J. Cui, H. Yuan, J. Li, X. Xu, Y. Shen, H. Lin*, et al.*, "Recent progress in efficient hybrid lead halide perovskite solar cells," *Science and technology of advanced materials,* vol. 16 (3), p. 036004, 2015.

[69] T. A. Berhe, W.-N. Su, C.-H. Chen, C.-J. Pan, J.-H. Cheng, H.-M. Chen*, et al.*, "Organometal halide perovskite solar cells: degradation and stability," *Energy & Environmental Science,* vol. 9 (2), pp. 323-356, 2016.

[70] T. Leijtens, G. E. Eperon, N. K. Noel, S. N. Habisreutinger, A. Petrozza, and H. J. Snaith, "Stability of Metal Halide Perovskite Solar Cells," *Advanced Energy Materials,* vol. 5 (20), pp. 1500963-n/a, 2015.

[71] C. Manspeaker, P. Scruggs, J. Preiss, D. A. Lyashenko, and A. A. Zakhidov, "Reliable Annealing of CH3NH3PbI3 Films Deposited on ZnO," *The Journal of Physical Chemistry C,* vol. 120(12), pp. 6377-6382, 2016.

[72] L. Zheng, Y. H. Chung, Y. Ma, L. Zhang, L. Xiao, Z. Chen*, et al.*, "A hydrophobic hole transporting oligothiophene for planar perovskite solar cells with improved stability," *Chem Commun (Camb),* vol. 50 (76), pp. 11196-9, 2014.

[73] J.-H. Im, H.-S. Kim, and N.-G. Park, "Morphology-photovoltaic property correlation in perovskite solar cells: One-step versus two-step deposition of CH3NH3PbI3," *APL Mater.,* vol. 2 (8), p. 081510, 2014.

[74] J. Huang, Z. Gu, L. Zuo, T. Ye, and H. Chen, "Morphology control of planar heterojunction perovskite solar cells with fluorinated PDI films as organic electron transport layer," *Solar Energy,* vol. 133 (August), pp. 331-338, 2016.

[75] J. Xiong, B. Yang, R. Wu, C. Cao, Y. Huang, C. Liu*, et al.*, "Efficient and non-hysteresis CH3NH3PbI3/PCBM planar heterojunction solar cells," *Organic Electronics,* vol. 24 (September), pp. 106-112, 2015.

[76] K. Kara, D. A. Kara, C. Krbyk, M. Ersoz, O. Usluer, A. L. Briseno*, et al.*, "Solvent washing with toluene enhances efficiency and increases reproducibility in perovskite solar cells," *RSC Advances,* vol. 6 (32), pp. 26606-26611, 2016.

[77] D. Shen, X. Yu, X. Cai, M. Peng, Y. Ma, X. Su*, et al.*, "Understanding the solvent-assisted crystallization mechanism inherent in efficient organic-inorganic halide perovskite solar cells," *Journal of Materials Chemistry A,* vol. 2 (48), pp. 20454-20461, 2014.

[78] S. Razza, F. Di Giacomo, F. Matteocci, L. Cinà, A. L. Palma, S. Casaluci, *et al.*, "Perovskite solar cells and large area modules (100 cm2) based on an air flow-assisted PbI2 blade coating deposition process," *Journal of Power Sources*, vol. 277 (March), pp. 286-291, 2015.

[79] T. M. Schmidt, T. T. Larsen-Olsen, J. E. Carlé, D. Angmo, and F. C. Krebs, "Upscaling of Perovskite Solar Cells: Fully Ambient Roll Processing of Flexible Perovskite Solar Cells with Printed Back Electrodes," *Advanced Energy Materials*, vol. 5 (15), pp. 1500569-n/a, 2015.

[80] J. Troughton, C. Charbonneau, M. J. Carnie, M. L. Davies, D. A. Worsley, and T. M. Watson, "Rapid processing of perovskite solar cells in under 2.5 seconds," *Journal of Materials Chemistry A*, vol. 3 (17), pp. 9123-9127, 2015.

[81] J. Troughton, M. J. Carnie, M. L. Davies, C. Charbonneau, E. H. Jewell, D. A. Worsley, *et al.*, "Photonic flash-annealing of lead halide perovskite solar cells in 1 ms," *Journal of Materials Chemistry A*, vol. 4 (9), pp. 3471-3476, 2016.

[82] B.-E. Cohen, S. Aharon, A. Dymshits, and L. Etgar, "Impact of Antisolvent Treatment on Carrier Density in Efficient Hole-Conductor-Free Perovskite-Based Solar Cells," *The Journal of Physical Chemistry C*, vol. 120 (1), pp. 142-147, 2016.

[83] L. Yang, J. Wang, and W. W.-F. Leung, "Lead Iodide Thin Film Crystallization Control for High-Performance and Stable Solution-Processed Perovskite Solar Cells," *ACS Applied Materials & Interfaces*, vol. 7 (27), pp. 14614-14619, 2015.

[84] P. W. Liang, C. Y. Liao, C. C. Chueh, F. Zuo, S. T. Williams, X. K. Xin, *et al.*, "Additive enhanced crystallization of solution-processed perovskite for highly efficient planar-heterojunction solar cells," *Advanced materials*, vol. 26 (22), pp. 3748-3754, 2014.

[85] A. Mei, X. Li, L. Liu, Z. Ku, T. Liu, Y. Rong, *et al.*, "A hole-conductor-free, fully printable mesoscopic perovskite solar cell with high stability," *Science*, vol. 345 (6194), pp. 295-8, 2014.

[86] Y.-J. Jeon, S. Lee, R. Kang, J.-E. Kim, J.-S. Yeo, S.-H. Lee, *et al.*, "Planar heterojunction perovskite solar cells with superior reproducibility," *Scientific Reports*, vol. 4 (6953), pp. 1-7, 2014.

[87] C.-G. Wu, C.-H. Chiang, Z.-L. Tseng, M. K. Nazeeruddin, A. Hagfeldt, and M. Gratzel, "High efficiency stable inverted perovskite solar cells without current hysteresis," *Energy & Environmental Science*, vol. 8 (9), pp. 2725-2733, 2015.

[88] A. Nawaz, A. K. Erdinc, B. Gultekin, M. Tayyib, C. Zafer, K. Wang, *et al.*, "Morphology Study of Inverted Planar Heterojunction Perovskite Solar Cells in Sequential Deposition," *World Academy of Science, Engineering and Technology, International Science Index 115, International Journal of Electrical, Computer, Energetic, Electronic and Communication Engineering*, vol. 10 (7), pp. 922-926, 2016.

[89] N. Adhikari, A. Dubey, E. A. Gaml, B. Vaagensmith, K. M. Reza, S. A. A. Mabrouk, *et al.*, "Crystallization of a perovskite film for higher performance solar cells by controlling water concentration in methyl ammonium iodide precursor solution," *Nanoscale*, vol. 8, pp. 2693-2703, 2016.

[90] Y. Rong, Z. Tang, Y. Zhao, X. Zhong, S. Venkatesan, H. Graham, *et al.*, "Solvent engineering towards controlled grain growth in perovskite planar heterojunction solar cells," *Nanoscale*, vol. 7 (24), pp. 10595-10599, 2015.

[91] X. Zheng, B. AU - Chen, C. AU - Wu, and S. AU - Priya, "Room Temperature Fabrication of CH3NH3PbBr3 by Anti-solvent Assisted Crystallization Approach for Perovskite Solar Cells with Fast Response and Small J-V Hysteresis," *Nano Energy*, vol. 17 (September), pp. 269-278, 2015.

[92] Q. Wang, Y. Shao, Q. Dong, Z. Xiao, Y. Yuan, and J. Huang, "Large fill-factor bilayer iodine perovskite solar cells fabricated by a low-temperature solution-process," *Energy & Environmental Science,* vol. 7 (7), pp. 2359-2365, 2014.

[93] Y. Zhou, M. Yang, W. Wu, A. L. Vasiliev, K. Zhu, and N. P. Padture, "Room-temperature crystallization of hybrid-perovskite thin films via solvent-solvent extraction for high-performance solar cells," *Journal of Materials Chemistry A,* vol. 3 (15), pp. 8178-8184, 2015.

[94] M. Liu, M. B. Johnston, and H. J. Snaith, "Efficient planar heterojunction perovskite solar cells by vapour deposition," *Nature,* vol. 501 (7467), pp. 395-398, 2013.

[95] E. Vincent Obiozo, L. Binglong, and M. Tatsuo, "Air-assisted flow and two-step spin-coating for highly efficient CH 3 NH 3 PbI 3 perovskite solar cells," *Japanese Journal of Applied Physics,* vol. 55 (2S), p. 02BF08, 2016.

[96] L. Hu, J. Peng, W. Wang, Z. Xia, J. Yuan, J. Lu*, et al.*, "Sequential Deposition of CH3NH3PbI3 on Planar NiO Film for Efficient Planar Perovskite Solar Cells," *ACS Photonics*, vol. 1 (7), pp. 547-553, 2014.

[97] Q. Chen, H. Zhou, Z. Hong, S. Luo, H.-S. Duan, H.-H. Wang*, et al.*, "Planar Heterojunction Perovskite Solar Cells via Vapor-Assisted Solution Process," *Journal of the American Chemical Society*, vol. 136 (2), pp. 622-625, 2014.

[98] Y. Chen, M. He, J. Peng, Y. Sun, and Z. Liang, "Structure and Growth Control of Organic–Inorganic Halide Perovskites for Optoelectronics: From Polycrystalline Films to Single Crystals," *Advanced Science,* vol. 3 (4), pp. 1-21, 2016.

[99] N. Yantara, D. Sabba, F. Yanan, J. M. Kadro, T. Moehl, P. P. Boix*, et al.*, "Loading of mesoporous titania films by CH3NH3PbI3 perovskite, single step vs. sequential deposition," *Chemical Communications,* vol. 51 (22), pp. 4603-4606, 2015.

[100] K. Hwang, Y.-S. Jung, Y.-J. Heo, F. H. Scholes, S. E. Watkins, J. Subbiah*, et al.*, "Toward Large Scale Roll-to-Roll Production of Fully Printed Perovskite Solar Cells," *Advanced Materials,* vol. 27 (7), pp. 1241-1247, 2015.

[101] C. Yi, X. Li, J. Luo, S. M. Zakeeruddin, and M. Gratzel, "Perovskite Photovoltaics with Outstanding Performance Produced by Chemical Conversion of Bilayer Mesostructured Lead Halide/TiO2 Films," *Adv Mater,* vol. 28 (15), pp. 2964-70, 2016.

[102] Z. Xiao, Q. Dong, C. Bi, Y. Shao, Y. Yuan, and J. Huang, "Solvent annealing of perovskite-induced crystal growth for photovoltaic-device efficiency enhancement," *Adv Mater,* vol. 26 (37), pp. 6503-9, 2014.

[103] Z. Zhou, Z. Wang, Y. Zhou, S. Pang, D. Wang, H. Xu*, et al.*, "Methylamine-Gas-Induced Defect-Healing Behavior of CH3NH3PbI3 Thin Films for Perovskite Solar Cells," *Angewandte Chemie International Edition,* vol. 54 (33), pp. 9705-9709, 2015.

[104] D. L. Jacobs and L. Zang, "Thermally induced recrystallization of MAPbI3 perovskite under methylamine atmosphere: an approach to fabricating large

uniform crystalline grains," *Chemical Communications*, vol. 52 (71), pp. 10743-10746, 2016.

[105] V. Gonzalez-Pedro, E. J. Juarez-Perez, W. S. Arsyad, E. M. Barea, F. Fabregat-Santiago, I. Mora-Sero, *et al.*, "General working principles of CH3NH3PbX3 perovskite solar cells," *Nano Lett*, vol. 14 (2), pp. 888-93, 2014.

[106] Z. H. Bakr, Q. Wali, A. Fakharuddin, L. Schmidt-Mende, T. M. Brown, and R. Jose, "Advances in hole transport materials engineering for stable and efficient perovskite solar cells," *Nano Energy*, vol. 34 (April), pp. 271-305, 2017.

[107] A. Fakharuddin, F. Di Giacomo, A. L. Palma, F. Matteocci, I. Ahmed, S. Razza, *et al.*, "Vertical TiO2 Nanorods as a Medium for Stable and High-Efficiency Perovskite Solar Modules," *ACS Nano*, vol. 9 (8), pp. 8420-8429, 2015.

[108] J.-H. Im, I.-H. Jang, N. Pellet, M. Grätzel, and N.-G. Park, "Growth of CH3NH3PbI3 cuboids with controlled size for high-efficiency perovskite solar cells," *Nat Nano*, vol. 9 (11), pp. 927-932, 2014.

[109] F. Azhar, L. P. Alessandro, G. Francesco Di, C. Simone, M. Fabio, W. Qamar, *et al.*, "Solid state perovskite solar modules by vacuum-vapor assisted sequential deposition on Nd:YVO 4 laser patterned rutile TiO 2 nanorods," *Nanotechnology*, vol. 26 (49), p. 494002, 2015.

[110] B.-E. Cohen and L. Etgar, "Parameters that control and influence the organo-metal halide perovskite crystallization and morphology," *Frontiers of Optoelectronics*, vol. 9 (1), pp. 44-52, 2016.

[111] D. Liu, M. K. Gangishetty, and T. L. Kelly, "Effect of CH3NH3PbI3 thickness on device efficiency in planar heterojunction perovskite solar cells," *Journal of Materials Chemistry A*, vol. 2 (46), pp. 19873-19881, 2014.

[112] S. Paek, P. Schouwink, E. N. Athanasopoulou, K. T. Cho, G. Grancini, Y. Lee, *et al.*, "From Nano- to Micrometer Scale: The Role of Antisolvent Treatment on High Performance Perovskite Solar Cells," *Chemistry of Materials*, vol. 29 (8), pp. 3490-3498, 2017.

[113] M. Xiao, F. Huang, W. Huang, Y. Dkhissi, Y. Zhu, J. Etheridge, *et al.*, "A fast deposition-crystallization procedure for highly efficient lead iodide perovskite thin-film solar cells," *Angew Chem Int Ed Engl*, vol. 53, pp. 9898-903, 2014.

[114] V. Somsongkul, F. Lang, A. R. Jeong, M. Rusu, M. Arunchaiya, and T. Dittrich, "Hole blocking PbI2/CH3NH3PbI3 interface," *physica status solidi (RRL) – Rapid Research Letters*, vol. 08 (09), pp. 763-766, 2014.

[115] K.-F. Lin, S. H. Chang, K.-H. Wang, H.-M. Cheng, K. Y. Chiu, K.-M. Lee, *et al.*, "Unraveling the high performance of tri-iodide perovskite absorber based photovoltaics with a non-polar solvent washing treatment," *Solar Energy Materials and Solar Cells*, vol. 141 (October), pp. 309-314, 2015.

[116] N. Sakai, S. Pathak, H.-W. Chen, A. A. Haghighirad, S. D. Stranks, T. Miyasaka, *et al.*, "The mechanism of toluene-assisted crystallization of organic-inorganic perovskites for highly efficient solar cells," *Journal of Materials Chemistry A*, vol. 4 (12), pp. 4464-4471, 2016.

[117] A. A. Zhumekenov, M. I. Saidaminov, M. A. Haque, E. Alarousu, S. P. Sarmah, B. Murali, *et al.*, "Formamidinium Lead Halide Perovskite Crystals with Unprecedented Long Carrier Dynamics and Diffusion Length," *ACS Energy Letters*, vol. 1 (1), pp. 32-37, 2016.

[118] A. Kahn, "Fermi level, work function and vacuum level," *Materials Horizons,* vol. 3 (1), pp. 7-10, 2016.

[119] J.-L. Bredas, "Mind the gap!," *Materials Horizons,* vol. 1 (1), pp. 17-19, 2014.

[120] J.-Y. Jeng, Y.-F. Chiang, M.-H. Lee, S.-R. Peng, T.-F. Guo, P. Chen, *et al.*, "CH3NH3PbI3 Perovskite/Fullerene Planar-Heterojunction Hybrid Solar Cells," *Advanced Materials,* vol. 25 (27), pp. 3727-3732, 2013.

[121] Z. Zhou, S. Pang, Z. Liu, H. Xu, and G. Cui, "Interface engineering for high-performance perovskite hybrid solar cells," *Journal of Materials Chemistry A,* vol. 3 (38), pp. 19205-19217, 2015.

[122] J. Wan, R. Liu, Y. Tong, S. Chen, Y. Hu, B. Wang, *et al.*, "Hydrothermal Etching Treatment to Rutile TiO2 Nanorod Arrays for Improving the Efficiency of CdS-Sensitized TiO2 Solar Cells," *Nanoscale Research Letters,* vol. 11 (1), p. 12, 2016.

[123] L. Vesce, R. Riccitelli, G. Soscia, T. M. Brown, A. Di Carlo, and A. Reale, "Optimization of nanostructured titania photoanodes for dye-sensitized solar cells: Study and experimentation of TiCl4 treatment," *Journal of Non-Crystalline Solids,* vol. 356 (37), pp. 1958-1961, 2010.

[124] H.-E. Wang, Z. Chen, Y. H. Leung, C. Luan, C. Liu, Y. Tang, *et al.*, "Hydrothermal synthesis of ordered single-crystalline rutile TiO 2 nanorod arrays on different substrates," *Applied Physics Letters,* vol. 96 (26), p. 263104, 2010.

[125] J.-J. Chao, J.-J. Wang, S.-C. Shiu, S.-C. Hung, and C.-F. Lin, "Hydrothermal synthesis of TiO 2 nanorod arrays on transparent conducting substrates," in *Nanotechnology (IEEE-NANO),11th IEEE Conference*, 2011, pp. 1235-1238.

[126] H. Huang, L. Pan, C. K. Lim, H. Gong, J. Guo, M. S. Tse, *et al.*, "Hydrothermal growth of TiO2 nanorod arrays and in site conversion to nanotube arrays for highly efficient quantum dot-sensitized solar cells," *Small,* vol. 18 (9), pp. 3153-3160, 2013.

[127] C. K. Nguyen, H. G. Cha, and Y. S. Kang, "Axis-Oriented, Anatase TiO2 Single Crystals with Dominant {001} and {100} Facets," *Crystal Growth & Design,* vol. 11 (9), pp. 3947-3953, 2011.

[128] I. Ahmed, A. Fakharuddin, Q. Wali, A. R. Bin Zainun, J. Ismail, and R. Jose, "Mesoporous titania-vertical nanorod films with interfacial engineering for high performance dye-sensitized solar cells," *Nanotechnology,* vol. 26 (10), p. 105401, 2015.

[129] M.-J. Zhang, N. Wang, S.-P. Pang, Q. Lv, C.-S. Huang, Z.-M. Zhou, *et al.*, "Carrier Transport Improvement of CH3NH3PbI3 Film by Methylamine Gas Treatment," *ACS Applied Materials & Interfaces,* vol. 8 (45), pp. 31413-31418, 2016.

[130] D. W. deQuilettes, S. M. Vorpahl, S. D. Stranks, H. Nagaoka, G. E. Eperon, M. E. Ziffer, *et al.*, "Impact of microstructure on local carrier lifetime in perovskite solar cells," *Science,* vol. 348 (6235), pp. 683-686, 2015.

[131] W. Tress, "Perovskite Solar Cells on the Way to Their Radiative Efficiency Limit – Insights Into a Success Story of High Open-Circuit Voltage and Low Recombination," *Advanced Energy Materials,* vol. 7 (14), pp. 1602358-n/a, 2017.

[132] E. Zimmermann, K. K. Wong, M. Müller, H. Hu, P. Ehrenreich, M. Kohlstädt, *et al.*, "Characterization of perovskite solar cells: Towards a reliable measurement protocol," *APL Materials,* vol. 4 (9), p. 091901, 2016.

[133] A. Agresti, S. Pescetelli, B. Taheri, A. E. Del Rio Castillo, L. Cinà, F. Bonaccorso, *et al.*, "Graphene–Perovskite Solar Cells Exceed 18 % Efficiency: A Stability Study," *ChemSusChem,* vol. 9 (18), pp. 2609-2619, 2016.

[134] A. Alnuaimi, I. Almansouri, and A. Nayfeh, "Effect of mobility and band structure of hole transport layer in planar heterojunction perovskite solar cells using 2D TCAD simulation," *Journal of Computational Electronics,* vol. 15 (3), pp. 1110-1118, 2016.

[135] S. Choulis, Y. Kim, J. Nelson, D. Bradley, M. Giles, M. Shkunov, *et al.*, "High ambipolar and balanced carrier mobility in regioregular poly (3-hexylthiophene)," *Applied physics letters,* vol. 85 (17), pp. 3890-3892, 2004.

[136] C. Goh, R. J. Kline, M. D. McGehee, E. N. Kadnikova, and J. M. Fréchet, "Molecular-weight-dependent mobilities in regioregular poly (3-hexyl-thiophene) diodes," *Applied Physics Letters,* vol. 86 (12), p. 122110, 2005.

[137] D. Shi, X. Qin, Y. Li, Y. He, C. Zhong, J. Pan, *et al.*, "Spiro-OMeTAD single crystals: Remarkably enhanced charge-carrier transport via mesoscale ordering," *Science Advances,* vol. 2 (4), p. e1501491, 2016.

[138] A. Abate, T. Leijtens, S. Pathak, J. Teuscher, R. Avolio, M. E. Errico, *et al.*, "Lithium salts as "redox active" p-type dopants for organic semiconductors and their impact in solid-state dye-sensitized solar cells," *Physical Chemistry Chemical Physics,* vol. 15 (7), pp. 2572-2579, 2013.

[139] D. Bi, L. Yang, G. Boschloo, A. Hagfeldt, and E. M. J. Johansson, "Effect of Different Hole Transport Materials on Recombination in CH3NH3PbI3 Perovskite-Sensitized Mesoscopic Solar Cells," *The Journal of Physical Chemistry Letters,* vol. 4 (9), pp. 1532-1536, 2013.

[140] G. E. Eperan, "Active alyer control for high efficiency perovskite solar cells," Phd thesis, University of Oxford, 2015.

[141] D. Lu, Y. Wu, J. Guo, G. Lu, Y. Wang, and J. Shen, "Surface treatment of indium tin oxide by oxygen-plasma for organic light-emitting diodes," *Materials Science and Engineering: B,* vol. 97 (2), pp. 141-144, 2003.